Boston University

OpenBU **http://open.bu.edu**

Theses & Dissertations Boston University Theses & Dissertations

2021

Interferometric reflectance microscopy for physical and chemical characterization of biological nanoparticles

https://hdl.handle.net/2144/43096

Boston University

BOSTON UNIVERSITY

COLLEGE OF ENGINEERING

Dissertation

INTERFEROMETRIC REFLECTANCE MICROSCOPY FOR PHYSICAL AND CHEMICAL CHARACTERIZATION OF BIOLOGICAL NANOPARTICLES

by

CELALETTIN YURDAKUL

B.S., Koç University, 2016

Submitted in partial fulfillment of the
requirements for the degree of
Doctor of Philosophy

2021

© 2021 by
CELALETTIN YURDAKUL
All rights reserved

Approved by

First Reader

M. Selim Ünlü, PhD
Professor of Electrical and Computer Engineering
Professor of Materials Science and Engineering
Professor of Biomedical Engineering
Professor of Physics

Second Reader

Ji-Xin Cheng, PhD
Moustakas Chair Professor in Photonics and Optoelectronics
Professor of Electrical and Computer Engineering
Professor of Biomedical Engineering
Professor of Materials Science and Engineering
Professor of Chemistry
Professor of Physics

Third Reader

Lei Tian, PhD
Assistant Professor of Electrical and Computer Engineering
Assistant Professor of Biomedical Engineering

Fourth Reader

Anna K. Swan, PhD
Associate Professor of Electrical and Computer Engineering
Associate Professor of Materials Science and Engineering
Associate Professor of Physics

Dedicated to my family

Acknowledgments

First, I would like to express my deep gratitude to Prof. Selim Ünlü, who has been always an honest and friendly advisor. His mentorship and persistent support throughout my PhD helped my growth as a researcher.

I would like to thank all my committee members; Prof. Ji-Xin Cheng, Prof. Lei Tian, and Prof. Anna Swan for guiding and collaborating on the projects. I'd like to express my special thanks to Prof. Cheng for kindly welcoming me to their group and for his scientific guidance over the last three years.

I'm thankful to all my colleagues in Photonics Center for making the PhD life enjoyable. I owe a debt to Oguzhan for his guidance and mentorship in my first year. Special thanks to past and current OCN group members: David, Fulya, Jake, Derin, Negin, Alex, Matt, Allison, Eli, and Iris. I'm also grateful to Cheng's group members including Peng, Haonan, Jian, Yi, Yeran, Lu, and Jiaze for their friendship and cheerfulness.

I'm indebted to my parents, sister, brother, and extended family including aunties, for believing me in my endeavors and providing their constant love and support during my entire education life. Finally, I would like to thank Gozde for the greatest support in this journey.

INTERFEROMETRIC REFLECTANCE MICROSCOPY FOR PHYSICAL AND CHEMICAL CHARACTERIZATION OF BIOLOGICAL NANOPARTICLES

CELALETTIN YURDAKUL

Boston University, College of Engineering, 2021

Major Professor: M. Selim Ünlü, PhD
Professor of Electrical and Computer Engineering
Professor of Materials Science and Engineering
Professor of Biomedical Engineering
Professor of Physics

ABSTRACT

Biological nanoparticles have enormous utility as well as potential adverse impacts in biotechnology, human health, and medicine. The physical and chemical properties of these nanoparticles have strong implications on their distribution, circulation, and clearance *in vivo*. Accurate morphological visualization and chemical characterization of nanoparticles by label-free (direct) optical microscopy would provide valuable insights into their natural and intrinsic properties. However, three major challenges related to label-free nanoparticle imaging must be overcome: (i) weak contrast due to exceptionally small size and low-refractive-index difference with the surrounding medium, (ii) inadequate spatial resolution to discern nanoscale features, and (iii) lack of chemical specificity. Advances in common-path interferometric microscopy have successfully overcome the weak contrast limitation and enabled direct detection of low-index biological nanoparticles down to single proteins. However, interferometric light microscopy does not overcome the diffraction limit, and studying the nanoparticle morphology at sub-wavelength spatial resolution remains a significant challenge. Moreover, chemical signature and composition are inaccessible in these interferometric optical measurements. This dissertation explores innovations in common-path interferometric microscopy to provide enhanced spatial resolution and chemical specificity in high-throughput imaging of individual nanoparticles.

The dissertation research effort focuses on a particular modality of interferometric imaging, termed “single-particle interferometric reflectance (SPIR) microscopy”, that uses an oxide-coated silicon substrate for enhanced coherent detection of the weakly scattered light. We seek to advance three specific aspects of SPIR microscopy: sensitivity, spatial resolution, and chemical specificity. The first one is to enhance particle visibility via novel optical and computational methods that push optical detection sensitivity. The second one is to improve the lateral resolution beyond the system’s classical limit by a new computational imaging method with an engineered illumination function that accesses high-resolution spatial information at the nanoscale. The last one is to extract a distinctive chemical signature by probing the mid-infrared absorption-induced photothermal effect. To realize these goals, we introduce new theoretical models and experimental concepts.

This dissertation makes the following four major contributions in the wide-field common-path interferometric microscopy field: (1) formulating vectorial-optics based linear forward model that describes interferometric light scattering near planar interfaces in the quasi-static limit, (2) developing computationally efficient image reconstruction methods from defocus images to detect a single 25 nm dielectric nanoparticle, (3) developing asymmetric illumination based computational microscopy methods to achieve direct morphological visualization of nanoparticles at 150 nm, and (4) developing bond-selective interferometric microscopy to enable multispectral chemical imaging of sub-wavelength nanoparticles in the vibrational fingerprint region. Collectively, through these research projects, we demonstrate significant advancement in the wide-field common-path interferometric microscopy field to achieve high-resolution and accurate visualization and chemical characterization of a broad size range of individual biological nanoparticles with high sensitivity.

Contents

1 Introduction 1

1.1 Dissertation objectives 6

1.2 Published work 8

2 Theoretical and experimental considerations in single particle interferometric reflectance microscopy 9

2.1 Introduction 9

2.2 Common-path interferometic detection 9

2.3 Enhancement of scattered light 16

2.4 Experimental considerations in SPIR 17

2.4.1 Köhler illumination 17

2.4.2 Experimental setup 18

2.4.3 Illumination engineering for enhanced visibility 23

2.4.4 Noise characteristics 25

2.5 Conclusion 29

3 Computational nanosensing from interferometric defocus images 30

3.1 Introduction 30

3.2 Experimental setup 33

3.3 Interferometric defocus signal 34

3.4 Linear forward model of SPIR 36

3.5 PSF calculations 40

3.6 Experimental validation of simulations 40

3.7 Reconstruction from defocus 42
3.8 Proof-of-concept experiments 44
3.9 Conclusion 47

4 High-resolution interferometic microscopy by computational asymmetric illumination 48

4.1 Introduction 48
4.2 Experimental design of caSPIR 50
4.3 Forward model of caSPIR 52
4.4 Illumination function optimization 53
4.5 Object reconstruction 58
4.6 Experimental validation of caSPIR 60
4.7 Resolution characterization 61
4.8 Sensitivity characterization 66
4.9 Artificial nanocarrier experiments 69
    4.9.1 Synthesis of PLGA nanospheres 70
    4.9.2 Fabrication of PLGA nanorods 71
    4.9.3 Preparation of PLGA sample 72
    4.9.4 Experiments on PLGA nanocariers 72
4.10 Virus experiments 73
    4.10.1 Creation and use of Virus and VLP sample 73
    4.10.2 Antibody microarray assay preparation 74
    4.10.3 Experiments on Ebola VLPs 76
    4.10.4 Experiments on Ebola VSVs 78
4.11 Conclusion 80

5 Bond-selective interferometric microscopy 82

5.1 Introduction 82

5.2 Theoretical considerations 84
    5.2.1 Interferometric photothermal contrast mechanism 84
    5.2.2 Theoretical simulations 87
    5.2.3 Temperature dependence of photothermal signal 89
    5.2.4 Photothermal effect COMSOL simulations 91
5.3 Experimental considerations 93
    5.3.1 Experimental setup 93
    5.3.2 Backside IR illumination 94
    5.3.3 Camera-based photothermal signal detection mechanism . . . 95
5.4 System validation and characterization 98
    5.4.1 IR spot visualization 98
    5.4.2 Noise analysis 98
    5.4.3 Resolution analysis 101
    5.4.4 Validation of theoretical calculations 103
    5.4.5 Mechanical stability in acquisitions 105
5.5 Biological experiments 106
    5.5.1 Bacteria and Fungi sample preparation 106
    5.5.2 Bond-selective bacteria imaging 107
    5.5.3 Bond-selective fungi imaging 110
5.6 Conclusion 111

6 Conclusions **112**
6.1 Summary 112
6.2 Future Research Directions 113
    6.2.1 Label-free nanoscopy in common-path interferometric microscopy 113
    6.2.2 Mid-infrared photohermal nano-imaging/sensing 114

References **115**

Curriculum Vitae **126**

List of Figures

1·1 (a) Total internal reflection dark-field microscopy (TIRDF), adapted from [Enoki et al., 2012]. (b) Surface plasmon resonance imaging (SPRI), adapted from [Jing et al., 2019]. (c) Interferometric scattering (iSCAT) microscopy, adapted from [Arroyo et al., 2016]). (d) Coherent brightfield (COBRI) microscopy, adapted from [Huang et al., 2017]. . 3

2·1 Schematic of common-path interferometric detection on SiO_2/Si layered substrate and light-nanoparticle interaction. Incident electric field ($\mathbf{E_i}$) reflects off the substrate surface ($\mathbf{E_r}$) and scatters from nanoparticle ($\mathbf{E_s}$) as a result of particle's polarizability (α). 10
2·2 Schematic of reflection in a two-layer substrate. 11
2·3 Experimental and simulation data for 100 nm silica beads in diameter (r = 50 nm). Scale bar is 1 µm. 14
2·4 (a) Horizontally (in x) oriented dipole in air on top of SiO_2/Si layered substrate. (b) Normalized dipole radiation profile in collection direction (+z) for SiO_2 thickness d at 0 and 100 nm. $n_1 = 1$, $n_2 = 1.47$, $n_3 = 5.14$ and illumination wavelength is 420 nm. 15
2·5 (a) Vertically (in z) oriented dipole in air on top of SiO_2/Si layered substrate. (b) Normalized dipole radiation profile in collection direction (+z) for SiO_2 thickness d at 0 and 100 nm. $n_1 = 1$, $n_2 = 1.47$, $n_3 = 5.14$ and illumination wavelength is 420 nm. 17
2·6 Köhler illumination configuration. 18

2·7 (a) Schematic of the SPIR microscope. IS, integrating sphere; AD, aperture diaphragm; FD, field diaphragm; L, lenses; BS, beam splitter; TL, tube lens; NA, numerical aperture. 20
2·8 (a) Picture of SPIR microcope, (b) SiO_2/Si chip, and (c) adjustable aperture 21
2·9 (Left) Simulations for nanoparticle signal with respect to illumination NA. The red dashed line around 1.01 indicates the limit of detection in terms of particle visibility for a 10 ke- pixel full-well-capacity. (Right) Simulated defocus scans of low-NA (0.3) and full-NA (0.8) illuminations. 23
2·10 Background-normalized SPIR images of polystyrene beads with 50 nm nominal diamater at their highest signal defocus plane for 0.3 NA and full-NA configurations. 24
2·11 Calculated noise in a single image for different collected photons (P). The fitted curve ($\alpha P^{0.45}$) has a slope of 0.45 in logarithmic scale, indicating shot-noise-limited detection. The total number of electrons in a single pixel is nearly 6 ke-. 25
2·12 Noise-floor calculated for different number of frames (N) averaging. The fitted curve ($\alpha N^{0.5}$) has a slope of 0.5, theoretical expected value for random noise. 27
2·13 SPIR images of 100 nm silica beads at different number (N) of averaged frames. 28

3·1 Experimental setup of SPIR microscopy. 33

3·2 Defocus in SPIR microscopy. (a) Schematic of the setup illustrating the case when sensor surface is in the same plane as the focal plane of the objective ($z = 0$), the defocus takes place by moving this layered substrate in the axial direction (z), (b) simulated interferometric defocus curves for 60 nm gold and 65 nm polystyrene nanospheres . . 34

3·3 Simulated cross-sectional defocus image (XZ plane) 36

3·4 (a) Defocus profiles of silica beads with the 100 nm nominal diameter. The red curve indicates the mean SPIR contrast of ∼1462 beads detected across the full FOV. The shaded curve indicates the standard deviation of the measured SPIR contrasts (b-d) (Top) The normalized and background-subtracted experimental SPIR images and (bottom) the calculated PSFs at the defocus positions (i-iii) from left to right, respectively. Scale bar is 1 µm. 41

3·5 Flow chart of computational nanosensing using defocus curves in SPIR. (a) Schematic of defocus scan. The defocus images are acquired by translating the sample along the optical (z) axis using the piezo scanner. (b) (Top) Defocus stack images normalized with background $I^N(r|z)$ and (bottom) the max-contrast image from the normalized stack. (c) Background image I^N_{bg} is obtained by median filtering along the defocus dimension. (d) (Top) Background subtracted SPIR signal $I^S(r|z)$ defocus stack and (bottom) max-contrast image from the stack. (e) Reconstructed single image. Scale bars are 2 µm. 42

3·6 (a)Reconstructed image of silica beads with a 50 nm nominal diameter. In total, ∼1275 silica beads are detected across the full FOV after filtering out of range particle contrasts. Insets (b-e) are the zoom-in regions indicated by the dashed square in (a). (b) The normalized intensity image at defocus position of maximum contrast, (c) the background image calculated from the defocus image stack, (d) the background-subtracted normalized SPIR image calculated from (b) and (c), and (e) reconstructed image inset indicated in (a). (f) The cross-section profiles along the dashed line in (c). (g) The SNR histogram of silica beads (N = ∼1275) detected in reconstructed image (a) and normalized, the background-subtracted image at the maximum-contrast defocus plane. Scale bars in (a) and (b-e) are 20 µm and 2 µm, respectively. 46

4·1 Single Particle Interferometric Reflectance (SPIR) microscopy. (a) Schematic of the experimental setup. IS, integrating sphere; CSA, circular sector aperture; RM, rotation mount; L1-L2, lenses; BS, 50:50 beam splitter; TL, tube lens. (b) Low-NA and (c) full-NA illumination schemes in conventional SPIR. (d,e), asymmetric illumination schemes in caSPIR with different rotation angles, 0° and 180° respectively (white dashed line denotes the boundary–back pupil size–of spatial frequencies limited by objective NA). (f-i) Calculated PSFs correspond to illumination schemes in (b-d), respectively. PSFs are calculated for 100×/0.9 NA objective in air at 420 nm illumination wavelength. The illumination NAs are set 0.3 and 0.9 in (f,g), respectively. 51

4·2 Circular sector aperture. (a) 3D CAD illustration of 60° circular sector mask. (b) Left to right: 3D printed sector mask, rotation mount, and circular iris aperture for low-NA illumination. 52

4·3 Circular sector optimization. (Top) Circular sector illustration and cross-section profiles along the center line for circular sector angles ranging from 30° to 180°. (Bottom) Annular aperture illustration at sector angle 60° and cross-section profiles along center line for blocked NAs ranging from 0 to 0.75 NA. Normalized intensity values are scaled with arbitrary unit. 54

4·4 Circular sector PSF optimization. Source-function illustrations and their corresponding PSFs and TFs. 56

4·5 Contrast and frequecny support comparison of full-NA and asymetric illumination functions. 57

4·6 Oxide thickness effect on the SPIR contrast under 60° asymmetric illumination. 59

4·7 Experimental validation of caSPIR. (a) Experimental (left two rows) images of 100 nm PS bead and theoretically (right two rows) calculated PSFs corresponds to circular sector mask's angle of axis of the asymmetry. (b) Experimental caSPIR image of a single 100 nm PS bead and cross-section profile. (c) Simulated caSPIR image of a delta function and cross-section profile. 60

4·8 SEM image of example patterns imprinted on EBL sample. The sample is fabricated in colloboration with Prof. Ekmel Ozbay at Bilkent University Nanotechnology Research Center (NANOTAM). 62

4·9 System evaluation of caSPIR with 250 nm separated nanobars. The EBL sample was inspected on FE-SEM (ZEISS, GeminiSEM 300) without any preparation process to preserve the sample. Scale bars are 300 nm. 63

4·10 System evaluation of caSPIR with bar nanostructures. The conventional SPIR and caSPIR images, and SEM images of 200 nm, 150 nm, 125 nm, and 100 nm separated nanobars. Vertical and horizontal profiles of the conventional SPIR (blue) and caSPIR (red) images. Scale bars are 300 nm. 64

4·11 Regularization parameter sweep. Different solutions are generated by sweeping the regularization parameter (α) from $0.1 \times \alpha_0$ to $10 \times \alpha_0$, where $\alpha_0 = 0.01$ is the chosen parameter. (Top) Reconstructed caSPIR images of 250 nm separated nanobars. (Bottom) Cross-section profiles along the horizontal nanobars. The results demonstrate that the choice of the regularization parameter is not critical within the close range of the selected parameter. 65

4·12 L-curve for the regularization parameter sweep in Tikhonov regularized solution. It is calculated for caSPIR image in Figure 4·9. The selected regularization parameter ($\alpha = 0.01$) falls nearby the L-curve's corner. 66

4·13 caSPIR imaging of nano-words. (a) Full FOV caSPIR image. Insets (b) and (c) are the zoom-in region of interest areas of caSPIR and conventional SPIR images, respectively. Scale bars in (a) and (b,c) are 10 µm and 1 µm, respectively. 67

4·14 Fabrication non-uniformity in EBL sample. (a) caSPIR, (b) conventional SPIR, and (c) SEM images of nano-word *BU NANO*. Fabrication non-uniformity can be clearly seen at the corners of the nano-letters. Scale bars are 1 µm 67

4·15 Sensitivity characterization of caSPIR. 100 nm PS bead cross-section profile captured under the asymmetric illumination with different number of frames (N) averaged. The image is normalized with the background signal, followed by background subtraction. The standard deviation of the background is ∼0.017. 69

4·16 SEM micrographs of PLGA (a) nanospheres and (b) nanorods, respectively. The PLGAs are fabricated in colloboration with Prof. Samir Mitragotri at Harvard University. Scale bar is 1 µm 71

4·17 caSPIR imaging of biodegradable PLGA nanospheres and nanorods. (a-d) caSPIR images and (e-h) their corresponding conventional SPIR images. Scale bars are 300 nm 72

4·18 caSPIR imaging of Ebola virus like particles. (a-c) (Left) caSPIR images and (Right) SEM images. SEM image area in (c) is indicated by a box. (d) caSPIR image. The Ebola VLP sample was coated by gold using sputter coater (Cressington, 108) and imaged on FE-SEM (ZEISS, Supra 55VP). Scale bars are 1 µm. 75

4·19 Ebola VLP cross-sections in caSPIR images. (a) caSPIR image. **b,c** (Left to right) cross-section profiles indicated by dash lines in (a), and SEM images of the indicated VLPs, respectively. Scale bars are 1 µm. 77

4·20 caSPIR imaging of recombinant Vesicular Stomatitis Virus Ebola model. (a) Full-FOV caSPIR image (∼1350 VSVs in the FOV). (b-e) Zoom-in areas indicated by arrows in (a), and (f-i) their conventional SPIR images, respectively. Scale bar in full-FOV image is 10 µm and scale bars in zoom-in areas in (b-i) are 300 nm. 79

5·1 Layout of the common-path interferometric detection, nanoparticle is placed on top of 70 nm Si_3N_4/Si layered substrate. The visible incidence field ($\mathbf{E_i}$) scatters from sample ($\mathbf{E_s}$) and reflects off the substrate surface ($\mathbf{E_r}$). The mid-IR pump beam absorbed by the nanoparticle causes temperature rise (ΔT) and induces change in particle's polarizability ($\Delta\alpha$) which is a function of size and refractive index change. The pump is incident on the sample with an oblique angle ($\theta =\sim 62°$) close to the Brewster's angle to improve the IR transmission and to avoid absorption by the OL. 85

5·2 Simulated scattering polar plots of 100 nm PMMA bead on silicon substrate in the hot $P_{Hot}(\theta)$ and cold $P_{cold}(\theta)$ states and corresponding photothermal polar plot obtained by subtracting hot and cold states, $P_{PT}(\theta) = P_{Hot}(\theta) - P_{Cold}(\theta)$. The signals are normalized by the maximum intensity value in the cold state. The simulation parameters at 520 nm illumination wavelength: $\theta_{\text{incident}} = 0°$, $n_{\text{medium}} = 1$, $n_{\text{silicon}} = 4.2$,$n_{\text{PMMA}} = 1.49$, dn/dT = - 1.1 × 10^{-4} K^{-1}, dr/dT = 90 × 10^{-6} K^{-1}, $T_0 = 298$ K. 87

5·3 Simulated temperature dependence of photothermal signal for 500 nm PMMA bead. Simulation parameteres are the same in Figure 5·2 . . 90

5·4 (a) Temperature distribution when a 500 nm PMMA bead is heated by the IR pulse. The time is at 500 ns after the rising edge of the IR pulse. (b) Temperature rising for different sizes of PMMA beads. . . 91

5·5 Schematic of wide-field interferometric mid-infrared photothermal microscopy. L1-L2: achromatic doublets; BS: beam-splitter; M1: gold mirror; P1: parabolic gold mirror; AOM: acousto-optic modulator; OL: objective lens. 93

5·6 Back-side IR illumination optimization. (a) Calculated transmission of silicon substrate for polarized IR beam at various angle of incidence. Simulation parameters: $\tilde{\nu}_{illumination} = 1650\ cm^{-1}$, $n_{silicon} = 3.4$, $n_{medium} = 1$. The imaginary part of silicon refractive index is omitted in the transmission calculations. (b) Topological polarization rotation of IR light from s to p polarization state. 94

5·7 (a) Virtual camera lock-in detection. The synchronization and timing are controlled by the pulse generator which externally triggers the pump, probe, and camera. T period of the IR and pump pulse which is set to 200 kHz. The camera frame rate is set to 200 Hz. The pump beam is modulated at 100 Hz such that odd frames are IR-on (Hot) and even frames are IR-off (Cold). Time delay t_d between the pump and probe beams are controlled for transient thermal response measurements and maximized photothermal signal. Zoom-in shows the pump and probe pulses monitored by an oscilloscope. (b) Block diagram of electronic connections for system control and signal detection. The pulse generator generates the master clock at 200 kHz and triggers the components at the aforementioned frequencies. (c) Experimental photothermal image calculation by subtracting the cold frame from the hot frame. The sample is 500 nm PMMA beads on the nitride substrate. The IR wavelength is tuned to the 1729 cm^{-1} vibrational peak of the C=H bond. 97

5·8 Bond-selective interferometric imaging of PMMA thin-film on top of a silicon substrate. Interferometric MIP images at C=O stretching absorption peak of 1729 cm^{-1} and off-resonance wavenumber of 1600 cm^{-1} . The dashed square indicates the region of interest in the analyzed photothermal images. Photothermal image acquisition time: 10 s (1000 frames). IR power: 6.05 mW @ 1729 cm^{-1} and 5.73 mW @ 1600 cm^{-1}. Scale bar: 20 µm 99

5·9 SNR analyis. (a) Calculated noise in a single photothermal image for different collected photons (P). The fitted curve ($\alpha P^{0.498}$) has a slope of 0.498 in logarithmic scale, indicating shot-noise-limited detection. The total number of electrons in a single pixel is nearly 10 ke-. (b) Photothermal SNR calculated for different number of frames (N) averaging. The fitted curve ($\alpha N^{0.505}$) has a slope of 0.505 in logarithmic scale, indicating random noise-source with minimal mechanical instability and fixed pattern artifacts. 100

5·10 Bond-selective interferometric imaging of 500 nm PMMA beads. (a) Interferometric cold image. (b-c) Interferometric MIP images at C=O stretching absorption peak (1729 cm^{-1}) and off-resonance (1600 cm^{-1}), respectively. (d) Cross-section profile indicated by the white dashed line along the single bead in (b). The FWHM of the Gaussian fit is nearly 300 nm. The minimum and maximum points coincide at 500 nm separation ($\Delta_{feature} = 500$ nm). The beads in the interfaces appears to be Gaussian-shaped objects with ($\Delta_{bead} = 350$ nm), resulting in the deconvolved PSF with 357 nm FWHM ($\Delta_{PSF} = \sqrt{\Delta^2_{feature} - \Delta^2_{bead}} = 357$ nm). Photothermal image acquisition time: 50 s. IR power: 2 mW @ 1729 cm^{-1} and 3.8 mW @ 1600 cm^{-1}. Scale bars: 10 µm 101

5·11 Experimental validation of photothermal image formation modeling. (a) Experimental and (b) simulated photothermal image of a 500 nm PMMA bead at 1729 cm^{-1}. (c) Modulation depth ($\Delta I/I$) cross-section profiles in (a-b). (d) Temperature change (ΔT) histogram of the detected 500 nm PMMA beads. The temperature change is calculated at each bead's peak contrast using the linear relationship with the modulation depth. Scale bar: 1 µm. 103

5·12 Transient temperature response analysis. Experimental and simulated transient temperature response for 56 particles. The temperature decay time constant is 915 ns. 104

5·13 Photohermal signal stability in frame averaging. The phothothermal SNR of 500 nm PMMA beads calculated at different number of frames averaging. The experimental data is fit to an exponential function $y = \alpha x^n$ with n = 0.43. IR power: 6 mW @ 1729 cm^{-1}. 105

5·14 Photothermal signal of 500 nm PMMA beads at different number (N) of averaged frames. $P_{pump} =$, $\tilde{\nu}_{pump} = 1729\ cm^{-1}$ vibrational peak of the C=H bond, camera FPS: 400 Hz, scale bar: 10 μm. 106

5·15 Bond-selective interferometric imaging of *S. aureus* bacteria. (a) Interferometric cold image. (b-d) Multi-spectral MIP images at discrete wavenumbers; (b-c) Amide I (1650 cm^{-1}) and II (1549 cm^{-1}) bands, and (d) C=O bond (1729 cm^{-1}). The left two arrows in DC image (a) indicates sample like features which disappear in MIP images. The upper right arrow indicates that the negative interferometric contrast from *S. aureus* due to its size appears to be negative in the MIP images. IR powers: 12.4 mW @ 1650 cm^{-1}, 9 mW @ 1549 cm^{-1}, and 6.05 mW @ 1729 cm^{-1}. Photothermal image acquisition time: 50 s (5000 frames). Scale bars: 10 µm 107

5·16 Bond-selective interferometric imaging of *E. coli* bacteria. (a) Interferometric cold image. (b-d) Multi-spectral MIP images at discrete wavenumbers; (b-c) Amide I (1650 cm^{-1}) and II (1549 cm^{-1}) bands, and (d) C=O bond (1729 cm^{-1}). IR powers: 12.4 mW @ 1650 cm^{-1}, 9 mW @ 1549 cm^{-1}, and 6.05 mW @ 1729 cm^{-1}. Photothermal image acquisition time: 50 s (5000 frames). Scale bars: 10 µm 109

5·17 Bond-selective interferometric imaging of *C. albicans*. (a) Interferometric cold image of *C. albicans*. (b-d) Multi-spectral MIP images at discrete wavenumbers; (b) protein Amide I band (1650 cm^{-1}), (c) CH_2 bending (1450 cm^{-1}) in lipid and protein bonds, (d) off-resonance (1800 cm^{-1}), and (e) C=O stretching (1742 cm^{-1}) in phospholipid esters. (f) Cross-section profile indicated by the white dashed line along the lipid droplet in (e). The FWHM of the Gaussian fit is 1.64 µm. IR powers: 11.35 mW @ 1650 cm^{-1}, 11 mW @ 1450 cm^{-1}, 8.7 mW @ 1800 cm^{-1}, 12.9 mW @ 1742 cm^{-1}. Photothermal image acquisition time: 20 s (1000 frames). Scale bar: 20 µm 110

List of Abbreviations

AOM	Acousto-Optic Modulator
BNP	Biological Nanoparticle
CCD	Charge-Coupled Device
CMOS	Complementary Metal–Oxide–Semiconductor
DC	Direct component
DPC	Differential Phase Contrast
EBL	Electron Beam Lithography
FFT	Fast Fourier Transform
FOV	Field-of-View
FPM	Fourier Ptychographic Microscopy
FWHM	Full Width Half Maximum
IR	Infrared
LED	Light-Emitting Diode
mid-IR	mid-infrared
MIP	Mid-Infrared Photothermal
NA	Numerical Aperture
OD	Optical Density
PLGA	Poly(lactic-co-glycolic acid)
PMMA	Polymethyl methacrylate
PS	Polystyrene
PSF	Point Spread Function
PT	Phototothermal
SHG	Second Harmonic Generation
SNR	Signal-to-Noise Ratio
SPIR	Single-particle Interferometric Reflectance
TF	Transfer Function
VLP	Virus Like Particle
VSV	Vesicular Stomatitis Virus
WIM	Wide-field Interferometric Microscopy

Chapter 1

Introduction

Nanoparticles are particles with a size range of 10 - 100 nm at least in one dimension. They have enormous utility as well as potential adverse impacts in biotechnology, human health, medicine, and food safety [Luan et al., 2017, Newell et al., 2010]. Characterization and utilization of nanoparticles have led to many advancements in medical diagnostics [Kairdolf et al., 2017], therapeutics [Kamaly et al., 2012], drug delivery [Prausnitz et al., 2004], environmental monitoring [Rassaei et al., 2011], and homeland security [Golightly et al., 2009]. As a naturally occurring nanoparticle class, biological nanoparticles (BNPs) are highly diverse and have unique functional implications in biological science. Viruses, for instance, are one of the most abundant BNPs on earth [Flint et al., 2020] and have caused deadly outbreaks throughout human history, with the stark and enduring example embodied in the recent global COVID-19 pandemic. Exosomes, another class of BNPs, are 30-200 nm diameter vesicles secreted from cells, containing a rich cargo of proteins, lipids, and nucleic acids, and play a key role in human health and diseases as they transfer signals from one cell to other cells [Pegtel and Gould, 2019]. Physical and chemical properties of these BNPs strongly influence their circulation [Geng et al., 2007], biodistribution [Wu et al., 2015], cell entry pathways [Rejman et al., 2004], and clearance *in vivo* [Bruckman et al., 2014]. For example, viruses and mycoplasmas exist in various geometries, *i.e.*, rods, and spheres, with sizes ranging from tens to hundreds of nanometers. Rod- and disk-shaped particles can tumble and flow close to blood vessel walls in contrast to spherical particles that tend to follow laminar flow along the center [Cooley et al., 2018]. Virus shape can also increase transmission [Welsch et al., 2010, Campbell et al., 2014], allow escape from small molecule antivirals [Vahey and Fletcher, 2019], and aid in evading host responses [Nehls et al., 2019].

Accurate morphological characterization of individual BNPs under optical microscopy could provide valuable insights to advance our understanding of biological mechanisms [Stanley, 2014]. However, light microscopy of these BNPs has two formidable challenges that need to be overcome: (1) weakly-scattering characteristics of BNPs due to their exceptionally small size and low-refractive-index difference with surrounding medium limiting the optical contrast and (2) sub-wavelength spatial resolution limit imposed by the imaging system. Elastically scattered light intensity induced by the illumination scales with the sixth power of the nanoparticle size resulting in very low optical contrast which makes them indistinguishable from the background in scattered intensity-based optical imaging. As an indirect method, fluorescence microscopy has been widely accepted to alleviate this weak contrast by detecting exogenous or endogenous fluorophores. Furthermore, the nonlinearity of fluorescence and stochastic approaches have been utilized to improve the lateral resolution beyond the diffraction limit and led to advancements in super-resolution far-field optical microscopy modalities [Schermelleh et al., 2019] for studying biological specimens in unprecedented details. Yet, fluorescence labeling has practical difficulties and could interfere with sample functionality and structure. Moreover, fluorescence imaging is severely limited by the photophysical properties of fluorescent molecules including phototoxicity, photobleaching, photostability, and saturation. Therefore, overcoming these limitations and enabling label-free (direct) imaging of BNPs in their natural environment and without any modifications would have a significant impact in life sciences [Zanchetta et al., 2017].

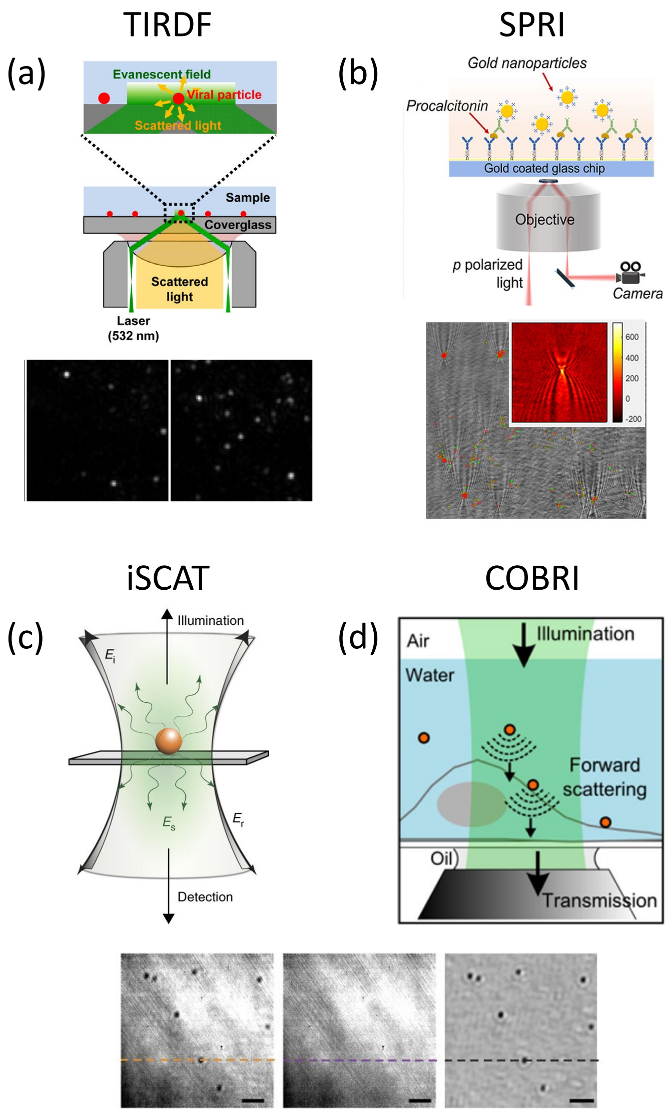
TIRDF
(a)
Evanescent field
Viral particle
Scattered light
Sample
Coverglass
Scattered light
Laser (532 nm)
SPRI
(b)
Gold nanoparticles
Procalcitonin
Gold coated glass chip
Objective
p polarized light
Camera
600
400
200
0
-200
iSCAT
(c)
Illumination
E_i
E_s
E_r
Detection
COBRI
(d)
Air
Illumination
Water
Forward scattering
Oil
Transmission

Figure 1·1: (a) Total internal reflection dark-field microscopy (TIRDF), adapted from [Enoki et al., 2012]. (b) Surface plasmon resonance imaging (SPRI), adapted from [Jing et al., 2019]. (c) Interferometric scattering (iSCAT) microscopy, adapted from [Arroyo et al., 2016]). (d) Coherent brightfield (COBRI) microscopy, adapted from [Huang et al., 2017].

Recent advances in label-free optical microscopy have enabled highly sensitive direct imaging of BNPs by various contrast enhancement methods [Enoki et al., 2012, Jing et al., 2019, Piliarik and Sandoghdar, 2014, Cheng et al., 2019, Daaboul et al., 2010]. Dark-field microscopy realizes the high optical contrast detection of the scattered intensity by suppressing the illumination background using a dark-field condenser or total internal reflection phenomenon. Yet, the sixth-power dependence of the scattering intensity limits the detection sensitivity and applications of dark-field techniques due to stray light and small dynamic range. Surface plasmon resonance imaging, another scattering-intensity only detection scheme, increases the optical excitation by utilizing plasmonic enhancement nearby a thin layer of gold surface atop of glass substrate. However, the plasmonic imaging technique has a highly distorted and aberrated point spread function, limiting its ability to distinguish densely populated nanoparticles [Huang et al., 2020]. Nevertheless, interferometric scattering detection techniques offer coherent detection of the elastically scattered field – rather than its square or intensity – mixing with a strong reference field in a common-path interferometry configuration [Avci et al., 2015]. The interferometric detection enjoys a reduced size dependence of contrast (scaling with the third power of the particle size) and enables a significant enhancement of nanoparticle visibility. Over the last two decades, wide-field common-path interferometric microscopy techniques have successfully demonstrated high-throughput, sensitive, and fast direct imaging of nanoparticles down to a single protein [Taylor and Sandoghdar, 2019]. The interferometric scattering (iSCAT) [Ortega Arroyo et al., 2014] microscopy detects nanoparticles captured on a glass substrate in reflection mode. The sample is illuminated with a highly coherent light source, *i.e.,* laser, to increase the interferometric contrast. Similarly, coherent brightfield (COBRI) microscopy uses laser illumination in transmission mode followed by background attenuation in the pupil plane to reveal high interferometric contrast [Cheng et al., 2019]. However, laser-based illumination causes spurious background due to the coherent artifacts from the substrate and optics surfaces. To reduce these artifacts, complex, expensive, and bulky components such as acousto-optic-modulator are used, followed by computational background subtraction algorithms that extract the subtle signal contrast buried under the coherent noise artifacts [Ortega Arroyo et al., 2014]. Moreover, these artifacts significantly reduce the observation field-of-view (FOV), limiting the nanoparticle detection throughput. Thus, laser-based illumination could dramatically limit the imaging system's performance.

Single-particle interferometric reflectance (SPIR) microscopy, also known as single-particle interferometric reflectance imaging sensor (SP-IRIS) [Daaboul et al., 2014], has been developed in our group. After its initial inception in 2010, SPIR has been progressively evolving from the proof-of-concept to commercialized products [Daaboul et al., 2016]. SPIR is a simple and low-cost yet powerful microscopy technique that detects nanoparticles captured on SiO_2 layered substrate in the common-path interferometry configuration. To achieve coherent detection with a sufficient coherence length, SPIR uses a partially coherent quasi-monochromatic light-emitting-diode (LED) as the light source. The LED illumination drastically reduces coherent illumination artifacts. Therefore, such low-coherence illumination allows for simultaneous detection and counting of tens of thousands of nanoparticles across large FOVs that are significantly larger than that of iSCAT or COBRI. Several applications for imaging, detecting, and counting of viruses [Daaboul et al., 2010, Daaboul et al., 2014], exosomes [Daaboul et al., 2016, Aygun et al., 2019], and metallic nanoparticles [Sevenler et al., 2018] have been demonstrated. Although SPIR has great advantages, several challenges have not been well addressed in the earlier studies. (1) Use of bright-field-like illumination function and current image reconstruction algorithms provide poor sensitivity below the system's ultimate detection limit. (2) Poor high-frequency Fourier support in classical illumination schemes limits the diffraction-limited resolution to the illumination wavelength scale, providing insufficient resolution to discern nanostructures below 350 nm. (3) The molecular specificity is limited to the surface affinity of the immobilized probes where chemical content and signature of particles are inaccessible.

1.1 Dissertation objectives

In this dissertation, we seek to advance three specific aspects of SPIR microscopy: sensitivity, resolution, and chemical specificity. First, we develop novel optical and computational methods to enhance particle visibility and achieve sensitivity to detect single sub-50 nm low-index nanoparticles. Next, we introduce novel asymmetric illumination with computational imaging to improve the lateral resolution of the system's classical limit and demonstrate morphological visualization of BNPs at the nanoscale. Finally, we develop bond-selective interferometric microscopy to extract chemical signature information by probing the mid-infrared absorption-induced photothermal effect for fingerprinting BNPs. To achieve these goals, we introduce novel analytical physical models in addition to designing and instrumenting new optical imaging systems.

This dissertation is divided into four main chapters. In Chapter 2, we discuss theoretical and experimental considerations in SPIR microscopy. We show the analytical model of the scattered field detection in common-path interferometry configuration. We formulate the light scattering process in the dipole limit. We present an analytical treatment of the light scattering enhancement for particles on top of the layered substrate. System-level design requirements and experimental realizations of SPIR microscopy are included to provide an instrumentation overview. Design and implementation of illumination function engineering for enhanced nanoparticle visibility are studied. Overall, a five-fold contrast improvement over classical fully-open aperture illumination is demonstrated. Shot-noise limited detection is investigated by theoretical analysis and experimental studies. This chapter forms the foundations for the studies discussed in the following chapters.

In Chapter 3, we describe a computational reconstruction framework for analyzing defocus images that capture the unique 3D interferometric signal profile. We develop a computationally- and memory-efficient algorithm to recover high signal-to-noise ratio nanoparticle signal. A vectorial-optics-based linear forward model that relates particle polarizability with the intensity images is formulated for sub-diffraction limited dielectric nanoparticles captured on the layered substrate. This linear forward model has great importance of direct inversion of the captured images. Proof-of-concepts experiments are demonstrated on individual low-index silica nanoparticles in 50 nm nominal diameter with a detection sensitivity of more than 8 SNR. We further extend the forward model to asymmetric illumination for resolution enhancement in the next chapter.

In Chapter 4, we introduce a computational asymmetric illumination method that improves the lateral resolution of the conventional SPIR microscopy two-fold. Simultaneous resolution and contrast improvement is optimized by illumination function engineering. A lateral resolution of 150 nm in interferometric microscopy is achieved over a large FOV. Theoretical considerations and experimental strategies are investigated. Detailed characterization of the resolution improvement is systematically studied on a custom sample fabricated by the electron beam lithography process. Experimental results on spherical and rod-shaped nanocarriers as well as Ebola and vesicular stomatitis viruses demonstrate the relevance to biological systems.

In Chapter 4, we develop a bond-selective interferometric scattering microscope where mid-infrared absorption provides molecular composition insights and wide-field interferometric geometry enables the detection of tens of nanoparticles simultaneously. Chemical imaging is achieved by probing the photothermal effect induced by the vibrational absorption at target molecules. SPIR microscopy is utilized for probing minute changes in the scattered field amplitude as a result of mid-IR absorption. This method provides chemically specific nanoparticle detection in the fingerprint region, for the first time, in wide-field interferometric scattering microscopy. We further discuss the analytical model of the photothermal signal mechanism and underline its physical constitutes. Biological importance is highlighted by chemical imaging of several microorganisms including *Staphylococcus aureus*, *Escherichia coli*, and *Candida albicans*.

1.2 Published work

Most of the work in this dissertation has been published in journal papers, and some are currently under review. The pupil engineering work for visibility enhancement described in Chapter 2 was published in Optica [Avci et al., 2017a]. The reconstruction framework for defocus images described in Chapter 3 was published in Optics Letters [Yurdakul and Ünlü, 2020]. High-resolution computational imaging work using asymmetric illumination described in Chapter 4 was published in ACS Nano [Yurdakul et al., 2020]. The bond-selective wide-field interferometric scattering microscopy work described in Chapter 5 is under review in Journal of Physics D: Applied Physics. The photothermal signal theory in Chapter 5 was partially published in Analytical Chemistry [Zhang et al., 2021]. The photothermal simulations are from our recent work that is under review in ACS Photonics [Zong et al., 2021].

Chapter 2

Theoretical and experimental considerations in single particle interferometric reflectance microscopy

2.1 Introduction

Single-particle interferometric reflectance (SPIR) microscopy visualizes particles captured on a thin film layered substrate in a common-path interferometry configuration, allowing for coherent detection of the elastically scattered field – rather than its intensity. This interferometric detection enjoys a reduced size dependence of signal contrast which scales with the third power of the particle size and enables a significant enhancement of the nanoparticle visibility. In this chapter, we provide an introduction to theoretical and experimental considerations in SPIR microscopy. An analytical model of the light scattering in common-path interferometry is discussed. The theoretical description of interferometric scattering detection forms the basis of this thesis's foundations. Experimental design specifications, optical system implementation, and noise analysis are included to give an overview of the imaging system's instrumentation.

2.2 Common-path interferometic detection

Our implementation of SPIR microscopy utilizes a thin film of SiO_2 thermally grown on a Si substrate. This layered substrate realizes common-path interferometry that

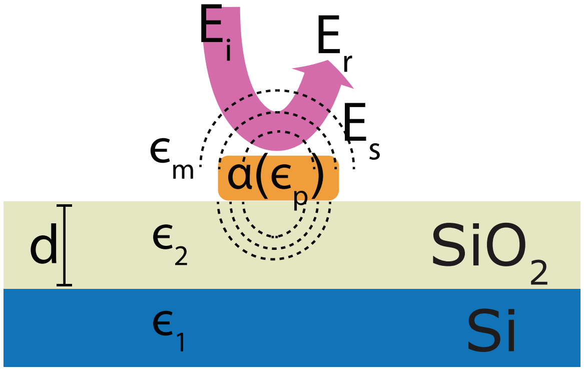

Figure 2·1: Schematic of common-path interferometric detection on SiO_2/Si layered substrate and light-nanoparticle interaction. Incident electric field ($\mathbf{E_i}$) reflects off the substrate surface ($\mathbf{E_r}$) and scatters from nanoparticle ($\mathbf{E_s}$) as a result of particle's polarizability (α).

allows for constructive self-interference of the scattered field from weakly-scattering nanoscale samples as well as provides a reference field through specular reflection (see Figure 2·1). The common-path configuration minimizes possible deviations of the reference arm from the scattered signal arm, in turn, provides highly stable coherent detection of the interferometric signal. This interferometric detection can only be achieved by a narrow-band light source, *i.e.*, laser or light-emitting-diode (LED), with a coherence length longer than an order of magnitude of the layer thickness ($d \sim \lambda/4$, where λ is the illumination wavelength). Although lasers can provide coherence length much longer than LEDs, they can dramatically decrease the system performance due to the speckle noise. The speckle pattern produces contrast variations in the background signal comparable to the interferometric signal [Taylor et al., 2019]. The speckle noise can be reduced by using computational algorithms and optical instruments which are typically bulky, expensive, and complex [Young et al., 2018]. Therefore, SPIR microscopy employs LED as the light source which is a simple and low-cost solution for the interferometric detection of nanoparticles.

We describe the physical model of the SPIR signal under the angular spectrum representation (ASR) framework using the dyadic Green's functions. We provide

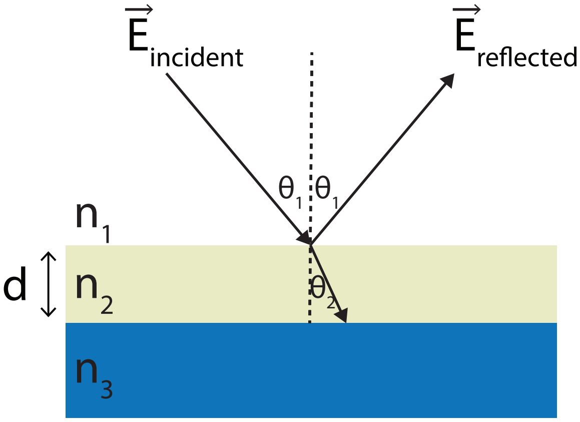

Figure 2·2: Schematic of reflection in a two-layer substrate.

SPIR signal constituents based on the theoretical foundations presented in our group's recent studies in [Avci et al., 2016, Sevenler et al., 2017]. In the common-path interferometry configuration, the incident field $\mathbf{E_i}$ scatters from the sample $\mathbf{E_s} = E_s e^{j\phi_s}$ and reflects off from the layered substrate $\mathbf{E_r} = E_r e^{j\phi_r}$ with a complex reflection coefficient dictated by the thin-film effect. The polarization dependent thin-film reflection coefficients can be written using Fresnel equations as follows [Sennaroglu, 2010]:

$$r^{s,p} = \frac{r_1^{s,p} e^{j\Phi} + r_2^{s,p} e^{-j\Phi}}{e^{j\Phi} + r_1^{s,p} r_2^{s,p} e^{-j\Phi}} \tag{2.1}$$

$$r_1^{s,p} = \frac{N_0^{s,p} - N_1^{s,p}}{N_0^{s,p} + N_1^{s,p}} \tag{2.2}$$

$$r_2^{s,p} = \frac{N_1^{s,p} - N_2^{s,p}}{N_1^{s,p} + N_2^{s,p}} \tag{2.3}$$

$$N_l^s = n_l \cos(\theta_l) \tag{2.4}$$

$$N_l^p = \frac{n_l}{\cos(\theta_l)} \tag{2.5}$$

$$\Phi = k_o n_1 d \cos(\theta_1) \tag{2.6}$$

where s,p superscripts denote the s and p polarizations, N_l denotes the effective direction dependent refractive index in the lth layer with refractive index n_l, Φ denotes optical path difference in the second layer at the thicknes d, θ_l denotes the incident angle at the lth layer as depicted in Figure 2·2. The incident angles at each layer is calculated using the Snell's law. The resulting complex-valued total driving field $\mathbf{E_d}$ becomes the coherent sum of the vectorial incident and reflected fields, $\mathbf{E_d} = \mathbf{E_i} + \mathbf{E_r}$. The scattered field amplitude $|E_s|$ scales with the total driving field $\mathbf{E_d}$ and particle polarizability α in the quasi-static dipole limit (r$\ll \lambda$) where the particle size r is much smaller than the illumination wavelength λ [Novotny and Hecht, 2006]. The resulting far-field scattered field can be expressed as follows:

$$\mathbf{E_s} = \frac{k_0^2}{\epsilon_0}\overset{\leftrightarrow}{\mathbf{G}}_{\mathbf{s}}\mathbf{p} \tag{2.7}$$

$$\mathbf{p} = \epsilon_m \overset{\leftrightarrow}{\alpha}\mathbf{E_d} \tag{2.8}$$

where $\overset{\leftrightarrow}{\mathbf{G}}_{\mathbf{s}}$ is the sum of the primary $\overset{\leftrightarrow}{\mathbf{G}}_{\mathbf{0}}$ and the reflected $\overset{\leftrightarrow}{\mathbf{G}}_{\mathbf{r}}$ dyadic point spread functions (PSFs) in the far-field, $\mathbf{p}$ denotes the dipole moment induced by the driving field at the sample plane, $\overset{\leftrightarrow}{\alpha} = \overset{\leftrightarrow}{I}\alpha$ denotes the particle polarizability tensor, and k_0 denotes the wavenumber in vacuum. In the dipole limit, the polarizability of a spherical nanoparticle is given as follows [Hulst and van de Hulst, 1981]:

$$\alpha = 4\pi r^3 \epsilon_m \frac{\epsilon_p - \epsilon_m}{\epsilon_p + 2\epsilon_m} \tag{2.9}$$

$$\overset{\leftrightarrow}{I} = \begin{bmatrix} 1 & 0 & 0 \\ 0 & 1 & 0 \\ 0 & 0 & 1 \end{bmatrix} \tag{2.10}$$

where r is the particle's radius, ϵ_p is the particle's dielectric constant, and ϵ_m is the medium's dielectric constant. Equation 2.9 indicates that scattered intensity is a function of the particle's volume square ($V^2 \propto r^6$) and the refractive index difference between the particle and its surrounding medium. The volume dependence of the scattered signal has strong implications on the pure scattering intensity-based detection (e.g., dark-field [Horio and Hotani, 1986]) of very small nanoparticles since the scattered signal rapidly falls off as a result of r^6 dependence. Nevertheless, the interferometric detection reduces this square dependence to a linear detection of the scattered field such that the measured signal scales with r^3 instead. In the interferometric microscopy, the detector captures the intensity signal from the coherent sum of reference and scattered fields I_{det} as follow:

$$\begin{aligned} I_{det} &= |\mathbf{E_r} + \mathbf{E_s}|^2 \\ &= |E_r|^2 + |E_s|^2 + 2|E_r||E_s|\cos(\theta). \end{aligned} \tag{2.11}$$

The first term denotes the reflected field intensity $I_r = |E_r|^2$, the second term denotes the scattered field intensity $I_s = |E_s|^2$, and the last term denotes the interference signal $2Re\{\mathbf{E_r}\mathbf{E_s}^*\}$. The phase term $\theta = \phi_r - \phi_s$ denotes the phase difference between complex reflected and scattered fields. This phase term has strong implications on signal constituents as it allows for accurate particle size information [Sevenler et al., 2017], dielectric characteristics [Avci et al., 2016, Avci et al., 2017b, Yurt et al., 2012], and its axial position [Taylor et al., 2019]. For the sake of brevity, we take the phase term as 1 in our formulation, providing the maximized interference signal. Due to r^6 dependence of scattered intensity, the nanoparticles of interest scatters very weakly. Under this approximation, the scattered intensity becomes negligible compared to the reference intensity. Therefore, the detected signal can be approximated as $I_{det} \approx |E_r|^2 + 2|E_r||E_s|$. This enables the coherent detection of the weakly-scattered field with a strong reference. The reflected field intensity constitutes the direct component intensity contribution which can be subtracted by simple background subtraction. Here, we define interferometric signal (S) as the background ($B = I_r$) subtracted intensity signal as follows:

$$S = I_{det} - I_r = 2|E_s||E_r|. \tag{2.12}$$

The interferometric detection realizes the linear detection of the scattered field which is proportional to r^3 whereas the scattering intensity is proportional to r^6 that causes read-noise limited signal fall-off for sub-wavelength particles as in conventional dark-field detection schemes. Thus, interferometric detection leads to high signal-to-noise-ratio (SNR) imaging of small scatterers that generate subtle light scattering contrast above the strong background signal. We further define the interferometric image contrast as the ratio of the interferometric signal to the background intensity as follows:

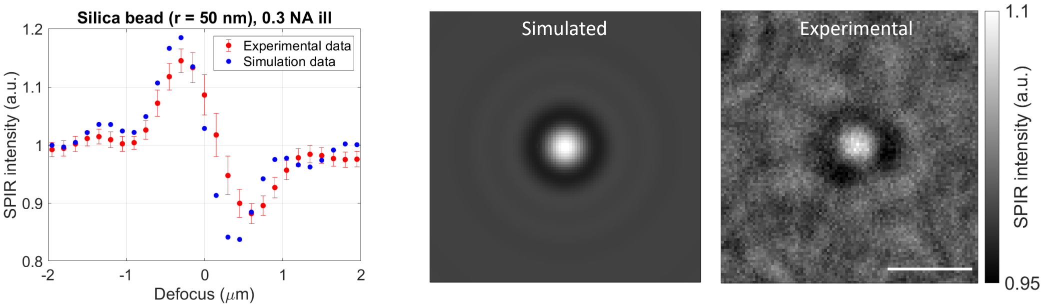

Figure 2·3: Experimental and simulation data for 100 nm silica beads in diameter (r = 50 nm). Scale bar is 1 µm.

$$S_c = \frac{S}{B} = \frac{I_{det} - I_r}{I_r} = 2\frac{|E_s|}{|E_r|}. \tag{2.13}$$

The equations above describe the scattered field as a result of dipole moment induced by an individual plane wave illumination. We perform theoretical simulations on a custom-developed electromagnetic simulation software on MATLAB. This dipole model shows a great agreement with experiments and a more comprehensive electromagnetic model for particles up to 200 nm in diameter [Sevenler et al., 2017]. Figure 2·3 experimentally shows the consistency with the simulations. Our simulation can be compartmentalized into two main parts: (1) substrate and particle geometry and dielectric coefficients to define the dipole moment and (2) optical system parameters including objective numerical aperture and illumination function to calculate the point spread function. Accordingly, we assume the particles are placed on top of the layered substrate at a height of the particle's radius. The dipole moment is calculated using the polarizability tensor and total driving electric field. The scattered fields are then calculated using far-field Green's functions. The reflected field is calculated using Fresnel's coefficients considering incidence angle and polarization. Both reflected fields and scattered far fields are mapped into the image space using the ASR treatment. Then, image fields are obtained by the incoherent sum of the resulting fields using equation 2.11 over the angles constrained by the objective lens numerical aperture as follows:

$$I_{det} = \sum_{\mathrm{m} \in \mathrm{NA}} |\mathbf{E_{r,m}} + \mathbf{E_{s,m}}|^2 \tag{2.14}$$

where m denotes the individual plane wave illumination. This summation draws similarities to the integral over pupil function in many other forward models. The ASR treatment enables simulating arbitrary illumination functions. This capability is the basis of PSF calculations in the following chapters.

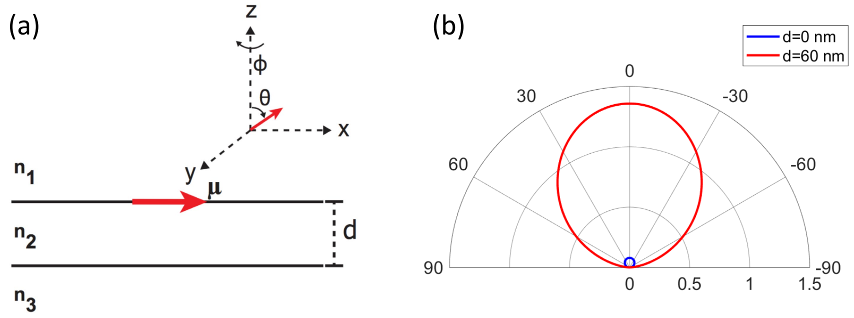

Figure 2·4: (a) Horizontally (in x) oriented dipole in air on top of SiO_2/Si layered substrate. (b) Normalized dipole radiation profile in collection direction (+z) for SiO_2 thickness d at 0 and 100 nm. $n_1 = 1$, $n_2 = 1.47$, $n_3 = 5.14$ and illumination wavelength is 420 nm.

2.3 Enhancement of scattered light

As discussed above, light scattering from small nanoparticles can be analytically modeled in the dipole limit where nanoparticles have radiation profiles similar to that of dipoles. A dipole's radiation strength at a given direction has a sine function dependence of angle with respect to its dipole moment. The emission falls to zero along the dipole axis. Therefore, a dipole mostly radiates perpendicular to its orientation. Knowing this fact, vertically aligned dipoles radiate at high angles, whereas horizontally aligned dipoles radiate at a small angle with respect to the surface normal. The dipole radiation near a planar surface needs to be carefully considered due to reflections from the surface boundaries. Such radiation in the vicinity of the layered substrate has been formulated and theoretically discussed in [Novotny and Hecht, 2006]. This dipole radiation theory considers polarization of the emission using dyadic Green's functions in the far-field. To understand the effect of the layered substrate on scattered light radiation patterns, we simulate both horizontal and vertical dipoles placed on top of the SiO_2/Si substrate. Figure 2·4a and 2·5a show the schematics in the simulation configurations. The z-axis is defined as the optical axis with respect to the collection direction. As shown in Figure 2·4b, the horizontal dipole power mainly falls into the collection angles. The vertical dipole has a radiation pattern similar to rabbit ears radiation profile around 60° due to the reflection from the substrate surface as shown in Figure 2·5b. This leads to a poor light scattered collection in the vertical dipole case. Therefore, the horizontally induced dipole can effectively generate more signal in the far-field microscopy configuration due to the limited angular allowance of objective numerical aperture, which is typically in the range of 0 - 60°. Furthermore, we investigate layer thickness effect on radiation power. It is clearly seen that layer thickness at d = 60 nm significantly ($>$ 15-fold) enhances the scattering intensity and its directivity for horizontally aligned dipole.

The vertical dipole emission strength is reduced by nearly two-fold at the 60 nm oxide layer thickness. Indeed, illumination in SPIR can be engineered such that particles are polarized mostly in the horizontal direction as discussed below.

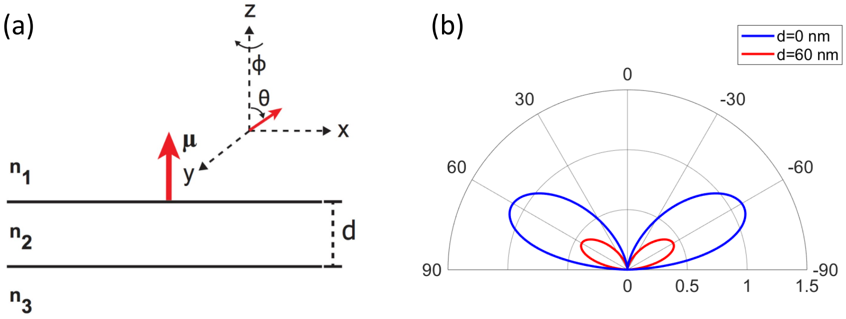

Figure 2·5: (a) Vertically (in z) oriented dipole in air on top of SiO_2/Si layered substrate. (b) Normalized dipole radiation profile in collection direction (+z) for SiO_2 thickness d at 0 and 100 nm. $n_1 = 1$, $n_2 = 1.47$, $n_3 = 5.14$ and illumination wavelength is 420 nm.

2.4 Experimental considerations in SPIR

2.4.1 Köhler illumination

Illumination engineering is the key aspect of SPIR microscopy. Enhanced particle contrast or better lateral resolution can be achieved by engineering the illumination function. To realize the illumination engineering in practice, the objective back-pupil plane is accessed through its conjugate plane in Köhler illumination geometry. Figure 2·6 shows the Köhler configuration commonly used in microscopy techniques. The aperture mask (A_{il}) in the source plane is imaged into the objective back-pupil A_{bf} such that these two planes become conjugates of each other. Each point in the light source generates a plane wave that is mapped into the sample plane. The sample is then illuminated by this plane wave at an incident angle defined by the point source's position in the transverse (XY) plane where we consider z as the optical axis. A point source further away from the back pupil's center illuminates the sample at a larger incident angle. The illumination angle can be controlled by changing the aperture mask size. Therefore, the filling factor of the objective pupil in the classical sense (circular filling) relates to the maximum illumination angle on the sample. For the sake of simplicity, we refer filling factor in terms of illumination numerical aperture (NA) which is the sine of the maximum illumination angle. For example, the illumination NA in full factor becomes equal to the objective NA. Nevertheless, Köhler illumination is the key design aspect of the experimental realizations in this thesis, allowing for arbitrary illumination functions to be used for various purposes including visibility and resolution enhancement.

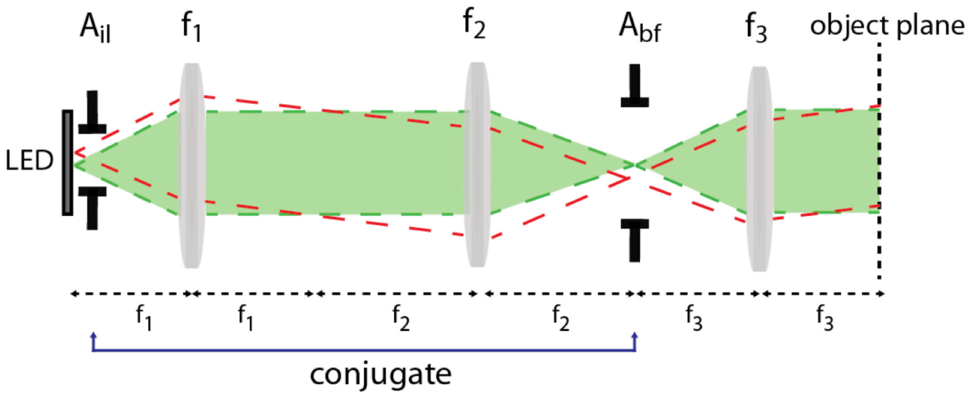

Figure 2·6: Köhler illumination configuration.

2.4.2 Experimental setup

The experimental setup is illustrated in Figure 2·7. A partially coherent light-emitting diode (LED) is butt-coupled to an integrating sphere (Thorlabs, IS200-4). The integrating sphere's inside is coated with highly reflective diffusive coating covering a broad wavelength range of 250 - 2500 nm. Integrating spheres are typically used in light source characterizations and power measurements since they output a highly uniform, nearly Lambertian source pattern. This stems from the fact that the coupled light undergoes numerous (>100) diffusive reflections inside the integrating sphere.

This source scrambling nearly eliminates the spatial coherence while preserving the temporal coherence of the light source. The input LED light beam becomes source-free, uniform, and spatially incoherent at the exit port. Although the Köhler geometry is assumed to provide source-free sample illumination, the non-uniformity of the LED chip image creates inferior interferometric image quality. Moreover, the illumination function engineering can be implemented much easier, assuming the equally weighted plane wave illumination. For these reasons, the integrating sphere is an essential part of our optical instrumentation. Yet, a significant amount of the input light power nearly 93% is lost at the output beam. In other words, only one out of fifteen input photons reaches the output. Therefore, the use of high-power (10 Watts) LEDs becomes necessary to maintain shot-noise-limited sensitivity with enough photon budget. We typically use printed-circuit-board mounted LEDs from LED Engin or Lumileds. We place the LEDs onto custom-designed heatsinks that can directly be mounted on Thorlabs mounts (SM1). To drive the LEDs at constant current, we design and make custom PCBs that can accommodate up to three high-power LEDs simultaneously.

To have control over the illumination function, we employ Köhler illumination configuration discussed above. In practice, an adjustable aperture diaphragm is mounted right after the integrating sphere's exit port. The aperture is imaged into the objective back-focal plane through a 1:1 4f-system consisting of two identical lenses. By doing so, the aperture diaphragm and objective back-pupil become conjugate planes as shown by red dashed lines in Figure 2·7. Since object back-pupils are typically within the objective at an unknown position, the condenser lens position should be carefully determined using shear plates, to form a 4f system with the objective lens. To do that, a collimated laser source at a wavelength close to that of the imaging system can be used. We typically align the optical system with a 532 nm laser, providing

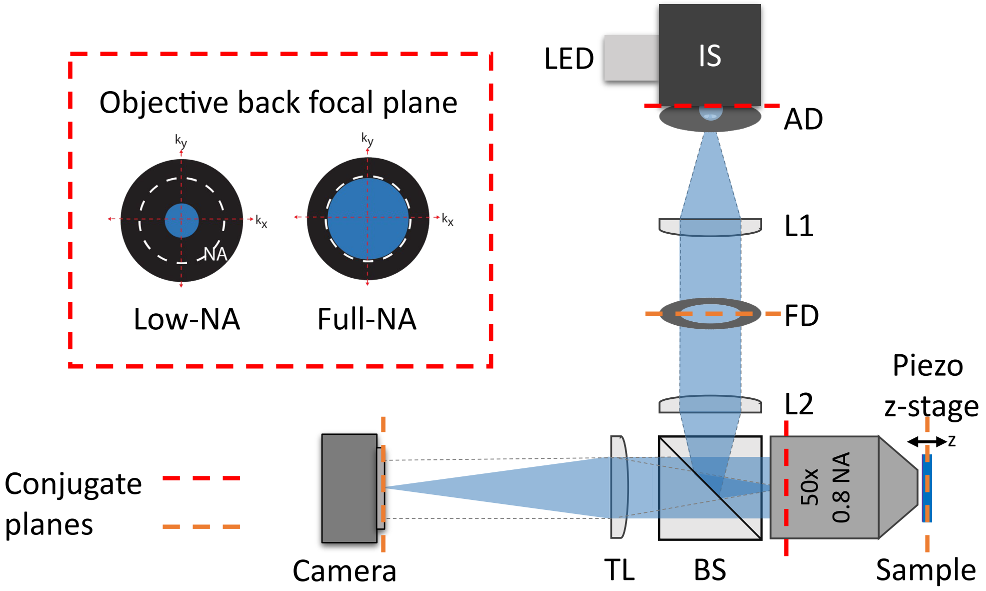

Figure 2·7: (a) Schematic of the SPIR microscope. IS, integrating sphere; AD, aperture diaphragm; FD, field diaphragm; L, lenses; BS, beam splitter; TL, tube lens; NA, numerical aperture.

enough proximity owing to the achromatic lens selection in the instrumentation. The lens focal length should be sufficient to reach the back-pupil plane beyond the beam-splitter. 60 mm achromatic lenses provide enough space for such alignment in the case that the objective is directly mounted on the beam splitter. Another aperture, namely the field diaphragm, is placed at the sample conjugate plane to control the field-of-view (FOV) and minimize the stray light coupled into the system.

Samples are typically placed on a custom-built vacuum chuck that is mounted on a 3-axis flexure stage with differential actuators. The vacuum chuck is of great use in horizontal setup configurations for stable image acquisitions. The sample is scanned along the optical axis with a piezo actuator. A high-NA microscopy objective lens from Nikon is used in epi-configuration. We use an infinity-corrected tube lens with 200 mm focal length that is optimized for infinity-corrected objectives. The focal length of the lens is determined by the objective's manufacturer. Nikon objectives are typically designed for 200 mm focal length tube lenses. The sample image is

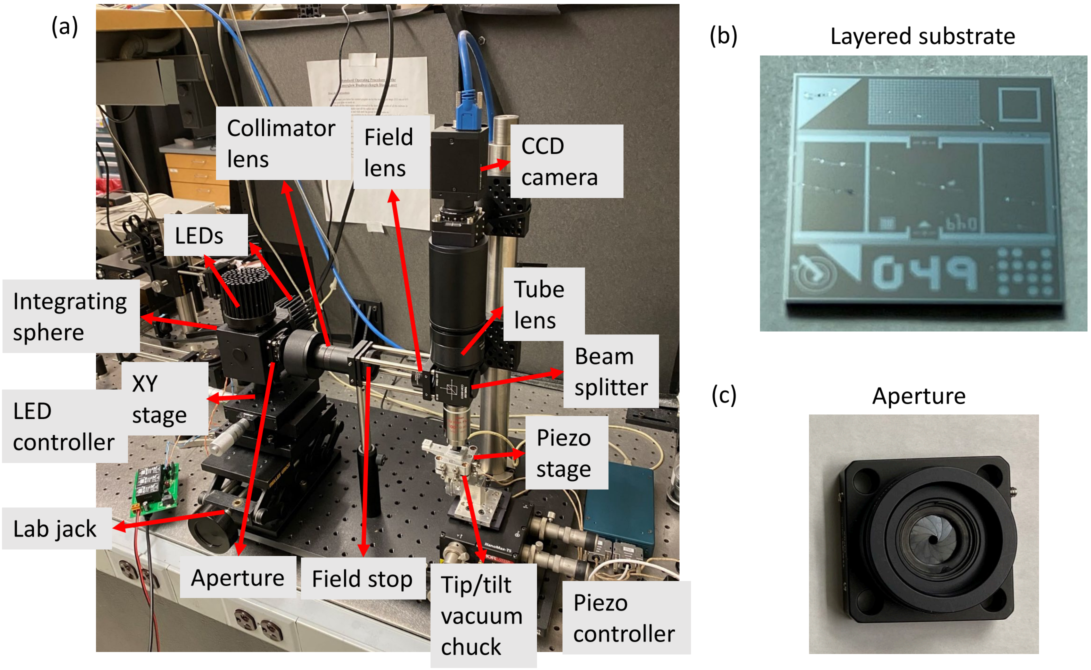
(a)
Collimator lens
Field lens
CCD camera
LEDs
Integrating sphere
Tube lens
Beam splitter
XY stage
LED controller
Piezo stage
Lab jack
Aperture
Field stop
Tip/tilt vacuum chuck
Piezo controller
(b)
Layered substrate
049
(c)
Aperture

Figure 2·8: (a) Picture of SPIR microcope, (b) SiO_2/Si chip, and (c) adjustable aperture

captured by an area-scan camera with a large image sensor that could be a charge-coupled device (CCD) or complementary metal-oxide-semiconductor (CMOS). The image sensor choice is critical such that the pixel size should satisfy the Nyquist sampling rate to avoid aliasing. The pixel size should sample twice the imaging system's diffraction-limited resolution at the detector plane. This condition for the sampling rate can be written as follows:

$$2 \times \text{Pixel size} \leq \text{Projected size} \tag{2.15}$$

$$\text{Projected size} = \text{Diffraction-limited resolution} \times \text{Objective magnification} \tag{2.16}$$

$$\text{Diffraction-limited resolution} = \frac{\lambda}{2NA} \tag{2.17}$$

$$\text{Pixel size} \leq \frac{\lambda}{4NA} \times \text{Objective magnification} \tag{2.18}$$

For example, 50 × 0.8 NA objective at wavelength 460 nm has a diffraction-limited resolution of 288 nm. The projected spot size is 14.4 µm. Using the equations above, the maximum pixel size required to resolve the features is 7.2 µm. This limit can be relaxed depending on the illumination condition. The diffraction-limited resolution for a nearly normal incident angle is about λ/NA. In that case, the pixel size should be smaller than 14 µm. In our studies, we use global shutter SONY image sensors with pixel sizes less than 3.5 µm. These cameras provide a sufficient sampling rate to resolve diffraction-limited spots in our images.

Our setup is shown in Figure 2·8a. This setup is used in our high-resolution imaging study discussed in Chapter 4. Two custom-built high-power LEDs are mounted on the integrating sphere. The custom-built PCB board controlled by Arduino provides constant current to the LEDs. The aperture is imaged into the back focal plane of the microscope objective (100×/0.9 NA) in Köhler geometry discussed above. To maximize the illumination power, we build the 4f system at unit magnification using two 60 mm focal length achromatic doublets. The custom-built vacuum chuck with a tip/tilt function is mounted on a closed-loop piezo actuator. The tip/tilt stage is essential to correct for aberrations across the entire FOV, particularly at high NA objectives.

Figure 2·8b shows the typical SiO_2/Si layered substrate used in our studies. The chips are fabricated by Silicon Valley Microelectronics with a custom lithography mask design. It is composed of single side polished silicon with 60 nm thermally grown oxide layer atop. The bright patterns are silicon regions that are etched down for chip identification. There are also micron-scale L-shape patterns repeated nearly every 150 µm, providing reference regions for nominal focus finding. Figure 2·8c is the picture of an adjustable aperture diaphragm whose opening controls the illumination NA.

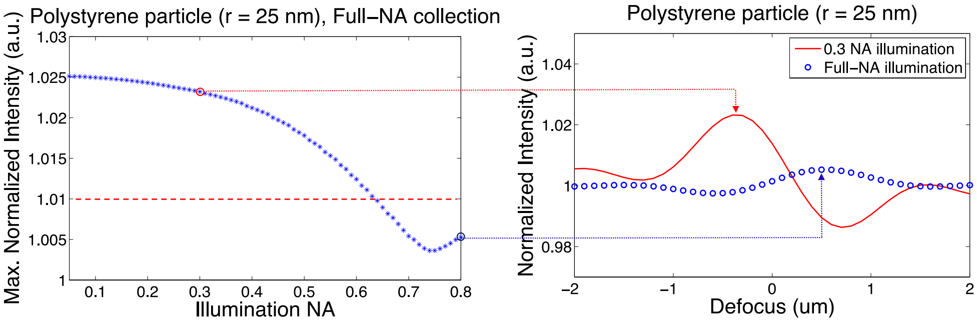

Figure 2·9: (Left) Simulations for nanoparticle signal with respect to illumination NA. The red dashed line around 1.01 indicates the limit of detection in terms of particle visibility for a 10 ke- pixel full-well-capacity. (Right) Simulated defocus scans of low-NA (0.3) and full-NA (0.8) illuminations.

2.4.3 Illumination engineering for enhanced visibility

The illumination function is critical for particle visibility and resolution in SPIR microscopy. In this discussion, we focus on the illumination NA effect on nanoparticle visibility. We follow the dipole theory discussed above. The dipole orientation has angular dependence on the plane wave illumination's incidence angle. The vertical dipole excitation increases as the incidence angle increases. This results in poorly collected light scattering which is mostly outside the angular range of the objective NA as shown in Figure 2·5b. On the other hand, the horizontal dipole radiation above the layered substrate is enhanced and mostly within the objective NA range. In epi-illumination, the illumination light specularly reflects from the substrate surface and is collected by the objective. As a result, the low-angle illumination enhances nanoparticle visibility compared to that of high-angle illumination.

To demonstrate the enhanced visibility, we first simulate the illumination NA effect on interferometric contrast as shown in Figure 2·9. We calculate the 50 nm polystyrene particle response on a 100 nm SiO_2/Si substrate for the illumination NA ranging from 0.05 to 0.8 NA. The particle contrast curve decreases as a slowly varying

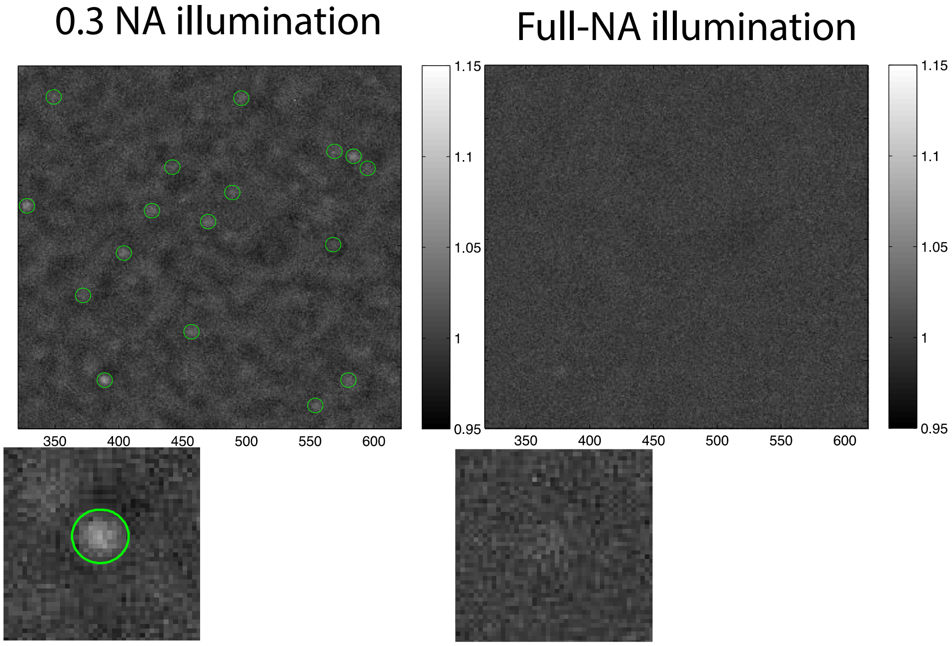

Figure 2·10: Background-normalized SPIR images of polystyrene beads with 50 nm nominal diamater at their highest signal defocus plane for 0.3 NA and full-NA configurations.

function of the illumination NA, converging to a plateau at normal incidence. One can place a pinhole to illuminate the sample nearly at the normal angle. However, this is not generally practical due to the significant power loss that requires a long exposure time. Owing to the slowly varying dependency, we can set illumination NA in the range of 0-0.4 NA without significantly sacrificing contrast loss and enjoy the shot-noise-limited sensitivity at a reasonable exposure time. For example, 0.3 NA illumination provides a five-fold contrast improvement over 0.8 NA illumination. In practical implementation, we greatly benefit from Köhler illumination configuration. Since each point at the objective back pupil illuminates the sample at an angle defined by its transverse position, the maximum illumination angle can be controlled by setting the aperture diaphragm opening. We define two illumination conditions: (1) low-NA which partially fills the back pupil and (2) full-NA which fills the entire back pupil as shown in Figure 2·7. Figure 2·10 compares SPIR images obtained at low-NA (0.3) and full-NA (0.8) illuminations. The visualized images are from the highest contrast defocus plane. The 0.3 NA illumination provides enhanced nanoparticle visibility whereas the particles are indistinguishable from the background signal in the full-NA illumination case. Therefore, we employ low-NA illumination as a standard in sensing applications where sensitive detection and enumeration of individual nanoparticles are desired.

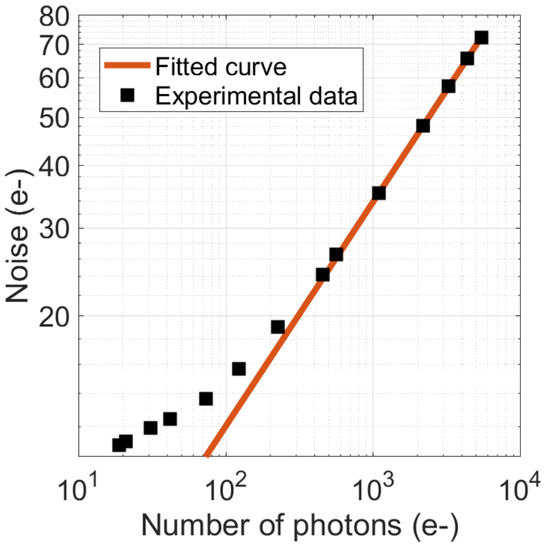

Figure 2·11: Calculated noise in a single image for different collected photons (P). The fitted curve ($\alpha P^{0.45}$) has a slope of 0.45 in logarithmic scale, indicating shot-noise-limited detection. The total number of electrons in a single pixel is nearly 6 ke-.

2.4.4 Noise characteristics

Unlike fluorescence microscopy which is photon-budget limited, the bright-field illumination can easily saturate the camera pixels and bring the imaging system into the shot-noise regime where all other noise sources, i.e., electronic and thermal, are negligible. The noise floor in a single interferometric measurement is dominated by the photon noise of photoelectrons accumulated at the detector during the integration time. This is a valid assumption for background light that generates enough photons (P) to saturate the detector within a given short exposure time of a few milliseconds. Thus, SPIR in principle enjoys the shot-noise limited sensitivity. Noise fluctuations in a single pixel can be expressed as the root sum squares of the noise sources in the system,

$$\sigma_e = \sqrt{\sigma_c^2 + \sigma_s^2} \tag{2.19}$$

where σ_e is the effective noise, σ_c is the camera's temporal dark noise, and σ_s is the photon shot-noise. The shot-noise fluctuation is equal to the standard deviation of the detected photons $\sigma_{photon} = \sqrt{P}$. We investigate the noise source in our camera (SONY CCD image sensor (GS3-U3-120S6M-C) which has a 54.63 dB dynamic range with a saturation capacity of 6125 e- and temporal dark noise of 10.87 e-). In such a large dynamic range camera where $\sigma_s^2 \ll \sigma_s^2$, σ_e can be approximated as σ_s even if saturating 20% of the pixel wells. We experimentally evaluate the noise in our imaging system. We measure the noise in difference images of the same FOV captured at various numbers of collected photons (P). The difference image is calculated from two frames captured subsequently without any change in the illumination conditions. This minimizes background fluctuations due to the collection optics. Figure 2·11 shows our noise calculations in the logarithmic scale. The fitted curve as a function of P is $\alpha P^{0.45}$ with a constant scaling factor of α. The curve exponent is very close to the theoretical value of 0.5. This indicates that our camera grants the shot-noise-limited detection for sufficiently saturated frames. The shot-noise-limited sensitivity starts deviating around 3% saturation level in which the camera read-noise becomes more pronounced. Nevertheless, LEDs can provide sufficient light power to nearly saturate the camera pixels, providing the shot-noise-limited detection sensitivity.

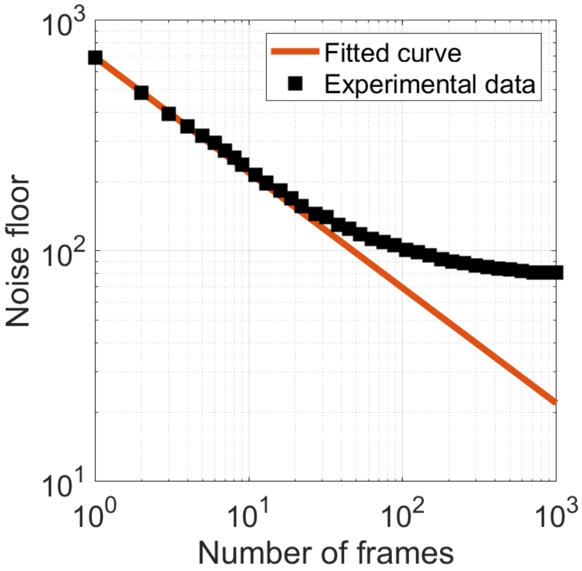

Figure 2·12: Noise-floor calculated for different number of frames (N) averaging. The fitted curve ($\alpha N^{0.5}$) has a slope of 0.5, theoretical expected value for random noise.

The signal-to-noise ratio (SNR) in SPIR can be calculated using equation 2.19. The reflected intensity is much larger than interferometric term. Since the interferometric contrast is typically a few percent, we can approximate the detected photons as the reflected light intensity, $I_{det} \approx I_{ref}$. In this assumption, the shot-noise is equals to the reflected field amplitude $|E_r|$. Using equations 2.11, 2.12, and 2.13, the SNR can be expressed as follows:

$$\begin{aligned} SNR &= 2|E_s| \\ &= S_c\sqrt{I_{det}} \\ &= S_c\sqrt{P_{det}} \end{aligned} \tag{2.20}$$

The number of detected photons in a single frame is bounded by the camera pixel's full-well-capacity ($P_{det} = P_{FWC}$). Using equation 2.20, the limit of detection in terms of interferometric contrast S_c and P_{FWC} becomes,

$$S_c \geq \frac{1}{\sqrt{P_{FWC}}} \tag{2.21}$$

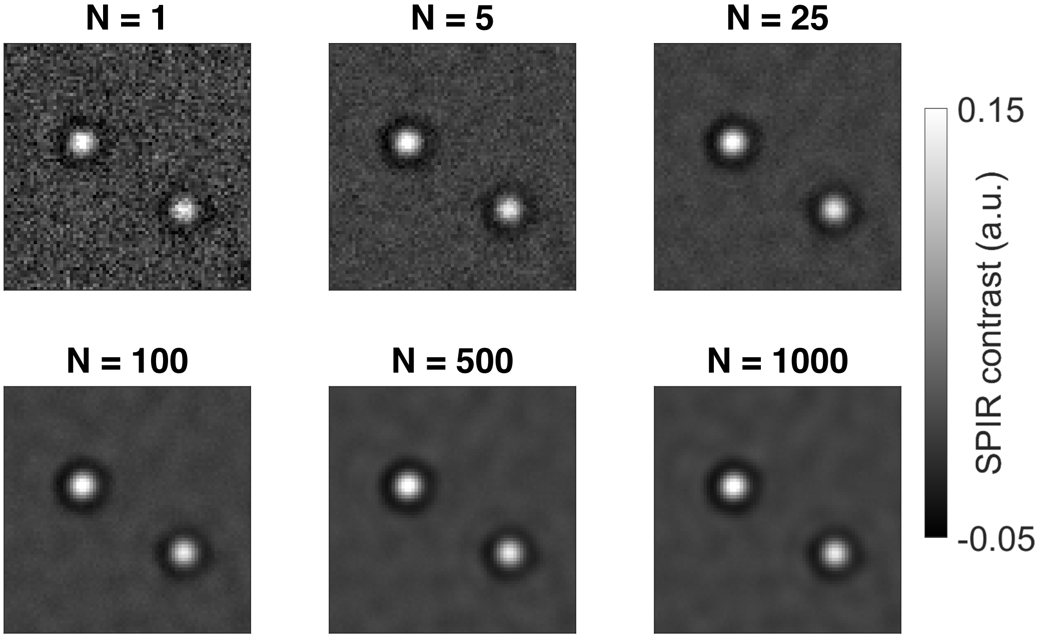

Figure 2·13: SPIR images of 100 nm silica beads at different number (N) of averaged frames.

This equation indicates that the interferometric signal in a single frame should be larger than minimum detectable contrast $1/\sqrt{P_{FWC}}$, otherwise indistinguishable from the background shot-noise. Therefore, large pixel depth cameras are desirable in shot-noise-limited measurements. Considering the SONY image sensor discussed above, the minimum detectable interferometric contrast becomes 1%. Luckily, the random noise in our measurements can be further reduced by frame averaging. The improved SNR scales with the square root of the number averaged frames N. Figure 2·12 experimentally demonstrates noise-floor with respect to N. The noise is calculated by taking the background standard deviation in each averaged image. To eliminate the stationary (incoherent) background artifacts from back-reflections from optics, we take the difference image at two different defocus planes (peak and dip positions). The experimental data is consistent with the theoretical curve of $N^{0.5}$ which has a slope of 0.5 on the logarithmic scale. However, noise reduction does not enjoy the frame averaging after nearly 25 frames, converging to a plateau. This stems from the fact that the coherent background artifacts in the collection path such as roughness from the substrate and image sensor surfaces become the dominant noise source, limiting the visibility of small nanoparticles. Figure 2·13 further shows the SNR improvement in 100 nm silica bead images averaged at different frames. In SPIR measurements, the substrate surface roughness becomes the ultimate limit since it causes substrate-induced scattering. We anticipate that the substrate surface roughness gives a signal level similar to a 25 nm silica bead placed on the layered substrate. Such scattering artifacts are particularly more obvious for the microarray assays that capture the biological nanoparticles. In real-time experiments, we believe that these background artifacts can be computationally reduced by simply taking differential images over time.

2.5 Conclusion

This chapter summarizes the theoretical and experimental considerations in SPIR microscopy. The analytical model forms the basis of the linear forward model discussed in Chapter 3 and Chapter 4. It is also used for developing photothermal signal theory in Chapter 5. Illumination function requirements for enhanced nanoparticle visibility are theoretically explained and validated by experiments. The shot-noise-limited sensitivity is discussed and experimentally demonstrated. These experimental and theoretical concepts are key to the system-level implementation and evaluation of the presented studies in this dissertation.

Chapter 3

Computational nanosensing from interferometric defocus images

3.1 Introduction

Label-free optical microscopy for the detection and characterization of biological nanoparticles is desirable owing to the simplicity of sample preparation and assays while avoiding detrimental limitations and interference of labeling. Label-free optical imaging techniques rely on optical scattering from these particles and are often very weak due to their small size and low refractive index contrast with the surrounding medium. This results in weak optical contrast that can be difficult to distinguish from the background signal in low signal-to-noise (SNR) measurements. Therefore, improving the sensitivity for such methods has been critical when studying viruses, exosomes, and other biological nanoscale specimens. Common-path interferometric microscopy techniques have successfully overcome this weak contrast limit and achieved remarkable sensitivity levels down to single proteins [Taylor and Sandoghdar, 2019, Cheng et al., 2019, Daaboul et al., 2016]. This superb sensitivity is demonstrated using various optical [Avci et al., 2017a, Cheng et al., 2019] and computational techniques [Ortega Arroyo et al., 2014, Cheng and Hsieh, 2017, Aygun et al., 2019, Trueb et al., 2017, Taylor et al., 2019]. Arroyo *et al.* developed a robust background subtraction method in the presence of moving samples that leave the occupied pixels over the observation time. Iterative background estimation algorithms for nanoparticles moving a much smaller distance than the setup's resolution limit have been also reported [Cheng and Hsieh, 2017]. Recently, computational algorithms for 3D particle localization have been demonstrated by using the experimentally extracted point spread function (PSF) of the imaging setup [Taylor et al., 2019]. In these computational approaches, background subtraction has been imperative in extracting the subtle signal contrast buried under the coherent noise artifacts of the laser-based illumination.

As discussed in Chapter 2, SPIR microscopy enables wide-field interferometric imaging of nanoparticles while significantly reducing the coherent artifacts owing to the incoherent LED illumination. SPIR often employs area scan cameras with large sensor formats (> 1") to record the extended field-of-view (FOV) image data at a single shot. This imaging modality enables low-cost and robust detection and characterization of thousands of nanoparticles simultaneously. In such large FOV imaging, however, a small tilt of the substrate relative to the optical axis creates defocus across the FOV, particularly with high numerical aperture (NA) objectives. Thus, the measured particle contrast exhibits dips, zeros, or peaks depending on the defocus at the different locations over the system's FOV [Trueb et al., 2017]. Furthermore, artifacts from the heterogeneous sensor surface morphology due to the assay capturing, inherent substrate roughness, and reflections from optics in the collection path may hinder the low-SNR signal detection in a single focal plane [Ekiz-Kanik et al., 2017]. A defocus scan can maximize visibility for all particles across the FOV and help to remove the artifacts. Beyond these initial corrections, the defocus images implicitly capture the sample's optical and physical properties [Avci et al., 2016, Yurt et al., 2012]. For these reasons, defocus scans become a typical routine in SPIR experiments. Several computational techniques have been developed for processing the SPIR defocus data [Trueb et al., 2017, Aygun et al., 2019]. Nanoparticle counting and discrimination algorithms using a differential intensity image obtained from multiple defocus images were reported in [Trueb et al., 2017]. Recently, Aygun *et al.* [Aygun et al., 2019] developed correlation algorithms by fitting 1D defocus information at each pixel to improve SNR. However, these techniques rely on either 1D or 2D defocus information and do not fully exploit nanoparticles' rich spatial information in all three dimensions. Moreover, they use computationally expensive and rather slow iterative algorithms.

In this study, we introduce an alternative computational image reconstruction framework for interferometric defocus images of nanoparticles captured on the substrate surface. Our technique reconstructs a single high-SNR image from a defocus image stack using 3D defocus information and fast direct inversion algorithms. This algorithm inverts the scattered signal in SPIR to recover the underlying sample from the measured data. The inverse problem is built upon our previously developed vectorial-optics physical forward model [Avci et al., 2016]. We formulate the SPIR signal in the dipole limit under the angular spectrum representation (ASR) framework in which the dyadic Green's functions are used. We then established a vectorial-optics-based linear forward model to relate the particle polarizability function to the intensity measurements. This model has also been demonstrated in spatial resolution enhancement for morphological visualization of viruses and dielectric structures using asymmetric illumination as described in Chapter 4. This study utilizes the forward model in defocus image reconstructions, where interferometric defocus images of the sample are captured under the circularly symmetric source function illumination. Our reconstruction framework is implemented by closed-form Tikhonov-regularized deconvolution using computationally and memory-efficient 2D fast Fourier transform (FFT) algorithms.

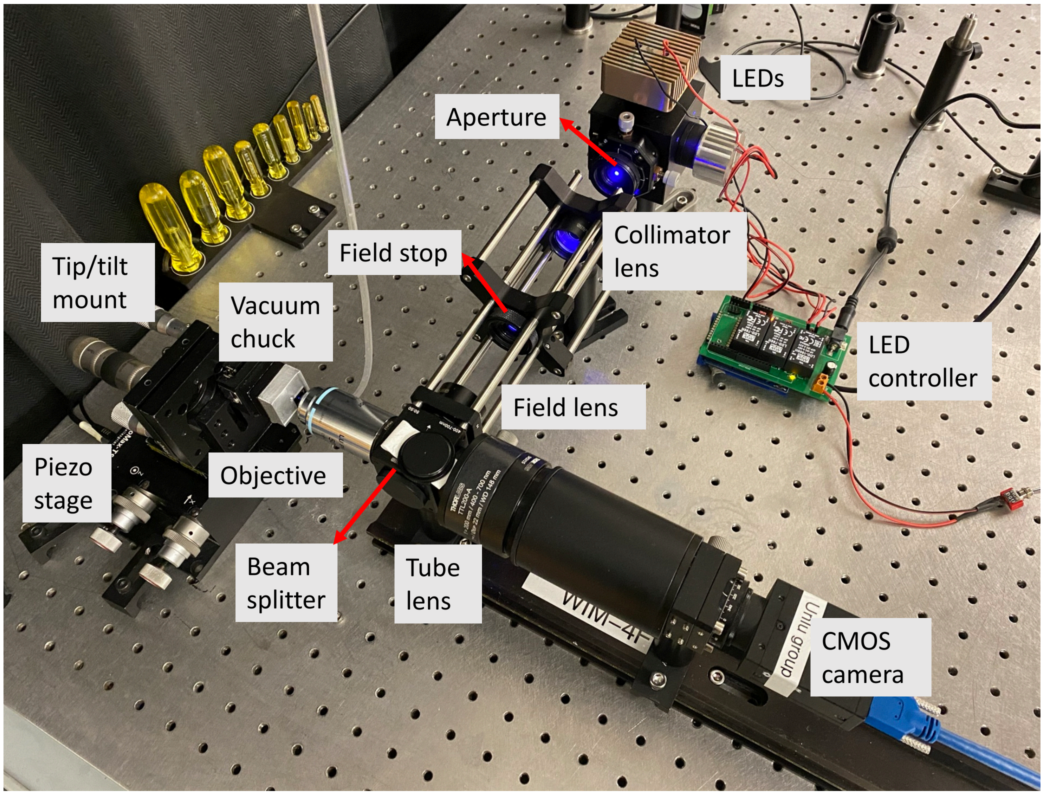
LEDs
Aperture
Collimator lens
Field stop
Tip/tilt mount
Vacuum chuck
LED controller
Field lens
Piezo stage
Objective
Beam splitter
Tube lens
CMOS camera
WiM-4F
Unlu group

Figure 3·1: Experimental setup of SPIR microscopy.

3.2 Experimental setup

Our setup is shown in Figure 3·1. A quasi-monochromatic blue (λ=457 nm center wavelength, $\Delta\lambda$=20 nm bandwidth) LED (LED Engin, LZ4-40B208-0000) is mounted on an integrating sphere (IS) (Thorlabs, IS200-4). The numerous scattering events to the illumination source inside the IS generate a highly uniform, nearly Lambertian output beam. An aperture diaphragm (Thorlabs, SM1D12C) is placed at the IS's exit port to control the illumination NA by employing Köhler illumination configuration where the aperture diaphragm and the objective back-pupil are conjugate planes. In this geometry, the aperture is projected to the back-focal plane of the microscope objective (Nikon, CFI TU Plan Fluor EPI 50×, NA 0.8) through a 4f-system consisting of two identical achromatic doublets (Thorlabs, AC254-060-A-ML). In the experiments, the aperture diaphragm size is set to 2.4 mm providing 0.3 NA sample illumination. This low NA illumination generates higher optical contrast from the sample as discussed in the previous Chapter 2. A second iris (field diaphragm) is placed in the conjugate plane of the sample to control the FOV and reduce the stray light coupled into the system. A custom-built sample holder is mounted on a 3-axis flexure stage with closed-loop piezo actuators (Thorlabs, MAX311D). An infinity-corrected tube lens (Thorlabs, TTL200) images the sample onto a monocolor 12.3 MP CMOS camera (FLIR, GS3-U3-123S6M-C) with 3.45 µm pixel pitch). The effective pixel size of 69 nm provides ∼5× sampling of diffraction-limited spots satisfying the Nyquist condition.

3.3 Interferometric defocus signal

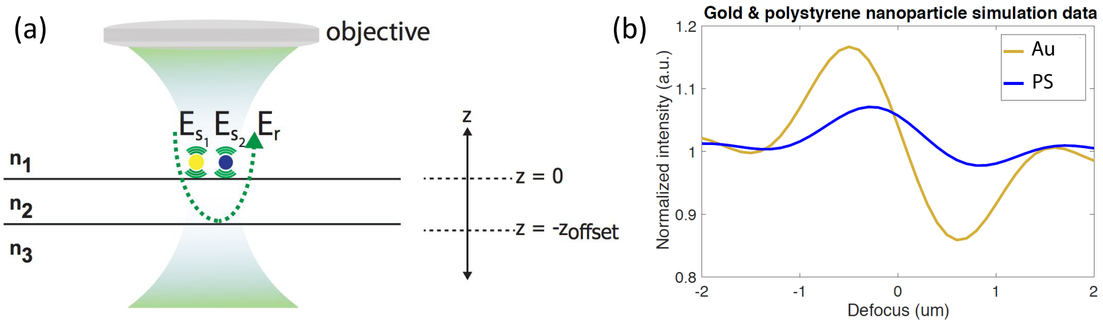

Figure 3·2: Defocus in SPIR microscopy. (a) Schematic of the setup illustrating the case when sensor surface is in the same plane as the focal plane of the objective ($z = 0$), the defocus takes place by moving this layered substrate in the axial direction (z), (b) simulated interferometric defocus curves for 60 nm gold and 65 nm polystyrene nanospheres

The theoretical considerations of SPIR have been described in Chapter 2. Briefly, SPIR utilizes a thin film of SiO_2 thermally grown on a Si substrate. The substrate with the optimized layer thickness enhances the sample's scattering field and provides a reference field for interferometric detection. SPIR's common-path configuration enables highly sensitive and stable interferometric imaging of nanoparticles captured on the substrate surface. The interference between reflected field $\mathbf{E_r}$ from the substrate surface and scattered field $\mathbf{E_s}$ is recorded as an intensity image by the camera. The resulting interference signal $I = |\mathbf{E_r} + \mathbf{E_s}|^2$ consists of three terms: (i) reflected intensity I_r, (ii) scattering intensity I_s, and (iii) interferometric cross-term $Re\{\mathbf{E_r}\mathbf{E_s}^*\}$. The contribution from the scattering intensity signal is negligible compared to the other terms due to the object's weak scattering nature. This comes from the fact that the scattering intensity drastically drops with the particle's volume square (r^6) dependency in the Rayleigh limit. Therefore, the coherent detection of scattering signal in SPIR enables sensing this minute signal above the strongly reflected field intensity. We define SPIR signal as background-normalized normalized $I^N = I/I_r$ and subtracted image contrast $I^S = (I - I_r)/I_r$. The simplified SPIR signal resulted from an individual plane wave m illumination can be expressed as follows:

$$I^s_m \approx A_0 |E_{r,m}(\mathbf{r})||E_{s,m}(\mathbf{r})| \cos_m(\theta(\mathbf{r})) \tag{3.1}$$

where A_0 is the scaling factor due to the normalization with reflected field intensity, m represents the individual plane waves within the range of the objective NA, and the sinusoidal term represents the phase difference between scattered and reflected fields as a function of distance $\mathbf{r}$. The phase term modulates the SPIR contrast from negative to positive as a function of the defocus position. The defocus position here is defined as the axial position difference between the objective focal plane and the substrate surface as shown in Figure 3·2(a) (adapted from [Avci et al., 2017b]). The amplitude and phase of the modulation function depend on the optical and physical properties of the sample [Avci et al., 2016]. Thus, the SPIR signal's coherent nature creates a unique signature as shown in Figure 3·2(b). This can be utilized to classify metallic and dielectric nanoparticles since metals have imaginary dielectric constants, inducing an additional phase shift in the defocus curves. In this study, we utilized the defocus PSF in all three dimensions. The calculated cross-sectional (XZ-plane) defocus SPIR image in Figure 3·3 shows the aforementioned axial dependence signal modulation behavior.

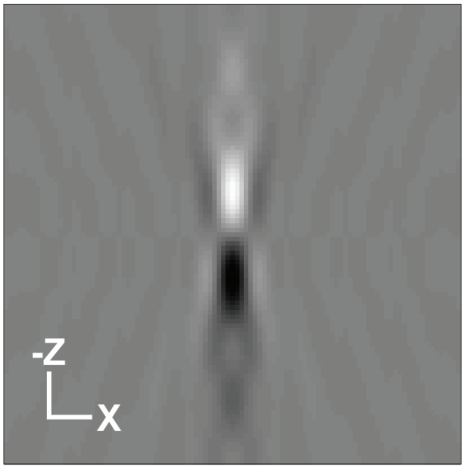

Figure 3·3: Simulated cross-sectional defocus image (XZ plane)

3.4 Linear forward model of SPIR

The individual plane waves coherently interact with the sample, but they are incoherent with each other due to the random phase relation. For a given incident field, the resulting enhanced scattered field components from the sample and specularly reflected field components from the substrate interfere at the image plane. The interference signal drastically improves the visibility of non-resonant sub-wavelength nanoparticles (often resulting in shot noise limited detection), as it realizes the linear detection of the scattering field, which scales with the particle polarizability and hence its volume (r^3 with r = particle radius). In contrast, the scattering intensity scales with the volume square (r^6) that leads to read-noise limited signal fall-off for sub-wavelength particles as in conventional dark-field detection schemes. The linear detection of the scattering field can also be utilized for establishing a computationally efficient linear inverse scattering problem. In this work, we formulated the vectorial linear forward model for the SPIR signal in the quasi-static limit where the dipole approximation is valid. We describe the physical model of the SPIR signal under the angular spectrum representation (ASR) framework using the dyadic Green's functions. The ASR framework depicts a more rigorous and accurate image formation in a high-resolution/NA optical imaging system compared with the scalar wave theory [Novotny and Hecht, 2006]. A complete picture of the SPIR signal with comprehensive theoretical foundations has been presented in recent studies [Sevenler et al., 2017, Avci et al., 2016]. Our forward model for SPIR builds upon these previous studies and can be extended to any arbitrary illumination function as we will discuss in the next chapter.

We present the refined closed-form solution of a dipole scatterer near a planar interface and realize the linear forward model for the SPIR signal. First, we define the total driving field of the dipole scatterer at the sample plane $\mathbf{E^o_{d,m}}(\mathbf{r})$, as the coherent sum of the incident plane wave $\mathbf{E^o_{i,m}}(\mathbf{r})$ and its reflected field from the substrate $\mathbf{E^o_{r,m}}(\mathbf{r})$. The resulting scattering field at the detector plane can be expressed as follows:

$$\mathbf{E_{s,m}}(\mathbf{r}) = \frac{k_0^2}{\epsilon_0}\overset{\leftrightarrow}{\mathbf{G}}_{\mathbf{s,m}}(\mathbf{r}) \otimes \mathbf{p_m} \tag{3.2}$$

$$\mathbf{p_m} = \epsilon_m \overset{\leftrightarrow}{\alpha} \mathbf{E^o_{d,m}}(\mathbf{r}) \tag{3.3}$$

where $\overset{\leftrightarrow}{\mathbf{G}}_{\mathbf{s,m}}$ denotes the sum of the primary and the reflected dyadic point spread functions (PSFs) which are calculated using the dyadic Green's functions in the far-field, $\mathbf{p_m}$ denotes the dipole moment induced by the driving field at the object plane, $\overset{\leftrightarrow}{\alpha}$ denotes the particle polarizability tensor, and k_o denotes the wavenumber in vacuum. The polarizability of a spherical dielectric nanoparticle in the dipole limit can be expressed as follows [Hulst and van de Hulst, 1981]:

$$\alpha_0 = 4\pi\epsilon_0 r_0^3 \frac{\epsilon_r - 1}{\epsilon_r + 2} \tag{3.4}$$

where r_o denotes the particle radius, ϵ_r denotes the ratio of the dielectric constants of the particle (ϵ_p) and the medium (ϵ_m), $\epsilon_r = \epsilon_p/\epsilon_m$. The reflected reference field at the object plane is mapped into the image plane,

$$\mathbf{E_{r,m}}(\mathbf{r}) = \mathbf{h_r}(\mathbf{r}) \otimes \mathbf{E^o_{r,m}}(\mathbf{r}) \tag{3.5}$$

where $\mathbf{h_r}$ is the collection PSF. Consequently, the total intensity at the image plane becomes the incoherent sum of the magnitude squared of the interfering reflected and scattered fields within the NA of the objective lens. The total detected intensity can be expressed as follows:

$$I_{det}(\mathbf{r}) = \sum_{\mathrm{m}\in\mathrm{NA}} \left[|\mathbf{E_{r,m}}(\mathbf{r})|^2 + |\mathbf{E_{s,m}}(\mathbf{r})|^2 + \mathbf{E^*_{r,m}}(\mathbf{r})\mathbf{E_{s,m}}(\mathbf{r}) + \mathbf{E_{r,m}}(\mathbf{r})\mathbf{E^*_{s,m}}(\mathbf{r}) \right] \tag{3.6}$$

As seen from equation 3.6, the physical model of the SPIR signal contains a quadratic term that is nonlinear requiring non-trivial reconstruction methods for recovering the object. To realize the simplified linear forward model in SPIR for sub-wavelength objects, we refined the problem under three physically motivated assumptions: (i) the particles of interest are weak scatterers, (ii) the light undergoes only a single scattering event with the object, and (iii) the particles of interest and the medium are composed of linear, homogeneous, and isotropic dielectric materials. The first term describing the reflected light intensity in equation 3.6 dominates the total measured intensity at the detector and acts as a background signal.

$$I_r(\mathbf{r}) = \sum_{\mathrm{m}\in\mathrm{NA}} |\mathbf{E_{r,m}}(\mathbf{r})|^2 \tag{3.7}$$

One can simplify equation 3.6 by subtracting the total reflected field intensity in equation 3.7 and normalizing the remaining signal with itself. Under the weakly-scattering object assumption due to the volume-dependent particle polarizability (see equation 3.4), the scattering field intensity (the second-term) becomes negligibly small compared with the interferometric signal (the cross-terms). The resulting signal is referred to the SPIR signal/contrast (signal-to-background ratio) described in equation 3.1 with the following form:

$$S(\mathbf{r}) = \frac{I(\mathbf{r}) - I_r(\mathbf{r})}{I_r(\mathbf{r})} \approx A_0 \sum_{\mathrm{m}\in\mathrm{NA}} \left[\mathbf{E}^*_{\mathbf{r,m}}(\mathbf{r})\mathbf{E}_{\mathbf{s,m}}(\mathbf{r}) + \mathbf{E}_{\mathbf{r,m}}(\mathbf{r})\mathbf{E}^*_{\mathbf{s,m}}(\mathbf{r})\right] \tag{3.8}$$

where A_0 denotes the scaling factor due to the reference field intensity and is usually $\sim$100 times smaller than the summation in equation 3.8. Note that the polarizability tensor $\overleftrightarrow{\alpha}$ in equation 3.3 is set to be a diagonal matrix under the assumption (iii) for the weakly-scattering BNPs and artificially synthesized nanostructures. Furthermore, in the dipole limit with the aforementioned approximations, light-matter interaction is linear and multiple scattering is negligible. The polarizability tensor $\overleftrightarrow{\alpha}$ in equation 3.3 can be set to be an identity tensor scaled with the polarizability (α_0) in a single direction, *i.e.*, $\overleftrightarrow{\alpha} = \alpha_0 \overleftrightarrow{I}$. As a result, by inserting equation 3.2 into equation 3.1, the effective PSF of the system becomes:

$$\begin{aligned}\mathbf{h}(\mathbf{r}) = \sum_{\mathrm{m}\in\mathrm{NA}} \Bigg[& \mathbf{C_0}\mathbf{E}^*_{\mathbf{r,m}}(\mathbf{r}) \left\{ \overleftrightarrow{\mathbf{G}}_{\mathbf{s,m}}(\mathbf{r}) \otimes \mathbf{E}_{\mathbf{r,m}}(\mathbf{r}) \right\} \\ & + \mathbf{C^*_0}\mathbf{E}_{\mathbf{r,m}}(\mathbf{r}) \left\{ \overleftrightarrow{\mathbf{G}^*}_{\mathbf{s,m}}(\mathbf{r}) \otimes \mathbf{E}^*_{\mathbf{r,m}}(\mathbf{r}) \right\} \Bigg]\end{aligned} \tag{3.9}$$

where C_0 is a complex constant due to mapping the total driving field $\mathbf{E^o_{d,m}}(\mathbf{r})$ into the detector plane. Since the ASR framework provides control over individual plane waves illuminating the sample, the theoretical formulation provides an easy implementation for both inverse problem and PSF engineering through the source plane.

3.5 PSF calculations

The physical forward model of SPIR was developed on custom-built MATLAB software using ASR formulation in the dipole limit where the size of the nanoparticle is much shorter than the excitation wavelength [Avci et al., 2016]. The model calculates the SPIR image of a dipole scatterer placed near a planar surface using the vectorial formulation discussed in the results section. We used the polarizability tensor of a silica nanosphere because silica has dielectric characteristics, that is, nonresonant and low-index, similar to biological nanoparticles. In the model, a spatially incoherent light source with a uniform intensity profile is imaged into the back focal plane of the microscope objective in Köhler geometry. Each point in the back-pupil is assumed to have the same intensity. Thus, the sample is uniformly illuminated within the angular spectrum of the system that is limited by the objective NA in epi-illumination. This is a valid assumption owing to the integration sphere which eliminates any structural attributes of the light source by reflecting each ray multiple times. The corresponding PSFs were calculated for a defined illumination geometry and system parameters at a given defocus position. Overall 41 defocus PSFs are generated for a 4 µm defocus range with 100 nm step size.

3.6 Experimental validation of simulations

To experimentally validate the physical forward model, we first demonstrate defocus profiles using 100 nm silica beads (nanocomposix, SISN100-25M). Silica ($n \approx 1.47$) beads have similar dielectric and optical properties to biological nanoparticles and are great model nanoparticles for SPIR's performance characterization. The defocus profile of averaged ∼1462 silica beads captured in a single FOV has been shown by the red curve in Figure 3·4(a). The defocus images in all experiments are acquired over a 4 µm range with an empirically determined step size of 100 nm. The minimum

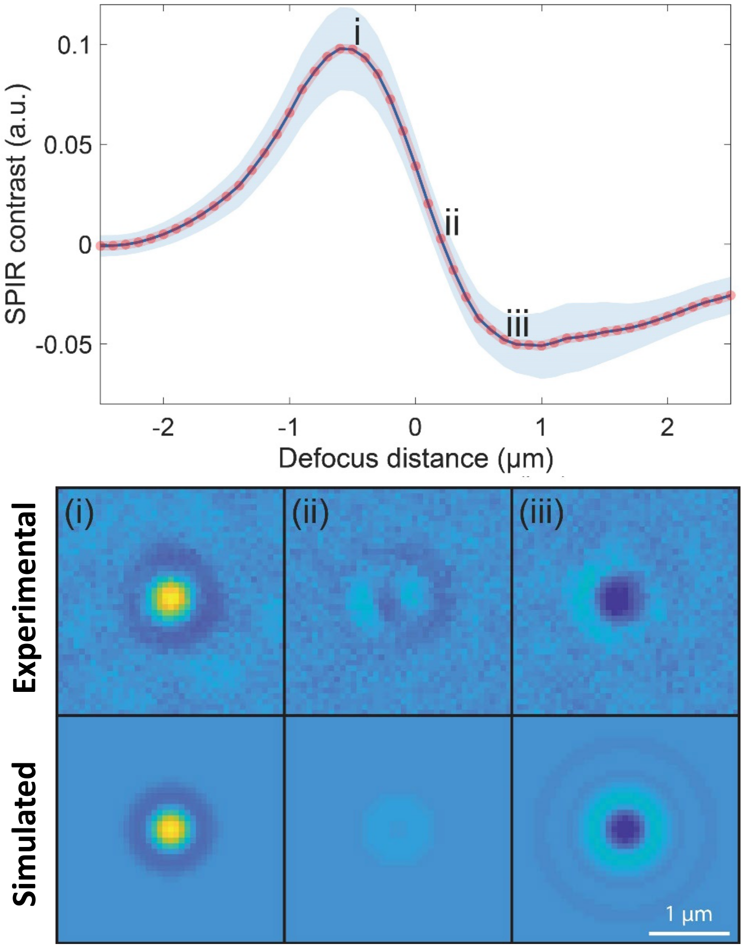

Figure 3·4: (a) Defocus profiles of silica beads with the 100 nm nominal diameter. The red curve indicates the mean SPIR contrast of ∼1462 beads detected across the full FOV. The shaded curve indicates the standard deviation of the measured SPIR contrasts (b-d) (Top) The normalized and background-subtracted experimental SPIR images and (bottom) the calculated PSFs at the defocus positions (i-iii) from left to right, respectively. Scale bar is 1 µm.

defocus range (∼2 µm) required to capture peaks and dips is proportional to the depth of field ($\propto 1/NA^2$). The SPIR contrast variation across the beads stems from the dispersity in the beads' dimensions. They are nominally spherical but can exhibit eccentric (prolate/oblate) spheroid geometry. Furthermore, we verify the forward model using the same beads. Although 100 nm beads have ∼10% SPIR contrast which is 10 times more than the typical shot-noise detection limit of ∼1% at a single acquisition, they provide high SNR fringe contrast for better PSF evaluation. As demonstrated in Figure 3·4(b), the calculated PSFs show great consistency with the experimental data.

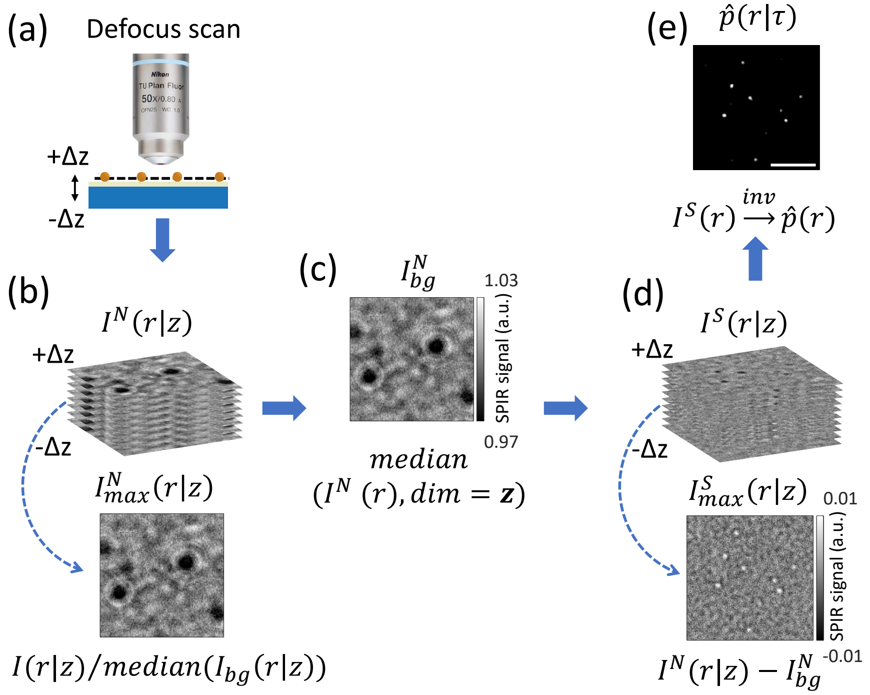
(a)
Defocus scan
Nikon
TU Plan Fluor
50x/0.80
$+\Delta z$
$-\Delta z$
(b)
$I^N(r|z)$
$+\Delta z$
$-\Delta z$
$I^N_{max}(r|z)$
$I(r|z)/median(I_{bg}(r|z))$
(c)
I^N_{bg}
1.03
SPIR signal (a.u.)
0.97
$median$
$(I^N\ (r), dim = \boldsymbol{z})$
(d)
$I^S(r|z)$
$+\Delta z$
$-\Delta z$
$I^S_{max}(r|z)$
0.01
SPIR signal (a.u.)
-0.01
$I^N(r|z) - I^N_{bg}$
(e)
$\hat{p}(r|\tau)$
$I^S(r) \xrightarrow{inv} \hat{p}(r)$

Figure 3·5: Flow chart of computational nanosensing using defocus curves in SPIR. (a) Schematic of defocus scan. The defocus images are acquired by translating the sample along the optical (z) axis using the piezo scanner. (b) (Top) Defocus stack images normalized with background $I^N(r|z)$ and (bottom) the max-contrast image from the normalized stack. (c) Background image I^N_{bg} is obtained by median filtering along the defocus dimension. (d) (Top) Background subtracted SPIR signal $I^S(r|z)$ defocus stack and (bottom) max-contrast image from the stack. (e) Reconstructed single image. Scale bars are 2 µm.

3.7 Reconstruction from defocus

The reconstruction framework is formulated to estimate the nanoparticle's polarizability distribution by minimizing the least-squares of the difference between the measured SPIR contrast and the expected signal obtained from the linear forward model which can be expressed as follows:

$$y_l = A_l x + n_l \tag{3.10}$$

y_l denotes the observed image, A_l denotes the convolution operator associated with the linear shift invariant PSF at a defocus position of subscript l, x denotes the unknown underlying structure to be reconstructed, and n_l denotes the unknown noise. Since the generalized solution suffers from noise amplifications in the ill-conditioned problems [Ralston et al., 2006], we employ the penalized least-squares to obtain a more stable estimation from noisy SPIR measurements. The underlying object can be estimated by minimizing the penalized least-squares cost function associated to Tikhonov regularization. This least-squares problem in Fourier domain can be written as:

$$\min \sum_{l=1}^{N} \left| \tilde{H}_l \tilde{P} - \tilde{I}_l^S \right|^2 + \tau |\tilde{P}|^2 \tag{3.11}$$

where $\tilde{P}$ is Fourier transform of the polarizability distribution function $p(r)$, $\tilde{H}_l$ and $\tilde{I}_l^{\,S}$, respectively, are the calculated PSF and the normalized, background-subtracted SPIR images in Fourier space at a particular defocus position l, and τ is the regularization parameter. The regularization parameter τ is manually adjusted over a range of values to achieve better noise-suppressing while preserving physical structure of the sample. The solution for the Eq. 3.11 in the spatial frequency domain can be expressed in closed-form,

$$\hat{p}(r|\tau) = \mathcal{F}^{-1} \left\{ \frac{\sum_{l=1}^{N} \tilde{H}_l^* \tilde{I}_l^S}{\sum_{l=1}^{N} |\tilde{H}_l|^2 + \tau} \right\} \tag{3.12}$$

where $\mathcal{F}^{-1}\{\cdot\}$ denotes inverse Fourier transform. The solution of Eq. 3.12 has an explicit inversion that can be easily implemented in computers using computationally simple and memory-efficient fast algorithms [McLeod and Ozcan, 2016].

To implement the reconstruction algorithms, we pre-process the raw defocus image stack and obtain the normalized, background-subtracted intensity images (SPIR contrast) defined in the forward model. The reconstruction flow-chart using 50 nm silica beads (nanocomposix, SISN100-25M) is demonstrated in Figure 3·5. First, we normalize defocus images with their corresponding background intensity to account for the intensity fluctuations during the acquisition. Heterogeneous background artifacts such as black/white spots due to the dust and surface roughness on the substrate, optical sensor, and collection optics are then removed from the image. These artifacts significantly limit the system performance because they typically have 2-3% contrast that is comparable to the sample's SPIR contrast (e.g., 1-2% for 50 nm silica beads). Fortunately, these unwanted artifacts are relatively stationary within the defocus range such that median filtering along the axial dimension can be performed to obtain the background signal. We note that the colorbar limit in the processed image in Figure 3·5(d) is adjusted to achieve better visualization. The pre-processed images are then fed into the Tikhonov regularized inversion algorithm in equation 3.12 to reconstruct the nanoparticle sample.

3.8 Proof-of-concept experiments

Figure 3·6 demonstrates the reconstruction results of ∼1275 silica beads with 50 nm diameter across a large FOV of 180 µm × 260 µm. To highlight background artifact suppression, we compare the normalized intensity signal with the calculated background intensity and SPIR signal as shown in Figure 3·6(b-d). The cross-section profiles of those images (see Figure 3·6(f)) show the median filtered background estimation clearly reveals the particle signal originally hindered in the raw images. Moreover, it eliminates false identification of the artifacts that appear as diffraction-limited spots (the dashed circles in Figure 3·6(c)). The substrate consists of L shape reference patterns which are etched down to the silicon substrate. These reference regions facilitate the focus alignment. Also, Laplacian of Gaussian is implemented to automatically determine the nominal focus position before the reconstruction. We observe at least two-fold SNR improvement in the reconstructed images as shown in Figure 3·6(g). Most strikingly, the reconstruction renders a high-SNR (improved to > 4) signal from the undetectable low-SNR (< 1) SPIR signal in raw images. The histogram indicates that these beads exhibit polydispersity in their size. Overall, the regularized reconstruction suppresses the noise artifacts and improves image quality. We note here that more complex regularization operators in tandem with image processing algorithms could achieve better SNR performance at the cost of the algorithm's computational complexity.

The interferometric detection of the scattering signal with a strong reference field in SPIR allows for operating the camera at very close to the pixels' full-well capacity. Therefore, SPIR sensitivity in a single frame is limited by the photon shot-noise associated with the reflected field intensity. Since the SPIR signal scales linearly with the particle volume (r^3), we anticipate that SPIR can detect silica nanoparticles as small as 25 nm in diameter with the current settings. We note that the SPIR's sensitivity limit could be further improved by frame averaging and large well-depth cameras as discussed in Chapter 2. Moreover, our polarizability reconstruction approach could provide great sensitivity improvement for metallic nanoparticles which exhibit distinctive defocus profiles compared with the dielectric background signal. This comes from the fact that the complex refractive index in metals induces an additional phase change in the scattered field. Although our technique is only demonstrated using dielectric silica nanoparticles, the forward model can be extended to metal nanoparticles for digital microarray applications in SPIR [Sevenler et al., 2018].

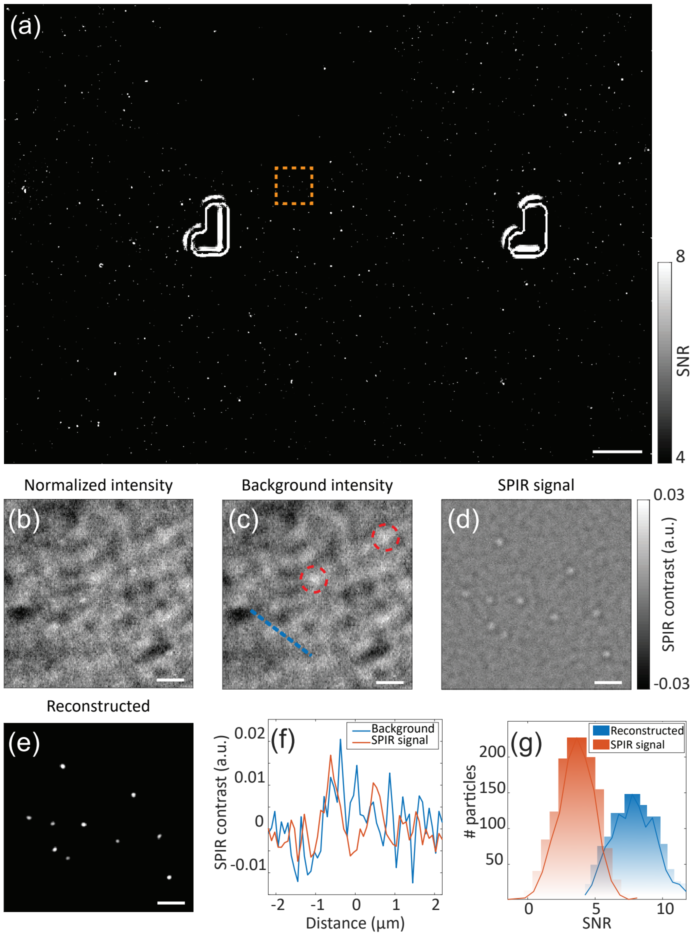

Figure 3·6: (a)Reconstructed image of silica beads with a 50 nm nominal diameter. In total, ∼1275 silica beads are detected across the full FOV after filtering out of range particle contrasts. Insets (b-e) are the zoom-in regions indicated by the dashed square in (a). (b) The normalized intensity image at defocus position of maximum contrast, (c) the background image calculated from the defocus image stack, (d) the background-subtracted normalized SPIR image calculated from (b) and (c), and (e) reconstructed image inset indicated in (a). (f) The cross-section profiles along the dashed line in (c). (g) The SNR histogram of silica beads (N = ∼1275) detected in reconstructed image (a) and normalized, the background-subtracted image at the maximum-contrast defocus plane. Scale bars in (a) and (b-e) are 20 µm and 2 µm, respectively.

3.9 Conclusion

In summary, we developed a new image reconstruction framework by solving the inverse scattering problem in SPIR microscopy. This framework successfully estimates the background signal and reconstructs a single high-SNR image from an intensity-only defocus image stack. Our computational imaging method provides means for enhanced sensitivity performance and image quality that extends SPIR's capability of sensing to much smaller dielectric nanoparticles. The linear physical model of the SPIR signal allows for computationally efficient inversion owing to the direct division in the Fourier domain. Moreover, our method can compensate for the low SNR particle signal in the individual images of the 3D stack that otherwise can be lost in raw images. Although we only demonstrated this approach in dry samples, this framework can be readily applied to dynamic in-liquid common-path interferometric imaging configurations in which antibody captured nanoparticles exhibit mobility less than a few nanometers owing to the strong multivalent interactions [Scherr et al., 2016]. We expect this new computational imaging approach in SPIR microscopy to advance the accuracy and sensitivity for the detection and characterization of biological nanoparticles in a high-throughput manner.

Chapter 4

High-resolution interferometic microscopy by computational asymmetric illumination

4.1 Introduction

Label-free optical microscopy in the visible spectrum has been an indispensable tool for studying biological nanoparticles (BNPs). In the previous chapters, we discussed great sensitivity achieved by wide-field interferometric imaging techniques that have demonstrated the label-free detection of very small BNPs such as exosomes [Daaboul et al., 2016], viruses [Daaboul et al., 2010], and synthetic nanoparticles [Avci et al., 2017a]. Recent advancements in interferometric microscopy techniques improved system sensitivity with pupil engineering and led to single protein detection in sparse samples, yet they do not address the inadequate lateral resolution [Young et al., 2018, Cheng et al., 2019, Avci et al., 2017a]. This stems from the fact that these techniques rely on sample illumination at a normal incidence angle to achieve enhanced nanoparticle visibility. Therefore, the diffraction-limited bandwidth is typically limited to λ/NA in such coherent detection systems, where λ is the illumination wavelength and NA is the objective numerical aperture. The high-frequency sample information can be accessed via oblique illumination in the coherent imaging systems [Haeberlé et al., 2010].

In this study, we introduce a computational imaging approach that extends single-particle interferometric reflectance (SPIR) microscopy's capability from direct detection to detailed morphological characterization of sub-diffraction-limited particles. Recently, several computational coherent imaging techniques have demonstrated great advancements in improving spatial resolution [Ralston et al., 2007, Soto et al., 2018, Zhou et al., 2019, Zheng et al., 2013, Tian et al., 2014, Cotte et al., 2013, Tian and Waller, 2015]. In particular, our work draws inspirations from Fourier ptychographic microscopy (FPM) [Zheng et al., 2013, Tian et al., 2014] and differential phase contrast (DPC) [Tian and Waller, 2015]. In both FPM and DPC, the sample is illuminated from multiple incidence angles to encode the high-frequency information about the sample into the finite passband of the imaging system. Next, a phase retrieval algorithm is applied to quantitatively recover the object with improved spatial resolution from the captured low-resolution intensity images. In FPM, the sample is modeled with a complex transmittance function that is nonlinearly related to the intensity. In DPC, the forward model is simplified to be linear by directly relating the weak permittivity contrast of the object to the captured intensity. In both cases, a scalar diffraction theory is used to model the object-light interaction.

In contrast to FPM and DPC, SPIR microscopy utilizes interferometric enhancement to detect the scattered light from sub-wavelength particles in which light-matter interaction has a strong dependency on polarization. Therefore, we formulated the SPIR signal in the dipole limit using vectorial Green's functions and then established a vectorial-optics-based linear forward model to relate the particle polarizability function to the intensity measurements. Similar to FPM and DPC, we applied both asymmetric illumination and efficient computational algorithms to improve the lateral resolution of SPIR microscopy. For the sake of brevity, we referred to this particular refinement over conventional SPIR microscopy as "computational asymmetric illumination SPIR", or caSPIR. Our method performed a computational reconstruction of a single high-resolution image from a series of low-resolution intensity images captured under asymmetric illumination using an illumination (source) function design engineered for achieving maximum contrast and resolution. We performed this reconstruction by solving a least-squares problem of the inverse scattering physical model with Tikhonov regularization. To demonstrate the versatility of our system, we quantified the shape and size of several types of low-refractive-index nano-objects. We first validated the caSPIR technique on a nanofabricated artificial sample which consists of nano-bars/words imprinted on a SiO_2 layered substrate using the electron beam lithography (EBL) process. We then demonstrated high-resolution, wide-field imaging of mixed-morphology of Ebola virus-like particles and a more uniformly structured Ebola virus vaccine candidate to show bio-related applications of this method.

4.2 Experimental design of caSPIR

The experimental setup for caSPIR is illustrated in Figure 4·1a. The photo of the real setup is shown in Chapter 2 Figure 2·8. A high-power LED with a spectral half-width of ∼14 nm at 420 nm central wavelength (Lumileds) is butt-coupled to an integrating sphere (Thorlabs). The coupled light undergoes multiple diffusive reflections on the entire sphere surface. Thus, the integrating sphere provides highly uniform, source-free, and spatially incoherent illumination. Note that the effect of integrating sphere on temporal coherence is quite negligible because it is reflectance spectrum is almost flat in a broad wavelength range (250 - 2500 nm). The custom-made 3D printed circular sector aperture shown in Figure 4·2 is mounted on a manual rotation mount (Thorlabs). The aperture is imaged into the back focal plane of the microscope objective (Nikon, 100×/0.9 NA) in Köhler geometry with unit magnification. Under the conventional SPIR configuration, a graduated ring actuated iris diaphragm mounted on a cage plate is mounted to control the illumination NA. The layered substrate under observation is placed on a custom-built vacuum chuck is mounted on a closed-loop

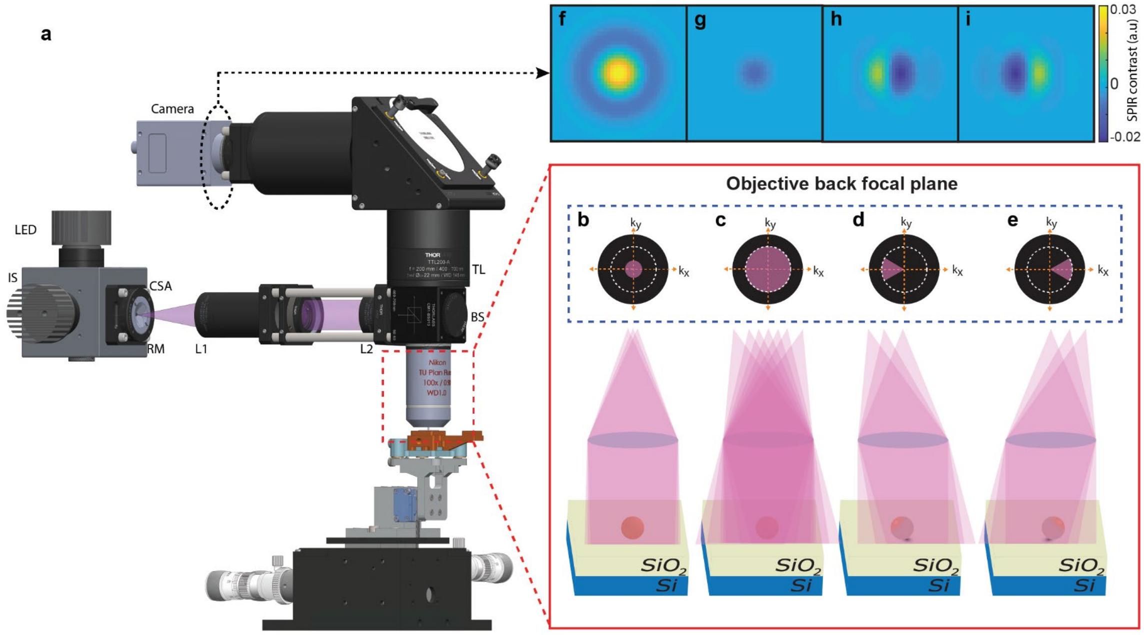

Figure 4·1: Single Particle Interferometric Reflectance (SPIR) microscopy. (a) Schematic of the experimental setup. IS, integrating sphere; CSA, circular sector aperture; RM, rotation mount; L1-L2, lenses; BS, 50:50 beam splitter; TL, tube lens. (b) Low-NA and (c) full-NA illumination schemes in conventional SPIR. (d,e), asymmetric illumination schemes in caSPIR with different rotation angles, 0° and 180° respectively (white dashed line denotes the boundary–back pupil size–of spatial frequencies limited by objective NA). (f-i) Calculated PSFs correspond to illumination schemes in (b-d), respectively. PSFs are calculated for 100×/0.9 NA objective in air at 420 nm illumination wavelength. The illumination NAs are set 0.3 and 0.9 in (f,g), respectively.

piezo-z stage (Micronix). A tube lens (Thorlabs) images the sample onto a monocolor 12 MP charge-coupled device (CCD) camera (Pointgrey) which has 3.1 µm pixel pitch providing more than twice the sampling rate required for Nyquist criterion – ∼ 6.2 µm for 125 nm resolution–.

In principle, each point in the light source generates a plane wave that illuminates the sample at an incident angle defined by its position in the transverse plane (see Figure 4·1b-i). A point source further away from the optical axis illuminates the

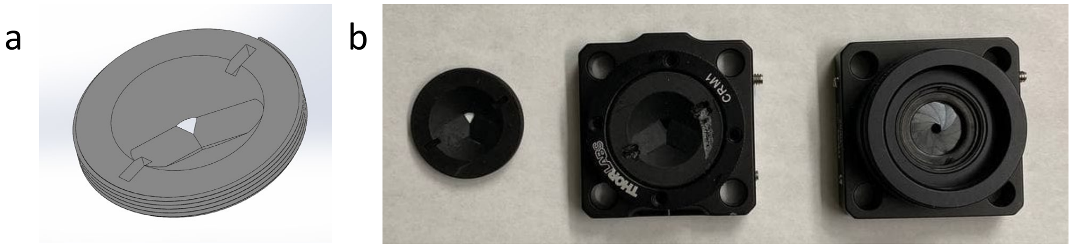

Figure 4·2: Circular sector aperture. (a) 3D CAD illustration of 60° circular sector mask. (b) Left to right: 3D printed sector mask, rotation mount, and circular iris aperture for low-NA illumination.

sample with the larger incident angle. Thus, the filling factor of the objective pupil in the classical sense (circular filling) relates the maximum oblique incident angle on the sample with the illumination numerical aperture (NA). Moreover, as depicted in Figure 4·1a, the LEDs are butt-coupled to an integrating sphere. The coupled light reflects multiple times (> 100) from a highly reflective surface and travels orders of magnitude longer than the coherence length of the LED before exiting the integrating sphere. This source scrambling provides uniform, source-free, and spatially incoherent illumination on the sample satisfying our model's assumptions.

4.3 Forward model of caSPIR

As discussed earlier, interferometric detection in SPIR microscopy realizes linear detection of the scattered field for nanoscale objects. The forward model for SPIR signal has been presented in Chapter 3, where we formulated the forward model for defocus image reconstructions. The linear forward model for the SPIR signal in the dipole limit where particles of interest are much smaller than the illumination wavelength is analytically discussed. This model relates a particle polarizability function with the measured intensity images. A complete picture of the SPIR signal with comprehensive theoretical foundations has been presented in recent studies [Avci et al., 2017a, Sevenler et al., 2017, Avci et al., 2016] which are summarized in the previous chapters. The computational nanosensing study is limited to low-NA illumination where a circularly symmetric illumination function is used. In this caSPIR study, we built our forward model on the previously formulated model and extend it to partially coherent asymmetric illumination for the caSPIR implementation. The PSFs were numerically calculated in custom-built MATLAB software described in Chapter 3 considering the illumination function and system parameters. Note that the EBL sample has an 80 nm oxide layer in contrast to the other samples that are immobilized on 60 nm oxide chips. Thus, two sets of PSFs were simulated to be used in reconstructions in this study.

4.4 Illumination function optimization

In our earlier studies, we utilized pupil function engineering and demonstrated a significant contrast enhancement by imposing the low-NA (0.3 NA) illumination constraint which limits the angle of incidence's upper bound [Avci et al., 2017a]. The theoretical explanation for the contrast enhancement by low-NA illumination was rigorously reported in [Avci et al., 2017a]. The illumination NA effect on the image contrast in Köhler geometry is also experimentally studied in reflected interferometric microscopy using a glass substrate [Mahamdeh et al., 2018]. The low-NA illumination is obtained by underfilling the objective pupil using an asymmetric circular source function. We refer to the SPIR microscopy with a low-NA implementation as conventional SPIR in which the emphasis has been on achieving high-contrast nanosized object detection [Sevenler et al., 2017]. However, the contrast improvement comes at the expense of a reduction in spatial resolution.

The trade-off between spatial resolution and SPIR contrast is an important limitation for high-resolution visualization of sub-diffraction-limited nanoparticles, particularly under the classical (circular) illumination schemes. With Köhler illumination,

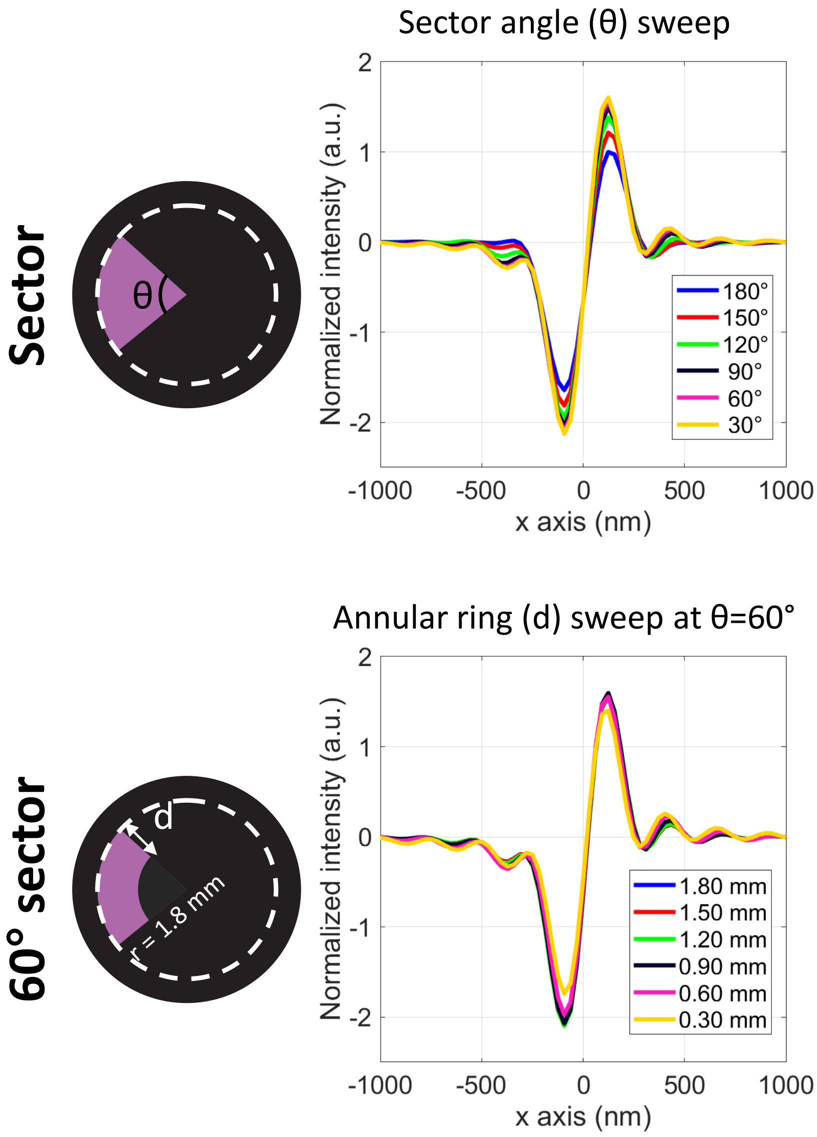

Figure 4·3: Circular sector optimization. (Top) Circular sector illustration and cross-section profiles along the center line for circular sector angles ranging from 30° to 180°. (Bottom) Annular aperture illustration at sector angle 60° and cross-section profiles along center line for blocked NAs ranging from 0 to 0.75 NA. Normalized intensity values are scaled with arbitrary unit.

the source function is imaged onto the objective pupil, and its radius directly determines the illumination NA and hence the maximum oblique angle incident on the sample. Oblique illumination at large incident angles is critical for encoding the high-resolution sample information into the imaging system's finite bandwidth. For this reason, the low-NA illumination (Figure 4·1b,f) provides an overall fivefold contrast improvement over full-NA illumination (Figure 4·1c,g), but incurs lower quality spatial resolution (∼320 nm at 420 nm wavelength). Since the maximum attainable oblique angle under epi-illumination configurations is limited by the objective NA, the sample under a full-NA illumination is illuminated at incident angles spanning the full range of the objective NA. Thus, utilizing the entire objective pupil becomes crucial for high-resolution imaging. To alleviate the loss of contrast with improved resolution, multiple images obtained by asymmetric illumination can provide full-NA equivalent resolution of SPIR while retaining the improved contrast sensitivity of a low-NA configuration.

Two main benefits of the asymmetric illumination for the SPIR microscopy were demonstrated in this work: (i) SPIR contrast is significantly enhanced (threefold) compared with full-NA illumination in which BNPs of interest are often indistinguishable from the background. (ii) The high-resolution information from the sample becomes accessible due to the oblique illumination at larger incident angles, unlike in the conventional SPIR. In the implementation, we employed the asymmetric illumination using a circular sector aperture in the conjugate plane of the back-pupil (see Figure 4·1d,e). The circular sector's radius matches the pupil size to access the entire objective back-pupil. With this configuration, the system can generate plane waves with incident angles within the objective NA's full range. The circular aperture partially covers the objective's angular spectrum, so that, only plane waves with particular azimuthal angles illuminates the sample. Thus, the aperture creates an asymmetric illumination pattern that has a limited azimuthal content defined by the sector angle. This angular asymmetry in the illumination leads to asymmetric PSF compared with the PSFs corresponds to the classical illumination patterns as shown in Figure 4·1g-h.

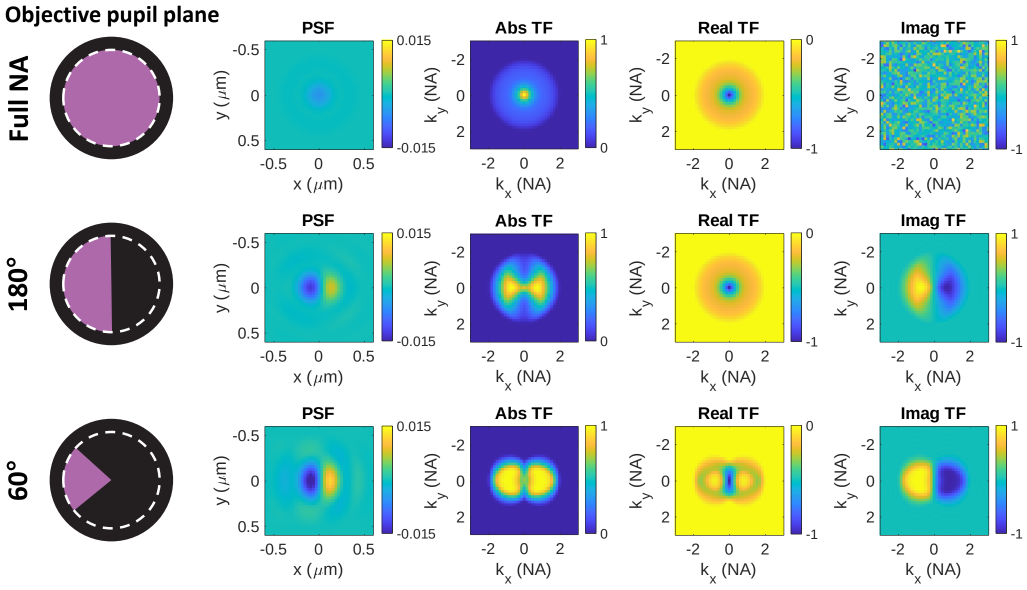

Figure 4·4: Circular sector PSF optimization. Source-function illustrations and their corresponding PSFs and TFs.

We optimized the asymmetric illumination function to jointly achieve maximum contrast and resolution in SPIR. We theoretically calculated the SPIR contrasts for different circular sector angles ranging from 30° to 180°. The SPIR contrast improves with decreasing the sector angle and reaches a plateau at the smaller angles as shown in Figure 4·3. This theoretical observation stems from the fact that the system PSF is the incoherent superposition of PSFs corresponds to the individual plane waves emanating from each point at the back-pupil (see equation 3.9). The summation of the PSFs along the different asymmetric axes averages out the asymmetry more at the large sector angles and thus decreases the contrast. Likewise, the circular source-function centered at the back-pupil generates circularly symmetric PSF because points symmetric about the origin cancel out the asymmetry. Since the exposure time required for shot-noise-limited detection is linearly proportional to the sector angle, employing the smallest sector angle is not practical for operating at the shot-noise limit. Also, the percentage change in the SPIR contrast from 30° and 60° is quite negligible, less than 1.3%. Accordingly, we determined the circular sector angle as 60° to achieve a higher contrast relative to a semicircular aperture with shot-noise-limited exposure time. Note that we expected to achieve similar performance with a 90° sector angle. We further investigated the effect of the annular aperture on the SPIR contrast. It is clearly seen that the annular aperture decreases the SPIR contrast. Therefore, we determined the asymmetric illumination aperture to be a circular sector.

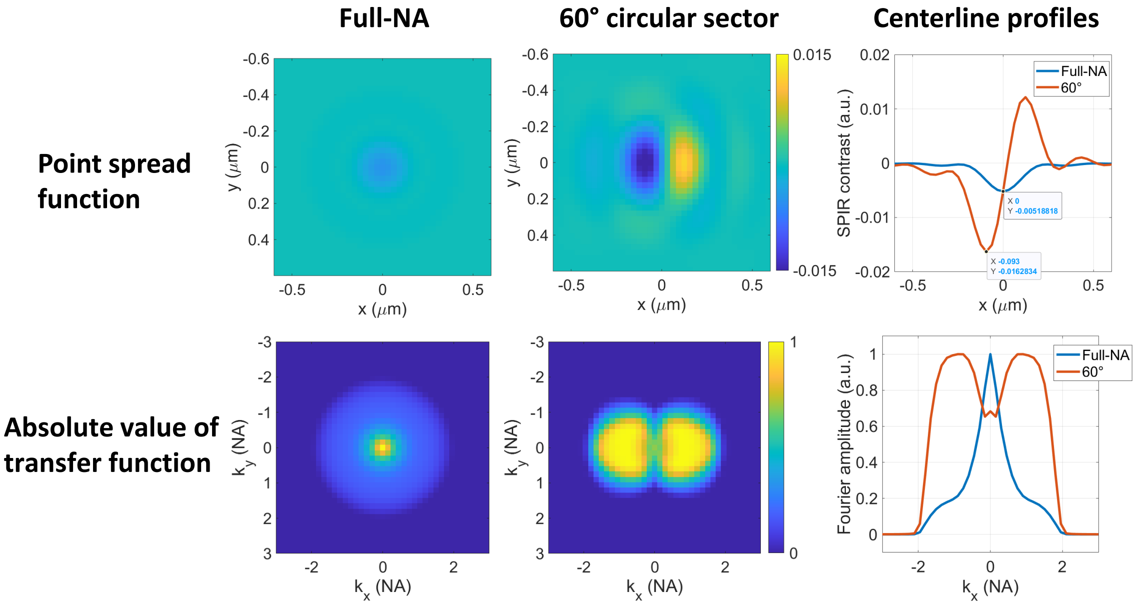

Figure 4·5: Contrast and frequecny support comparison of full-NA and asymetric illumination functions.

We further investigate the PSFs in the Fourier domain to analyze frequency support in circular sector illumination. Figure 4·4 compares full-NA, 180° and 60° PSFs, TFs, and their imaginary and real parts. The full-NA illumination does not provide any phase information due to symmetry of illumination, whereas DPC illumination's transfer function is asymmetric and non-negative. Moreover, the real part of the 60° TF is asymmetric compared to the 180° TF. Hence, the overall frequency coverage is much more improved in smaller circular sector angles. We also compared the cross-sections of PSFs and TF magnitudes in Figure 4·5. It is clearly shown that the high-frequency support increases in small angles. One drawback of asymmetric illumination is the loss of Fourier coverage along the axis of asymmetry. To recover these missing frequencies and access the imaging system's entire bandwidth, we obtained multiple images of the same FOV along different asymmetric axes by rotating the circular sector. Moreover, this combination of multiple images under various asymmetric illumination doubles the effective numerical aperture of our technique [Tian and Waller, 2015]. Although asymmetric illumination does not break the diffraction limit, an increase in the bandwidth support of the associated PSF indeed provides 2× lateral resolution improvement. To acquire multiple image pairs in practice, we manually rotate the 3D printed circular sector mask on the rotation mount shown in Figure 4·2. We further emphasize that oxide thickness is also critical to achieving high-contrast asymmetrically illuminated SPIR imaging. Figure 4·6 compares the PSFs centerlines at different oxide thicknesses. The oxide thickness changes the contrast and the profile significantly. 60 nm oxide can achieve high-contrast for both negative and positive peak values along the illumination axis.

4.5 Object reconstruction

We follow a reconstruction framework discussed in Chapter 3. Briefly, the linear forward model, $y_j = A_j x + n_j$, was established using the vectorial SPIR model. y_j denotes the observed image, A_j denotes the convolution operator associated with the shift invariant PSF for a particular asymmetric illumination geometry of subscript j, x denotes the unknown underlying structure to be reconstructed, and n_j denotes the unknown noise. The underlying object can be estimated by minimizing the penalized least-squares cost function associated to Tikhonov regularization as follows:

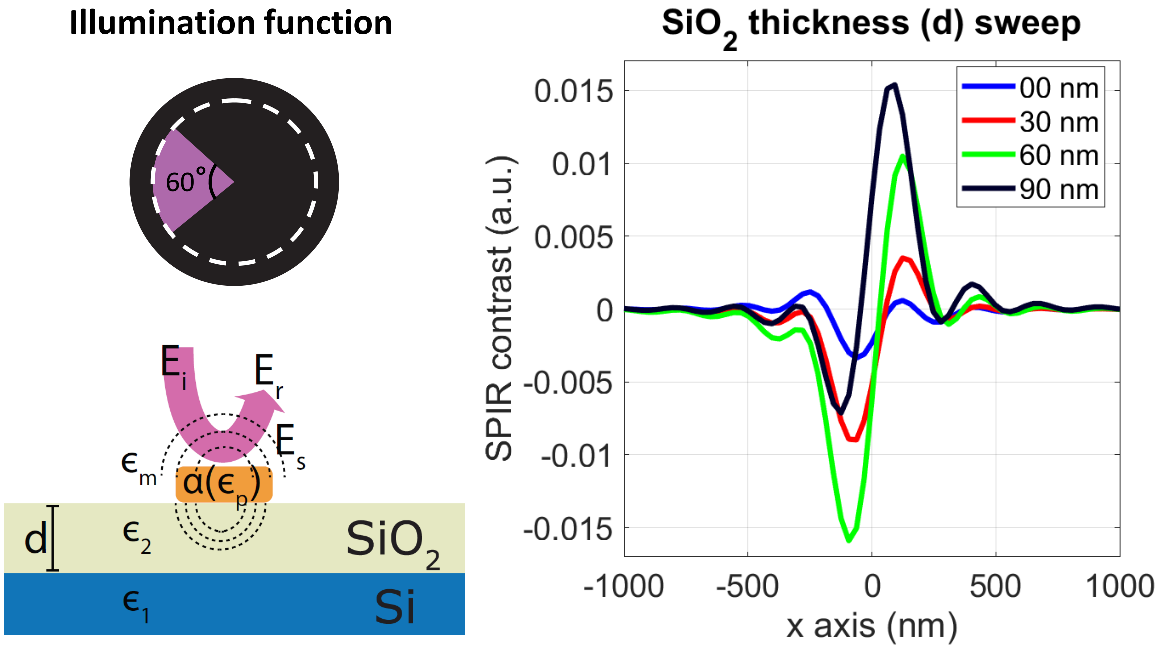

Figure 4·6: Oxide thickness effect on the SPIR contrast under 60° asymmetric illumination.

$$\hat{x}(\alpha) = \arg\min_{x} \sum_{j=1}^{N} \Big[\parallel A_j x - y_j \parallel_2^2 \Big] + \alpha \parallel x \parallel_2^2 . \tag{4.1}$$

Note that the first term in this optimization accounts for the data fidelity, and the second term captures prior information regarding image behavior, with α being a regularization parameter which trades off impact of the two terms. The closed-form solution of the Tikhonov regularized least-squares minimization problem can be expressed as:

$$\hat{x}(\alpha) = \mathcal{F}^{-1} \left\{ \frac{\sum_{j=1}^{N} [H_j^{*}(Y_j)]}{\sum_{j=1}^{N} |H_j|^2 + \alpha} \right\}. \tag{4.2}$$

where $\mathcal{F}^{-1}\{\cdot\}$ denotes the inverse Fourier operator, and H and Y denote the Fourier transforms of A and y, respectively. The raw images for asymmetric illumination were acquired by manually rotating the 60° circular sector aperture by 30° steps, results in 12 total images. After the asymmetrical illuminated images were acquired, the circular sector was replaced with a graduated-ring diaphragm to acquire conventional SPIR images. The conventional images were taken under low-NA (0.3) illumination. Then, the images were reconstructed in MATLAB using the aforementioned closed-form solution. The regularization parameter α was empirically chosen by visual inspection to provide the best discrimination of the objects in the scene. All the images were taken under the 100×/0.9 NA objective unless otherwise stated.

4.6 Experimental validation of caSPIR

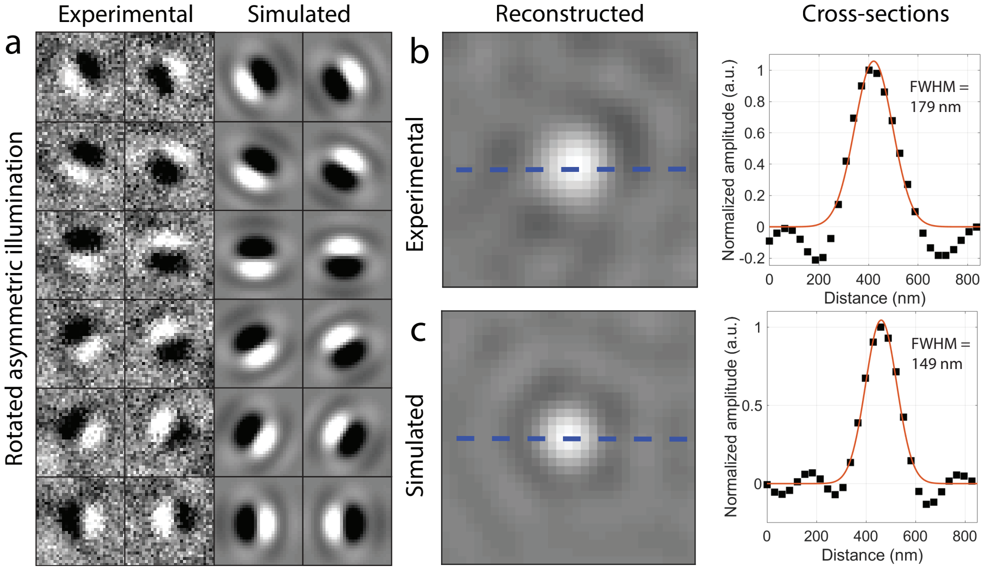

Figure 4·7: Experimental validation of caSPIR. (a) Experimental (left two rows) images of 100 nm PS bead and theoretically (right two rows) calculated PSFs corresponds to circular sector mask's angle of axis of the asymmetry. (b) Experimental caSPIR image of a single 100 nm PS bead and cross-section profile. (c) Simulated caSPIR image of a delta function and cross-section profile.

We experimentally validated our technique using polystyrene (PS) nanospheres with 100 nm nominal diameter. A total of 12 sample images were acquired by rotating the source mount in 30° steps. The experimental images under each asymmetric illumination show excellent agreement with the simulated PSFs (see Figure 4·7a). The resolution limit of caSPIR is experimentally measured from these images and then benchmarked against the theoretically simulated results. During the reconstruction, the low-resolution raw images were effectively superimposed in the Fourier space, and a single high-resolution image of the PS beads was reconstructed by solving the least square problem with Tikhonov regularization discussed above. As shown in Figure 4·7b, the 100 nm PS bead cross-section had a full width at half maximum (FWHM) of $\sim$ 179 nm by Gaussian fitting. The FWHM of system PSF can be then estimated as $\sim$ 148 nm by performing deconvolution of the reconstructed PS bead's FWHM with its nominal size under a Gaussian object assumption. Furthermore, we calculated the theoretical PSF by reconstructing the computationally generated images. The images were obtained by convolving the calculated asymmetric illumination PSFs with a delta function. White Gaussian white noise with a signal-to-noise ratio of 10 was added to each image, which matches the SNR of the experimental conditions for the 100 nm PS bead. The FWHM of the cross-section in Figure 4·7c was $\sim$149 nm. This shows our theoretically determined PSF for the caSPIR technique matches the measured PSF, hence, we can reliably reconstruct our objects under these approximations. We also note that caSPIR provides a twofold improvement in lateral resolution and surpasses the resolution limit of conventional interferometric microscopy.

4.7 Resolution characterization

The methods described above for providing high-contrast/resolution images were further validated using a custom-fabricated resolution target. Since there is no industry standard resolution target for interferometric nanoparticle imaging, we imprinted dielectric nanostructures at various sizes and geometries, *e.g.*, bars and words, into a SiO_2 layered substrate using the EBL process as shown in Figure 4·8. We followed

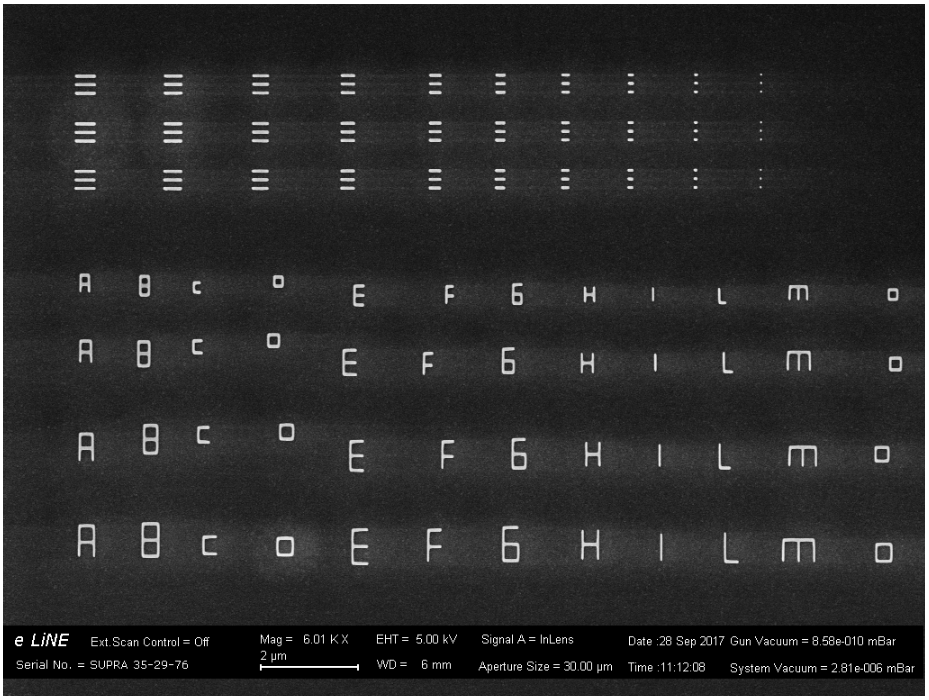
e LiNE
Ext.Scan Control = Off
Serial No. = SUPRA 35-29-76
Mag = 6.01 K X
2 µm
EHT = 5.00 kV
WD = 6 mm
Signal A = InLens
Aperture Size = 30.00 µm
Date :28 Sep 2017
Time :11:12:08
Gun Vacuum = 8.58e-010 mBar
System Vacuum = 2.81e-006 mBar

Figure 4·8: SEM image of example patterns imprinted on EBL sample. The sample is fabricated in colloboration with Prof. Ekmel Ozbay at Bilkent University Nanotechnology Research Center (NANOTAM).

the previously reported EBL process [Işil et al., 2018]. Briefly, 80 nm SiO_2 layer is formed on silicon substrate by a plasma-enhanced vapor deposition coating. Then, Hydrogen silsesquioxane (HSQ) was spin-coated as a resist material because transforms into SiO_2 after e-beam exposure. Nanostructure patterns were written on the sample using EBL, followed by immersion with developer solution. Our EBL sample consists of feature groups defined by their constituent nanostructure geometries. Elements within feature groups were fabricated with different dimensions of known size. Each element was replicated 100 times in a 10×10 grid to account for possible variations due to fabrication errors. The imprinted nanostructures resemble the morphology of existing BNPs such as filamentous viruses and exosomes [Daaboul et al., 2014, Daaboul et al., 2016]. Furthermore, dielectric properties of the EBL sample material (SiO_2), *e.g.*, low refractive index ($n \approx 1.47$) and polarizability, are comparable to that of typical BNPs. Our EBL sample thus provides an invaluable validation tool for investigating not only the proposed method but also prospective methodologies in SPIR microscopy for biological studies.

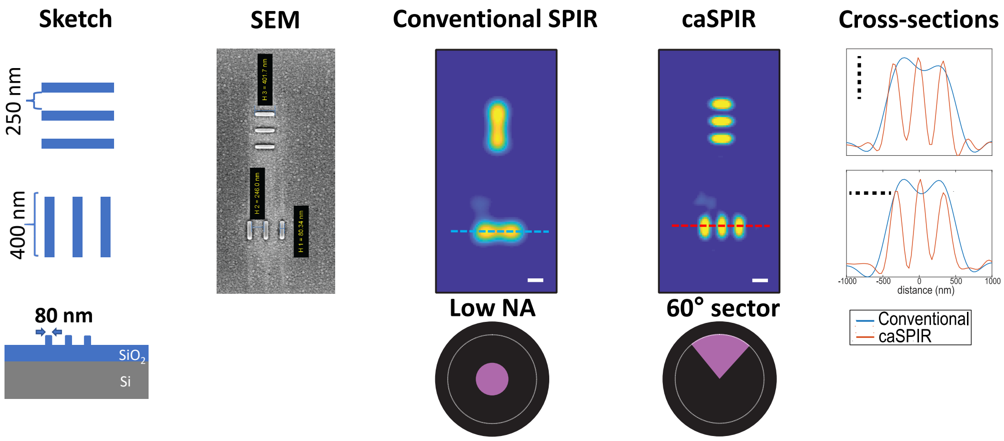

Figure 4·9: System evaluation of caSPIR with 250 nm separated nanobars. The EBL sample was inspected on FE-SEM (ZEISS, GeminiSEM 300) without any preparation process to preserve the sample. Scale bars are 300 nm.

To systematically evaluate the performance of caSPIR, we imaged the bar nanostructure (nanobars) feature groups from the EBL samples and compared them to scanning electron microscopy (SEM) images. Each element had two orthogonal subgroups of three nanobars as shown in Figure 4·9. The nanobars were separated at distances ranging from 250 nm down to 100 nm and have a nominal size of 80 nm by 400 nm (see SEM images in Figure 4·10). The separation is defined as the edge-to-edge distance of two successive bar structures. In Figure 4·10, we demonstrated high-resolution recovery of these nanobars and presented their cross-section along the indicated vertical and horizontal dashed lines. The caSPIR technique significantly improved the lateral resolution down to 125 nm (edge-edge) according to the Sparrow limit. By contrast, the diffraction-limited resolution of the conventional SPIR is approximately 300 nm and nanobars even with 250 nm separation cannot be resolved. As a result, caSPIR demonstrated at least twofold improvement in the lateral resolution. Furthermore, caSPIR maintained similar high-contrast signal levels compared to that of conventional SPIR. We note that for the direct comparison of the two modalities, the conventional SPIR images were also reconstructed with Tikhonov regularization using the theoretically calculated PSF with the aforementioned parameters.

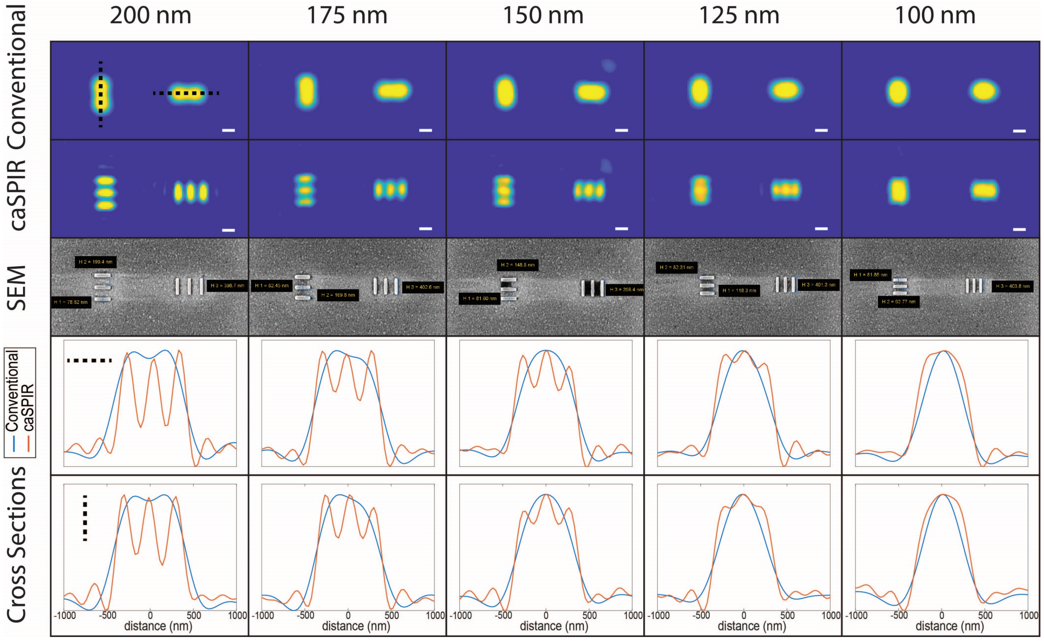

Figure 4·10: System evaluation of caSPIR with bar nanostructures. The conventional SPIR and caSPIR images, and SEM images of 200 nm, 150 nm, 125 nm, and 100 nm separated nanobars. Vertical and horizontal profiles of the conventional SPIR (blue) and caSPIR (red) images. Scale bars are 300 nm.

To demonstrate its robustness, we generated reconstructions for various regularization parameter values that are an order of magnitude larger and smaller than the tuned parameter (see Figure 4·11). These results indicated that the parameter choice was not critical within the close interval of its nominal value. Moreover, as shown in Figure 4·12, the results from the L-curve were consistent with the manually tuned parameter. The manually determined value fell on the corner of the

L-curve for Tikhonov regularization as shown in Figure 4·12). Note that we first determined the regularization parameters for both caSPIR and conventional SPIR using the well-known EBL sample and then used the same parameters throughout all reconstructions.

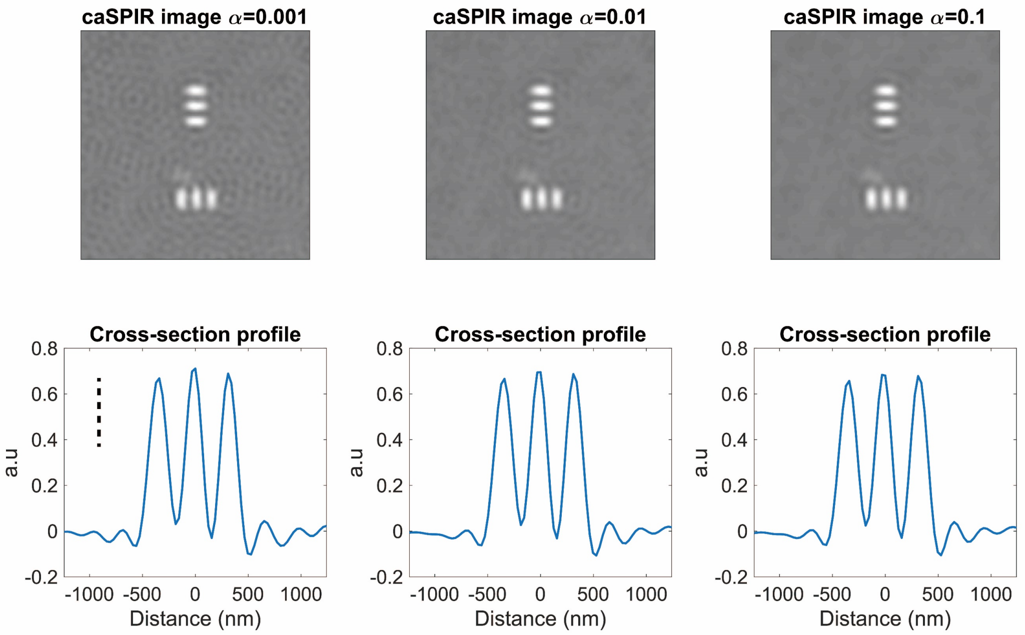

Figure 4·11: Regularization parameter sweep. Different solutions are generated by sweeping the regularization parameter (α) from $0.1 \times \alpha_0$ to $10 \times \alpha_0$, where $\alpha_0 = 0.01$ is the chosen parameter. (Top) Reconstructed caSPIR images of 250 nm separated nanobars. (Bottom) Cross-section profiles along the horizontal nanobars. The results demonstrate that the choice of the regularization parameter is not critical within the close range of the selected parameter.

Under asymmetric illumination, one possible concern arises when considering the loss of frequency support along the axes of asymmetry in the reconstructed image. Without multiple asymmetric illuminations at different angles of the asymmetry axis, this frequency loss could create non-uniform resolution improvement that generates artifacts in the object reconstruction. Especially, the results from orthogonal nanobars might raise the question of whether the resolution enhancement is only limited

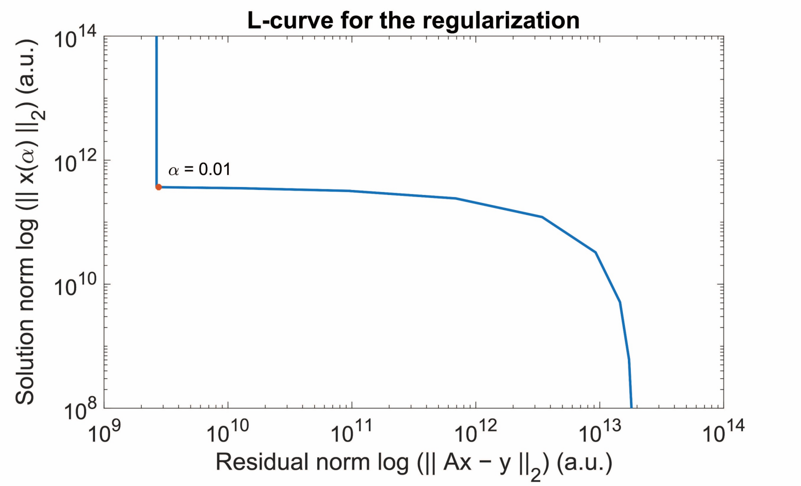

Figure 4·12: L-curve for the regularization parameter sweep in Tikhonov regularized solution. It is calculated for caSPIR image in Figure 4·9. The selected regularization parameter ($\alpha = 0.01$) falls nearby the L-curve's corner.

to along two axes, *e.g.*, x and y. To address this concern, we imaged the nano-words feature group in the EBL sample. As shown in Figure 4·13a, caSPIR recovered high-resolution nanostructure features uniformly across multiple orientations over a large field-of-view (FOV) of $> 100 \times 100$ µm^2. Image outsets (Figure 4·13b,c) further emphasized the resolution advancement along all directions. We also observed contrast variations within each geometry such as S and B nano-letters in both conventional and caSPIR images. These variations could be attributed to non-uniformity during the fabrication process as shown in Figure 4·14. Overall, these results showed that asymmetric images from multiple axes of asymmetry recover the missing frequency support, in turn, improving the lateral resolution in all directions.

4.8 Sensitivity characterization

The interferometric detection in caSPIR has a noise-floor dominated by the shot-noise because the interferometric signal has a very small contrast over a very large background signal due to reflected light. The detection sensitivity of caSPIR is limited by

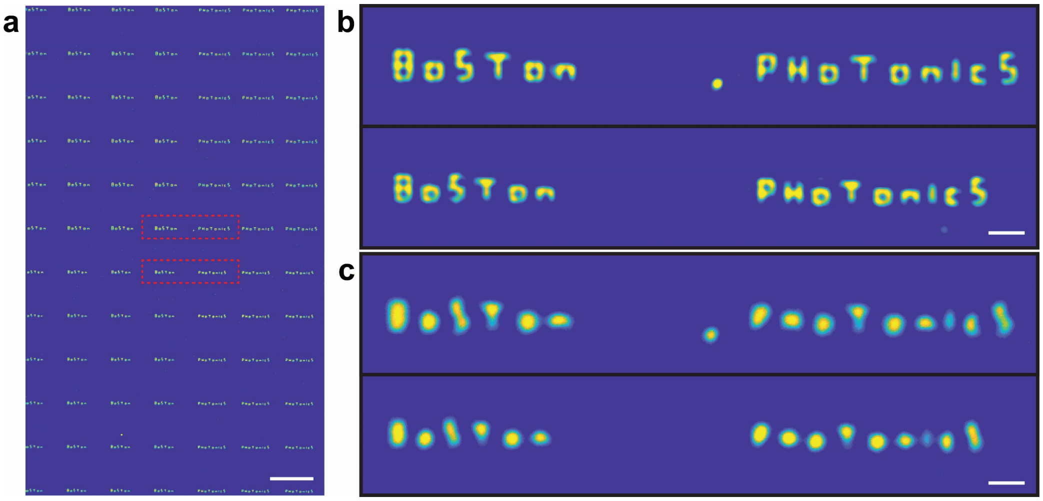

Figure 4·13: caSPIR imaging of nano-words. (a) Full FOV caSPIR image. Insets (b) and (c) are the zoom-in region of interest areas of caSPIR and conventional SPIR images, respectively. Scale bars in (a) and (b,c) are 10 µm and 1 µm, respectively.

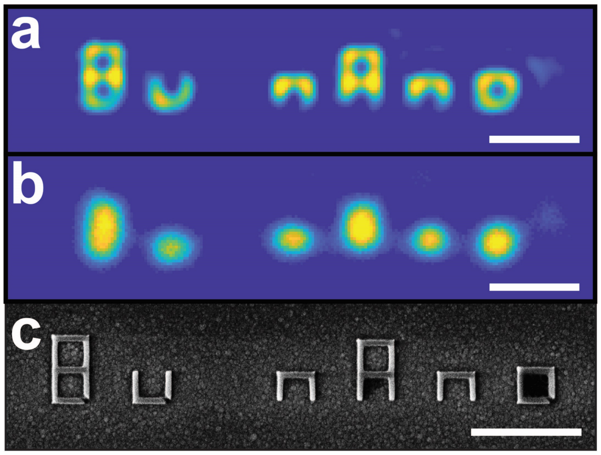

Figure 4·14: Fabrication non-uniformity in EBL sample. (a) caSPIR, (b) conventional SPIR, and (c) SEM images of nano-word *BU NANO*. Fabrication non-uniformity can be clearly seen at the corners of the nano-letters. Scale bars are 1 µm

the camera's shot-noise which can be calculated using the camera specifications including well-depth. The full well capacity of the CCD sensor in the system is 6125 e-.

During the acquisitions, the exposure time was set according to the background signal's intensity histogram, filling ∼60% of the pixel wells to prevent the over-saturation of the camera. The shot-noise for the background was estimated to be 61 e-. Thus, the theoretical detection sensitivity to distinguish a signal from the background was 1.65% in a single captured image. This theoretical calculation was consistent with the standard deviation of the background (1.7%) in a single asymmetric illumination in Figure 4·15. However, the overall sensitivity limit of caSPIR depends on the sample's signal contrast. The maximum and minimum contrast values along the 100 PS bead's cross-section profile were ∼15% and ∼12%, respectively. As we stated in the previous sections, the captured intensity contrast scales linearly with the sample's volume. As a result, we anticipate that caSPIR can detect PS beads with sizes down to ∼50 nm for the aforementioned parameters, since this approximately reduces the contrasts to 1.88% and 1.5%, making the signal to noise ratio drop to around 1. We would also like to emphasize that these limits are specific to camera configurations and could be further improved by utilizing the full capacity of the pixel wells and frame averaging, both of which will reduce the noise level. This stems from the fact that the scattering signal does not have limitations associated with fluorescence detection such as saturation and photobleaching. For instance, the noise floor can be reduced to nearly 1.3% in a single acquisition by increasing the exposure time to saturate 95% of the pixel well depth. Frame averaging reduces the shot noise by the square root of the number of averaged frames. Figure 4·15 shows that SNR improved by averaging more frames. In practice, excessive frame averaging is not possible because the measurement accuracy could be hindered by unknown mechanical vibrations and sample drift. Moreover, the background fluctuations due to optics and substrate become the dominant source of artifacts. This can be further improved by flat-field correction and background subtraction.

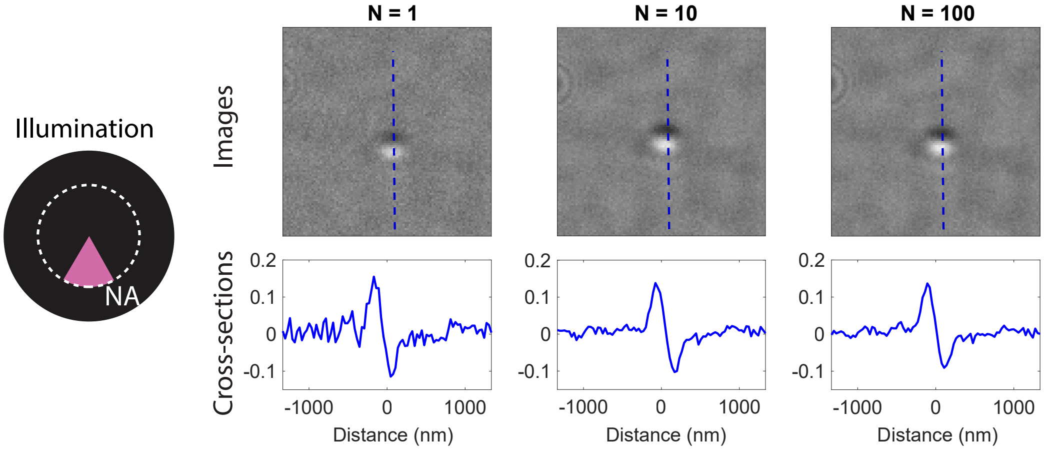

Figure 4·15: Sensitivity characterization of caSPIR. 100 nm PS bead cross-section profile captured under the asymmetric illumination with different number of frames (N) averaged. The image is normalized with the background signal, followed by background subtraction. The standard deviation of the background is ∼0.017.

4.9 Artificial nanocarrier experiments

We next determined the system's performance with low-index ($n \approx 1.46$) poly (lactic-co-glycolic acid) PLGA nanospheres/rods. Owing to its biodegradability and biocompatibility with well-established synthesis techniques, PLGA shows great promise for drug delivery and nanomedicine applications including targeting, imaging, and therapy. PLGA was approved by the Food and Drug Administration (FDA) as well as the European Medicine Agency for drug delivery systems (DDSs). This versatile polymer can deliver a large size range of hydrophobic and hydrophilic therapeutic agents, ranging from small drug molecules to proteins, nucleic acids, and other macromolecules [Mir et al., 2017, Dinarvand et al., 2011, Chereddy et al., 2016, Pagels and Prud'homme, 2015]. While PLGA microparticle DDSs like Atridox®, Sandostatin®, Trelstar® and Lupro® depots are already in use clinically, several PLGA nanoparticle DDSs are currently undergoing clinical trials [Mir et al., 2017]. Besides, PLGA's easy tunability of physicochemical properties, e.g., size, shape, and surface chemistry, enables desirable biological interactions and drug release profiles. The drug delivery performance of particulate DDSs is strongly dependent on their physical parameters. For this reason, the direct high-resolution imaging of PLGA nanocarriers at high-throughput in a single experiment becomes highly desirable for accurate morphological characterization.

4.9.1 Synthesis of PLGA nanospheres

Poly (D, L-lactide-co-glycolide) resomer® RG504H (PLGA, acid terminated, lactide:glycolide 50:50, 38000-54000 Da), glycerol and mineral oil, dichloromethane (anhydrous, $\geq$99.8%), and polyvinyl alcohol (PVA, 98-99% hydrolyzed and 87-90% hydrolyzed) were purchased from Sigma-Aldrich (St. Louis, MO). PLGA nanospheres were synthesized using a double emulsion solvent evaporation method. 10 mg PLGA polymer was dissolved in 1.5 mL anhydrous dichloromethane. 0.15 mL MilliQ water was added to it and the mixture was subjected to bath sonication (Branson UltrasonicsTM CPX952139R) at 40 kHz for 3 min to form a water-in-oil (w/o) emulsion. This primary emulsion was further emulsified by the addition of 10 mL of 0.5% PVA (98-99.8% hydrolyzed) solution under vigorous stirring, followed by probe sonication (Sonics and Materials Inc. VCX 600) at 20 kHz operating frequency for 40 s with pulsation at 70% amplitude in an ice bath. The resulting double emulsion (w/o/w) was kept stirring at 400 rpm overnight at room temperature for the evaporation of dichloromethane. The PLGA nanospheres were retrieved by centrifugation of the aqueous suspension at 9000 rcf for 20 min, followed by multiple washes with MilliQ water. The washed nanoparticles were then resuspended in MilliQ water and stored at 4°C for further use.

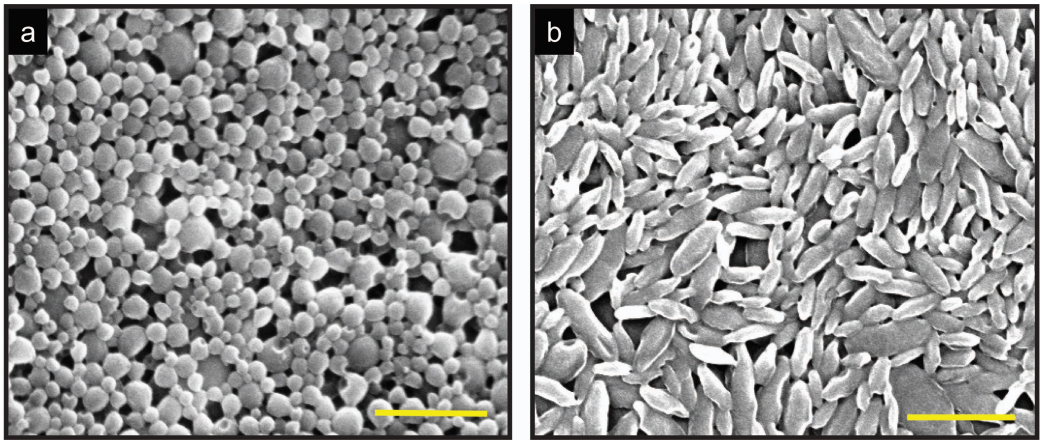

Figure 4·16: SEM micrographs of PLGA (a) nanospheres and (b) nanorods, respectively. The PLGAs are fabricated in colloboration with Prof. Samir Mitragotri at Harvard University. Scale bar is 1 µm

4.9.2 Fabrication of PLGA nanorods

Rod-shaped particles were fabricated using a previously reported one-dimensional polymer film stretching method described in [Champion et al., 2007]. Briefly, $\sim 10^8$ PLGA nanospheres were suspended in 80 mL 6.25% w/V aqueous solution of 87-90% hydrolyzed PVA. 1.25% v/V glycerol was added as a plasticizer to lower the glass transition temperature of the films and facilitate stretching. The mixture was then cast into a film and dried for 24 hours at room temperature to immobilize the PLGA particles. The dried films were mounted on a 1-D mechanical stretcher, heated for 5 minutes at 70°C in mineral oil, and stretched to obtain the desired prolate geometry. The stretched films were cooled to room temperature for 10 minutes to allow solidification of the particles in their new shape. Suitable sections were cut from the stretched films for their dissolution in MilliQ water at room temperature and were centrifuged at 8000 rpm for particle recovery. The isolated particles were subsequently washed thrice with MilliQ water via centrifugation and finally passed through a 100 µm filter, for the removal of residual PVA.

4.9.3 Preparation of PLGA sample

PLGA rods and spheres with deionized water were suspended by vortexing for a minute followed by 5 minutes of sonication at room temperature. They were mixed 1:1 without any dilution. Before immobilization of the sample, the SiO_2 chip surface was plasma ash treated with oxygen for 5 minutes. Doing so, the surface becomes hydrophilic and the sample solution spreads over the surface. Then, the PLGA rod and sphere mixture was spin-coated onto the chip surface at 3000 RPM for 10 seconds.

4.9.4 Experiments on PLGA nanocariers

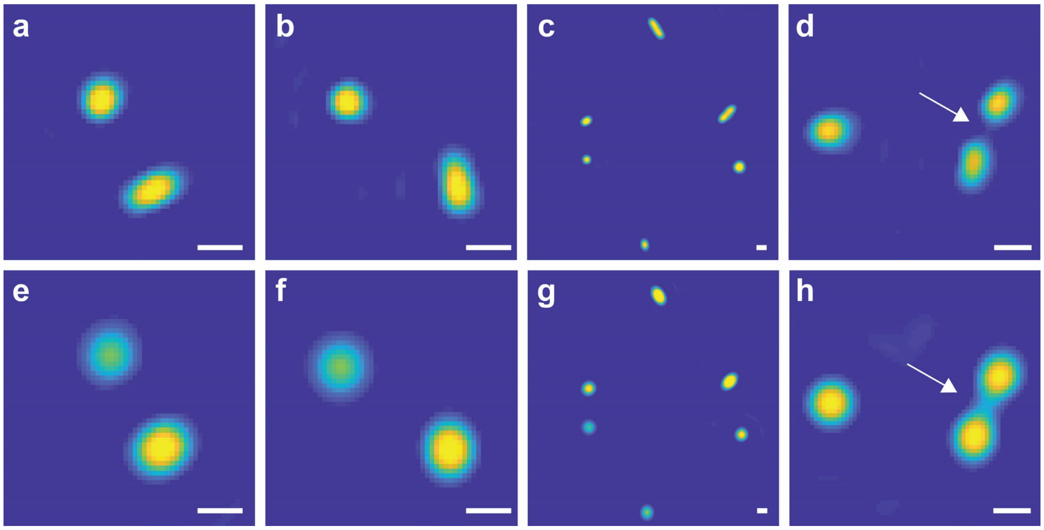

Figure 4·17: caSPIR imaging of biodegradable PLGA nanospheres and nanorods. (a-d) caSPIR images and (e-h) their corresponding conventional SPIR images. Scale bars are 300 nm

We demonstrated high-resolution visualization of PLGA nanoparticles in Figure 4·17. The PLGA sample is prepared by spin coating the mixture of PLGA nanospheres and nanorods on the SiO_2 chip surface. PLGA nanorods, in prolate geometry, are fabricated using a polymer film stretching method applied on the synthesized PLGA nanospheres as detailed above. As shown in the SEM micrographs of the spherical and rod-shaped PLGA nanoparticles in Figure 4·16, the fabricated nanoparticles exhibit polydispersity in both size and aspect ratio. Geometrical parameters of the PLGA nanocarriers in the EBL sample were characterized using field emission scanning electron microscopy (FE-SEM). PLGA nanoparticles underwent a sample preparation process which involves vacuum drying of 10 µL particle suspension on an aluminum stub, followed by 5 nm thick coating with platinum-palladium using EMS 150T S Metal Sputter Coater (Quorom Technologies, U. K.). The sputter-coated PLGA samples were imaged using FE-SEM (ZEISS, Supra55VP). Having a large size distribution with varying degrees of ellipticity (in prolate spheroid geometry) makes these particles ideal for morphology characterization with caSPIR. With conventional SPIR, the system's low resolution in a high-throughput visualization of these polydisperse nanocarriers could lead mischaracterize their morphology. In particular, nanorods with small eccentricity appear as spherical particles. As demonstrated in Figure 4·17a-c, the caSPIR image outsets clearly show the particle elongation. In addition, the caSPIR offers a more informative means for distinguishing closely separated particles indicated by arrows in Figure 4·17d,h. Based on these results, we reasoned that advanced discrimination and morphological characterization in SPIR microscopy highlights its utility in improving BNP visualization in a high-throughput manner.

4.10 Virus experiments

4.10.1 Creation and use of Virus and VLP sample

Ebola VLPs was generated by transfection of HEK293FT cells with pCAGGS-based plasmids encoding each EBOV structural protein, (GP, NP, VP30, VP35, VP24, VP40) except for the viral polymerase, L, together with a plasmid encoding the red fluorescent protein, mKate2, fused to VP40. The inclusion of mKate2-VP40 allowed visualization of particles by conventional fluorescence microscopy and the amount used was optimized for VLP formation. Cells were plated in 10 cm culture dishes to 80% confluency 2 hours prior to transfection. Each 10 cm dish was transfected with a total of 15 µg of plasmid DNA using calcium phosphate [Chen and Okayama, 1987]. Transfection reagents were removed, and cells were washed with Dulbecco's Phosphate Buffered Saline (PBS) after 15 hours, followed by the addition of 10% Fetal Bovine Serum containing DMEM. Cells were cultured at 95% humidity, 37°C, 5% CO_2 for 48 hours. The culture medium was collected and clarified by centrifugation (1500 × g) prior to the concentration of VLPs by ultracentrifugation at 159000 × g for 2 hr at 4° C through a 10 mM HEPES buffered (pH 7.4) isotonic 8.2% sucrose cushion. Pellets were resuspended in Dulbecco's PBS and banded through an isotonic iodixanol gradient to remove trace culture medium contaminants. Aliquots of banded VLPs were snap frozen in liquid nitrogen and stored at -80°C until use.

In this study, VSV-based viruses that lack the endogenous VSV glycoprotein and express the Ebola virus glycoprotein from an independent transcription start/stop sequence placed in between the M and L genes of the VSV genome were used. Expression of the Ebola virus glycoprotein was confirmed by Western blotting using glycoprotein-specific proteins. Virus stocks were prepared using Vero cells cultured in DMEM supplemented with 10% FBS, as described previously [Garbutt et al., 2004]. Virus titers were determined by standard plaque assay methods and then diluted in PBS before incubation. VLP amounts were assessed by Western blot of the Ebola virus glycoprotein.

4.10.2 Antibody microarray assay preparation

60 nm SiO_2 chips were coated with a solution of antifouling NHS copolymer (Lucidant Polymers MCP-2) dissolved 1:100 in 1.2M Ammonium Sulfate. Antibodies targeting the Ebola glycoproteins were spotted onto activated, polymer-coated chips, as were non-specific antibodies (as controls) using the sciFLEXARRAYER S3 (Sci-

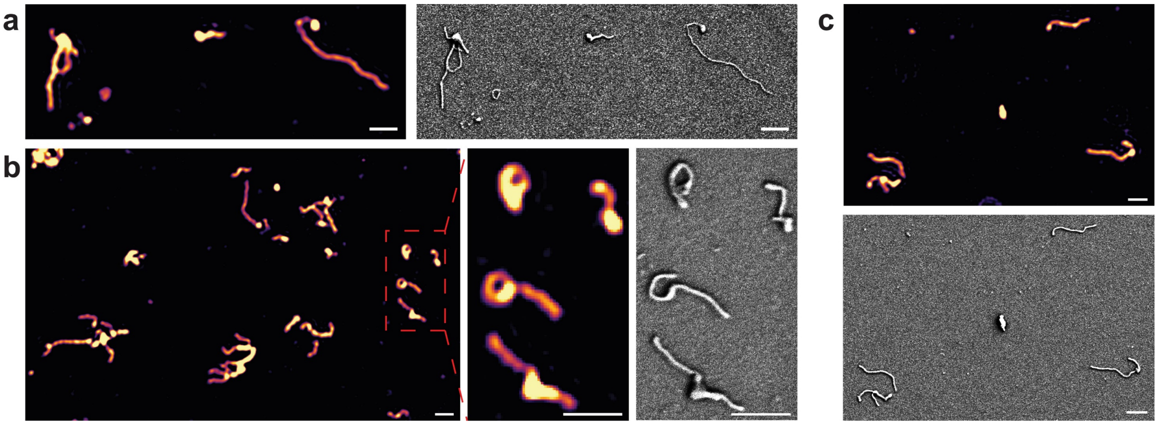

Figure 4·18: caSPIR imaging of Ebola virus like particles. (a-c) (Left) caSPIR images and (Right) SEM images. SEM image area in (c) is indicated by a box. (d) caSPIR image. The Ebola VLP sample was coated by gold using sputter coater (Cressington, 108) and imaged on FE-SEM (ZEISS, Supra 55VP). Scale bars are 1 µm.

enion AG). Chips were dried overnight and then washed with Tris-buffered saline + 0.1% Tween20. Chips were then rinsed with milliQ water at least 6 times, and removed from the dish at a 45° angle so that water wicks off the top surface, and then dried on a KimWipe with N_2 gas [Carter et al., 2017]. Chips were scanned with a custom 1.5X magnification instrument (Nanoview Biosciences) to ensure the correct spot morphology. Note that since both Ebola virus-like particles and recombinant vesicular stomatitis virus Ebola have the same surface glycoproteins, the same microarray preparation protocol is followed for each.

For virus loading, chips were placed in 24 well plates, etched-side up. 750 µL of virus solution was added to the wells containing the chips, and the plates were put on an orbital shaker for 1 hour at ∼150 RPM. Chips were then removed from the sample containing wells with forceps and placed in wells containing 0.1X PBS (Gibco 10010023) + 0.01% Tween20, followed by washing on the orbital shaker for 5 minutes. This process was repeated twice, then the chips were placed in individual 60 mm dishes containing milliQ water, and rinsed by swirling for a few seconds. Chips were dried by removing them from their dishes at a 45° angle followed by placing them face-up on a KimWipe.

4.10.3 Experiments on Ebola VLPs

To explore the potential of caSPIR in analyzing BNPs, we examined its ability to accurately characterize a heterogeneous mixture of Ebola virus-like particles (EBOV VLPs). Ebola virus is a highly pathogenic virus that has caused thousands of deaths and explosive outbreaks. The infected cells produce multiple Ebola virions, showing various shapes and size distributions. Some virions are filamentous, 90 nm width and one to multiple microns in length, and the others appear in circular, 6, or toroid shapes that can be 4-500 nm in diameter [Bharat et al., 2012]. The filamentous Ebola virion has been suggested to have greater infectivity [Campbell et al., 2014]. For these reasons, direct high-resolution imaging of EBOV VLPs at high-throughput in a single experiment becomes highly desirable for accurate morphological characterization. However, label-free visualization of these viruses in SPIR microscopy is even more challenging than fabricated nanostructures because their smaller size and lower refractive index lead to much weaker contrast. Fortunately, the refined SPIR with asymmetric illumination provides simultaneous contrast and resolution enhancement with high SNR.

EBOV-VLPs were obtained using a transfection protocol as detailed above. To capture the EBOV-VLPs, we utilized a microarray printed on a SiO_2 chip surface. The microarray consists of ∼150 µm diameter antibody spots and negative control spots that capture the rVSV-EBOV and other viral glycoproteins, respectively. Before and after incubation, both positive and negative spots were imaged with conventional SPIR to ensure the specific binding. caSPIR clearly resolved the various EBOV structures and discriminate against their morphological differences, consistent with the SEM images as shown in Figure 4·18. We also observed that EBOV VLPs could form

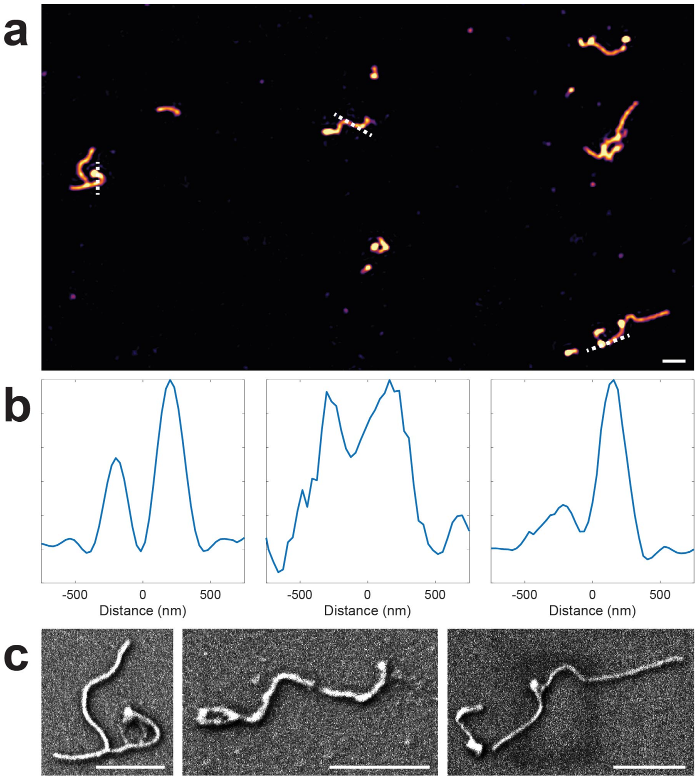

Figure 4·19: Ebola VLP cross-sections in caSPIR images. (a) caSPIR image. **b,c** (Left to right) cross-section profiles indicated by dash lines in (a), and SEM images of the indicated VLPs, respectively. Scale bars are 1 µm.

branched filaments. The cross-section profiles in Figure 4·19b showed that caSPIR can distinguish closely separated (<200 nm) VLP structures and revealed both bent and straight VLP morphology. Furthermore, caSPIR images showed a higher contrast at the tips of the viral particles. This result was consistent with the classic "shepherd's crook" shapes where increased mass creates locally high polarizability and thus leads to a more intense signal. Prior electron microscopy studies have shown that the ability to measure the length and density of EBOV virions correlates with the number of genomes incorporated [Beniac et al., 2012], suggesting that caSPIR could be used to "count" the number of genomes incorporated into an Ebola virus particle.

4.10.4 Experiments on Ebola VSVs

We also imaged a leading Ebola virus vaccine candidate (rVSV-EBOV). This vaccine is a bullet-like (approximately 80 nm by 180 nm [Daaboul et al., 2014]) recombinant Vesicular Stomatitis Virus (rVSV) that expresses EBOV glycoprotein and can be captured for imaging by the same antibody used to capture and image EBOV VLPs. rVSV-based vaccine candidates have shown great promise against Ebola disease and are have been deployed to combat Ebola outbreaks in Africa [Henao-Restrepo et al., 2017]. The promise of rVSV-vaccines brings with it a need to assess the quality of vaccines produced for human use. In this context, characterizing the monodispersity of the rVSV-based vaccine candidates and its distinctive "bullet" shape along with an assessment of the genetic "payload" carried by a virion would aid vaccine development and quality assurance.

As demonstrated in Figure 4·20a, we were able to simultaneously visualize more than 1,350 rVSVs-EBOV in the FOV at high resolution. Since this technique provides 150 nm lateral resolution, it can be utilized on denser samples that have more than 10^4 particles in a FOV. As shown in Figure 4·20 b,c,f,g, caSPIR enables the morphological characterization of rVSVs, which was previously not possible in SPIR microscopy. Although two rVSVs indicated by a dashed circle in the caSPIR image (Figure 4·20d) appear to be spherical, they are mischaracterized as an elliptical structure with conventional SPIR (Figure 4·20h). This problem occurs because the background artifacts are more pronounced in the conventional SPIR image reconstructions that recover the object from a single illumination configuration. The main background artifact sources include back-reflections from the optics and the surface roughness of the camera sensor glass and SiO_2 chip. Over different illuminations, these artifact components remain stationary compared to the varying particle signal. Under multiple asymmetric illuminations, these static background artifacts become separated from the object's

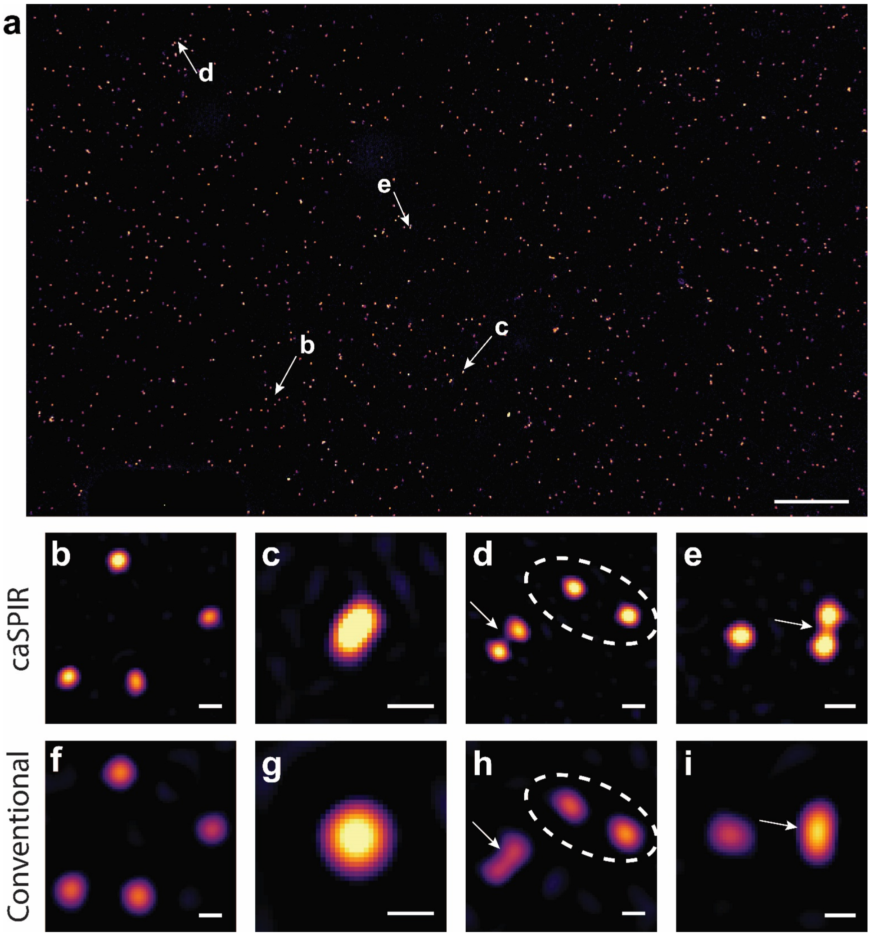

Figure 4·20: caSPIR imaging of recombinant Vesicular Stomatitis Virus Ebola model. (a) Full-FOV caSPIR image (∼1350 VSVs in the FOV). (b-e) Zoom-in areas indicated by arrows in (a), and (f-i) their conventional SPIR images, respectively. Scale bar in full-FOV image is 10 µm and scale bars in zoom-in areas in (b-i) are 300 nm.

signal and are greatly reduced. We note that the signal contrast from an individual virion under asymmetric illumination has lower SNR compared when compared to conventional SPIR. Yet with multiple illuminations, caSPIR achieves ultrasensitive imaging of very small particles with high-SNR. We anticipate that combinations of multiple low-NA illuminations from different parts of the back-pupil would allow for additional SNR improvement. Moreover, caSPIR offers a more informative means for distinguishing closely separated particles and thus prevents misleading morphological characterizations of individual virions in dense samples. The high-resolution images clearly discriminate two individual rVSV particles that were close enough to appear as a single elongated particle in conventional SPIR (compare arrows in the outsets in Figure 4·20d,e,h,i). With these improvements, the SPIR imaging platform enables accurate morphological characterization of thousands of individual viruses simultaneously.

4.11 Conclusion

In this chapter, we demonstrated high-throughput direct visualization of low-index nanoparticles at sub-wavelength resolution. We formulated the vectorial PSF of caSPIR using optical theory and implemented a computationally efficient linear inverse scattering approach. We demonstrated a two-fold improvement in lateral resolution of the conventional SPIR and achieved lateral resolution of ∼148 nm using visible light (420 nm) under a 100×/0.9 NA objective. This wide-field technique provided a large field-of-view of 100 µm × 100 µm, allowing for sub-wavelength imaging over 10^4 BNPs at once. We specifically focused on the concept demonstration of this technique and its resolution capability using an artificial nanostructure sample fabricated by an EBL process. To demonstrate the biological relevance, we studied filamentous Ebola VLPs and an rVSV based Ebola virus vaccine candidate as model viruses. These model viruses are surrogates of wild-type, clinically relevant pathogens. Namely, Ebola VLPs have been shown to closely resemble Ebola virus [Bharat et al., 2012] and the rVSV-EBOV resembles that of parent rhabdovirus [Ge et al., 2010].

Conventional approaches for morphological characterization of viruses in solution use indirect methods such as fluorescent labeling often relying on genetic modification of viral proteins [Brandenburg and Zhuang, 2007]. Historically, direct imaging of unmodified viruses has relied on laborious imaging techniques such as electron microscopy that can cause sample desiccation and degradation. Our low-cost light microscopy technique, caSPIR, enables high-resolution imaging of BNPs without any modification or sample preparation thus allowing for analysis of clinical isolates directly. To conclude, our study could enable exciting possibilities for high-throughput, ultrasensitive, and label-free imaging and characterization of a broad-size spectrum of biological nanoparticles at high resolution. In particular, with the integration of the computational asymmetric illumination modality, this versatile wide-field interferometric microscopy technique – SPIR microscopy– could bridge the gap between scanning electron microscopy and conventional optical microscopy.

Chapter 5

Bond-selective interferometric microscopy

5.1 Introduction

In the previous chapters, we discussed various methods in SPIR microscopy to achieve high-resolution and sensitive label-free imaging of biological nanoparticles. Although we demonstrate that SPIR can reveal particle morphological information including size and shape, the chemical composition of particles is inaccessible in interferometric measurements. To date, molecular specificity in these studies is limited to the surface affinity of assays. Therefore, functional analysis of single biological nanoparticles remains unsolved in interferometric microscopy techniques including SPIR and iSCAT.

To obtain molecular information beyond the surface affinity, vibrational spectroscopic imaging methods have enabled molecular fingerprinting of molecules with high chemical specificity [Cheng and Xie, 2015]. Inelastic Raman scattering or optical absorption has been utilized in various optical sensing methods to probe spectroscopic signatures of chemical bonds. The Raman scattering microscopy techniques rely on a non-linear scattering process to achieve diffraction-limited-resolution [Turrell and Corset, 1996, Freudiger et al., 2008]. Fourier transform infrared (FTIR) microscopy utilizes linear infrared (IR) absorption, yet the long illumination wavelengths in FTIR limit its resolution to several microns which is inadequate for studying sub-cellular features [Baker et al., 2014, Levin and Bhargava, 2005]. As a tip-based approach, atomic force microscope infrared spectroscopy (AFM-IR) techniques can resolve structures at the nanoscale (20 nm) but its applications are typically limited to dry samples due to contact requirement [Dazzi et al., 2012, Huth et al., 2012]. Recently developed mid-infrared (mid-IR) photothermal (MIP) microscopy demonstrated optical detection of photothermal effect induced by IR absorption of the specimen using a visible probe beam [Zhang et al., 2016a]. In principle, the MIP contrast mechanism is similar to those reported in the photothermal microscopy field [Boyer et al., 2002, Gaiduk et al., 2010, Berciaud et al., 2006, Selmke et al., 2012]. This emerging technique have been recognized widely in the chemical imaging field and continuously evolved in various geometries including scanning-based [Zhang et al., 2016a, Pavlovetc et al., 2020, Samolis and Sander, 2019] and wide-field [Bai et al., 2019, Zhang et al., 2019, Toda et al., 2019, Tamamitsu et al., 2019, Tamamitsu et al., 2020, Schnell et al., 2020] illumination. A wide range of applications spanning from material science to life science has been reported by scanning MIP techniques [Klementieva et al., 2020, Chatterjee et al., 2018, Li et al., 2019, Zhang et al., 2021, Samolis et al., 2021].

Although its great sensitivity down to a single virus level [Zhang et al., 2021], scanning MIP has inherent limitations associated with scanning itself such as slowness, low-throughput, and mechanical instability. Bai *et al.* [Bai et al., 2019] has overcome these challenges and demonstrated a wide-field MIP microscopy approach by probing interferometric reflectance measurement. To achieve this on very fast complementary metal-oxide-semiconductor (CMOS) cameras, a virtual lock-in camera technique has been introduced. Camera-based MIP systems have been already applied to extend various label-free imaging methods including low-coherence interference microscopy [Schnell et al., 2020], quantitative phase imaging [Zhang et al., 2019, Tamamitsu et al., 2020], and dark-field imaging [Zong et al., 2021] and led to applications in histopathology and living cells. However, individual nanoparticle detection in wide-field MIP remains still challenging due to the very weak scattered light from nanoparticles. As a consequence, single nanoparticles are invisible under strong background illumination.

In this chapter, we introduce bond-selective interferometric scattering microscopy for biological nanoparticle fingerprinting. We utilize layered substrate to increase interferometric contrast by reducing background and enhancing the scattered field. By probing the mid-IR absorption-induced photothermal effect, this study enables chemical specificity beyond the surface affinity. Our technique provides vibrational spectroscopic sample information which is not accessible in the previous wide-field interferometric scattering microscopy approaches. A theoretical framework for the interferometric photothermal contrast mechanism is discussed. The system performance is evaluated using poly (methyl methacrylate) (PMMA) film and beads. To show chemical imaging of biological nanoparticles, we provided examples of *Staphylococcus aureus* (*S. aureus*), *Escherichia coli* (*E. coli*), and *Candida albicans* (*C. albicans*). The results show promise for high-throughput and sensitive label-free imaging of a broad size range of individual bio-nanoparticles, including viruses and exosomes, with high chemical specificity.

5.2 Theoretical considerations

5.2.1 Interferometric photothermal contrast mechanism

As described in Chapter 2, wide-field interferometric microscopy utilizes common-path interferometry configuration for highly sensitive and stable coherent detection of scattered light from nanoparticles. To minimize the IR absorption by thin layer, we use 70 nm Si_3N_4/Si substrate as depicted in Figure 5·1. The nitride film thickness d is nearly $\lambda_{Si_3N_4}/4$ where $\lambda_{Si_3N_4}$ is the wavelength of the light propagating in the nitride layer. This specific layer thickness not only minimizes the reflected light through destructive interference but also enhances the total scattered light through

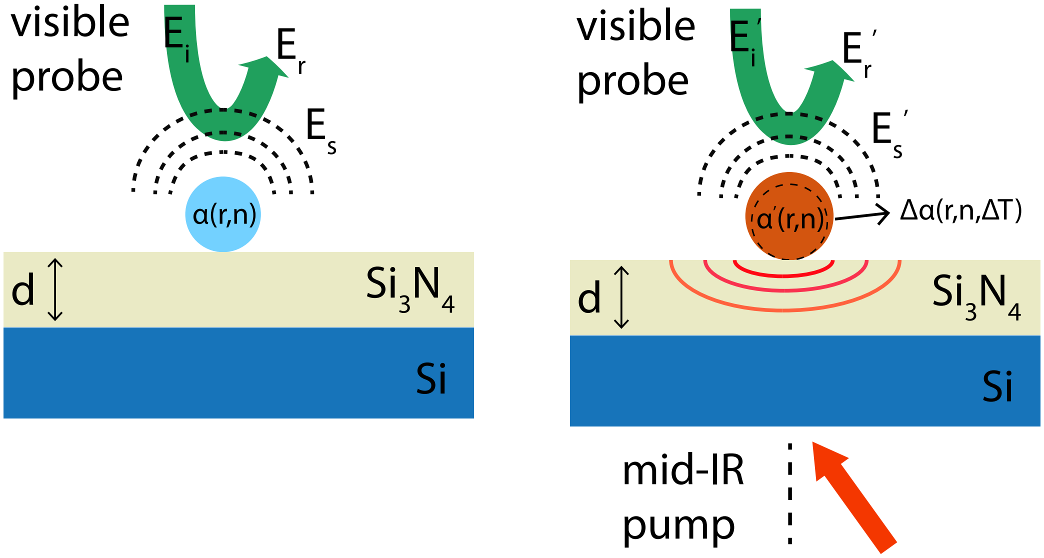

Figure 5·1: Layout of the common-path interferometric detection, nanoparticle is placed on top of 70 nm Si_3N_4/Si layered substrate. The visible incidence field ($\mathbf{E_i}$) scatters from sample ($\mathbf{E_s}$) and reflects off the substrate surface ($\mathbf{E_r}$). The mid-IR pump beam absorbed by the nanoparticle causes temperature rise (ΔT) and induces change in particle's polarizability ($\Delta\alpha$) which is a function of size and refractive index change. The pump is incident on the sample with an oblique angle ($\theta =\sim 62^\circ$) close to the Brewster's angle to improve the IR transmission and to avoid absorption by the OL.

the constructive self-interference of the forward and backward scattered light.

The photothermal signal in our system is measured by probing the change in the interferometric signal. The IR absorption increases the temperature around the vicinity of the nanoparticle. This temperature rise ΔT induces a change in the particle's size and refractive index depending on its linear thermal-expansion β_r = 1/rdr/dT and thermo-optic β_n=1/ndn/dT coefficients. As a result, the nanoparticle's polarizability and the scattered field amplitude change, whereas the reference field is untouched. This process is referred to as the photothermal effect which causes the temperature-dependent signal change. Our formulation, in principle, is similar to the earlier reported photothermal signal theory based on the scattered field from the medium fluctuations [Berciaud et al., 2006, Selmke et al., 2012]. We use the interferometric scattering contrast mechanism discussed in Chapter 2. Using equation 2.12, we can express the signal difference ΔS between IR-on (S^{hot}) and IR-off (S^{cold}) states as follows:

$$\Delta S = S^{hot} - S^{cold} = 2|E_r|\Delta|E_s| \text{and} \Delta|E_s| = |E_s^{hot}| - |E_s^{cold}|, \tag{5.1}$$

where $E_s^{hot} = E_s(T_0 + \Delta T)$ and $E_s^{cold} = E_s(T_0)$ are respectively the scattered fields at the IR-on and IR-off states with the pre-IR pulse temperature of T_0. Equation 5.1 implies that the interferometric photothermal signal is detected through the linear detection of the scattering amplitude change with a strong reference field [Huang et al., 2021]. This has a similar detection principle to that of the interferometric signal. Similar to equation 2.13, the photothermal image contrast can be expressed as the interferometric contrast difference at two states.

$$\Delta S_c = S_c^{hot} - S_c^{cold} = 2\frac{\Delta|E_s|}{|E_r|} = S_c\frac{\Delta|E_s|}{|E_s^{cold}|}. \tag{5.2}$$

We measure the photothermal signal as the intensity difference at the camera. To generalize the photothermal signal quantification, we define the intensity modulation fraction which can be expressed as the ratio of the photothermal signal to the interferometric signal at the pre-pulse state $M_{PT} = \Delta S/S^{cold}$. By plugging equation 2.9, the modulation fraction can be calculated as follows [Zhang et al., 2021]:

$$M_{PT} = \frac{\Delta S}{S^{cold}} = \frac{\Delta S_c}{S_c^{cold}} = \frac{\Delta|E_s|}{|E_s|} \propto \frac{\Delta\alpha}{\alpha} \approx 3\Delta T\left(\beta_r + \frac{2\epsilon_p}{(\epsilon_p + 2\epsilon_m)(\epsilon_p - \epsilon_m)}\beta_n\right). \tag{5.3}$$

The equations above indicate that the photothermal signal contrast scales with the modulation fraction and interferometric contrast. Therefore, reference reduction through either substrate engineering [Avci et al., 2016] or pupil engineering [Avci et al., 2017a, Cole et al., 2017, Cheng et al., 2019] could enhance the visibility of the photothermal signal. The photothermal modulation is typically in negative five-six orders of magnitude for a given 1K temperature rise (see Figure 5·2). For example, PMMA has linear thermal expansion coefficient of $\beta_{\mathrm{r}} = 90 \times 10^{-6}$ K^{-1} [Mark et al., 2007] and thermo-optic coefficient of $\mathrm{n}_{\mathrm{PMMA}}\beta_{\mathrm{n}}$ = -1.1 × 10^{-4} K^{-1} [Kasarova et al., 2010] with a refractive index of $\mathrm{n}_{\mathrm{PMMA}} = 1.49$ [Tsuda et al., 2018]. The modulation fraction for a PMMA bead surrounded in air then becomes nearly 0.01% at ΔT = 2K.

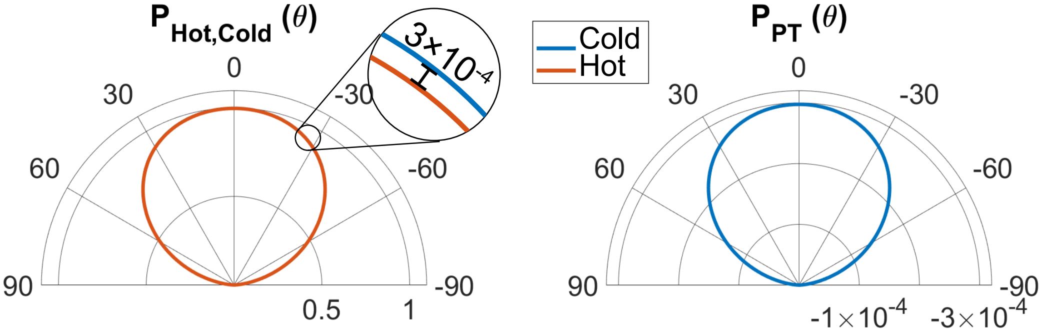

Figure 5·2: Simulated scattering polar plots of 100 nm PMMA bead on silicon substrate in the hot $P_{Hot}(\theta)$ and cold $P_{cold}(\theta)$ states and corresponding photothermal polar plot obtained by subtracting hot and cold states, $P_{PT}(\theta) = P_{Hot}(\theta) - P_{Cold}(\theta)$. The signals are normalized by the maximum intensity value in the cold state. The simulation parameters at 520 nm illumination wavelength: $\theta_{\mathrm{incident}} = 0°$, $\mathrm{n}_{\mathrm{medium}} = 1$, $\mathrm{n}_{\mathrm{silicon}} = 4.2$, $\mathrm{n}_{\mathrm{PMMA}} = 1.49$, dn/dT = - 1.1 × 10^{-4} K^{-1}, dr/dT = 90 × 10^{-6} K^{-1}, $T_0 = 298$ K.

5.2.2 Theoretical simulations

To accurately characterize the photothermal contrast mechanism, we developed an analytical model considering imaging optics and system parameters. We employ image field representation of optical fields that provides better means for physical optical system simulations. Our model is built upon the previously developed theoretical framework for interferometric scattering calculations from an arbitrary shape and size particle near a substrate [Sevenler et al., 2017] and extends to the photothermal signal. The photothermal imaging simulation is split into two steps: (1) numerical evaluation of far-field scattered field from a particle and (2) calculating image fields using diffraction integrals. To do so, we first define the system geometry including the substrate, medium, and particle dielectric functions as well as the illumination wavelength (λ). The vectorial scattered fields at the infinity ($\mathbf{E}_{\mathbf{scat},\infty}$) are then calculated using metallic nanoparticle boundary element method (MNPBEM) toolbox [Waxenegger et al., 2015]. NMPBEM numerically solves full Maxwell's equations for the dielectric environment in which the particle and surrounding medium have homogeneous and isotropic dielectric functions. In calculations, it utilizes the boundary element methods (BEM) [García de Abajo and Howie, 2002] which is a computationally efficient approach for simple geometries. It should be noted that MNPBEM accounts for the substrate effect on internal and driving electric fields using Green's functions. This is very important for accurate analysis of the total back-scattered field considering the reflections from the surfaces. After numerically calculating the far-field scattered field, we perform image formation integrals using angular spectrum representation (ASR) of vectorial electric fields. The ASR framework has been a powerful tool for a rigorous and accurate description of the field propagation in the homogeneous media [Novotny and Hecht, 2006]. The electric field distribution at the image plane can be explained by the superposition of the far-field scattered fields as follows:

$$\mathbf{E}_{\mathbf{scat}}(x, y, z) = A_0 \frac{j}{2\pi} \iint\limits_{\sqrt{k_x^2+k_y^2} \leq k_{NA}} \frac{1}{k_z} \mathbf{E}_{\mathbf{scat},\infty}\left(\frac{k_x}{k}, \frac{k_y}{k}\right) e^{j(k_x x + k_y y \pm k z_z)}\, dk_x\, dk_y \tag{5.4}$$

where A_0 is scaling factor associated with the far-field calculations at the infinity, $k = \lambda/2\pi$ is the wavevector, and $k_z = \sqrt{k^2 - k_x^2 - k_y^2}$ is the wavevector along the optical axis z. The integral limits impose filtering pupil function defined by objective NA. Therefore, the scattered radiation profile has of great importance for contrast calculations. The image field intensity is then calculated at the camera plane. To incorporate the photothermal effect into the model, the same steps are iterated after updating the particle size and refractive index using the thermo-optic [Kasarova et al., 2010] and thermal-expansion coefficients [Mark et al., 2007] explained above. The simulation geometry is defined for a 500 PMMA bead ($n = 1.49$) placed on top of a silicon substrate ($n = 4.2$). We set the imaginary part of the silicon refractive index to zero since it is negligibly small compared with the real part at the illumination wavelength ($\lambda = 520$ nm). We assumed plane wave illumination from above. This is a valid approximation for the nearly collimated sample illumination in the experiments. To speed up the successive simulations, reflected Green's functions are pre-calculated and stored in the memory. The reference field image is similarly calculated using Fresnel's reflection coefficients and mapped into the image field. The final image becomes the intensity of the coherent sum of both image fields.

5.2.3 Temperature dependence of photothermal signal

The scattering signal is differentiable in the temperature domain. We can write the derivative of the scattered field E_{scat} as follows:

$$\lim_{\Delta T \to 0} \Delta T \frac{dE_{scat}(T)}{dT} = E_{scat}(T + \Delta T) - E_{scat}(T) \tag{5.5}$$

In our system, the infrared (IR) absorption induced the temperature change is less than 5 K for a 500 nm PMMA bead. Also, we numerically demonstrate that the scattered field modulation depth ($\Delta E/E$) for a 1 K temperature increase is about 10^{-4}. This modulation depth is determined by the sample's thermo-optic and thermal-expansion coefficients. Applying the chain rule on equation 5.5, the modulation depth

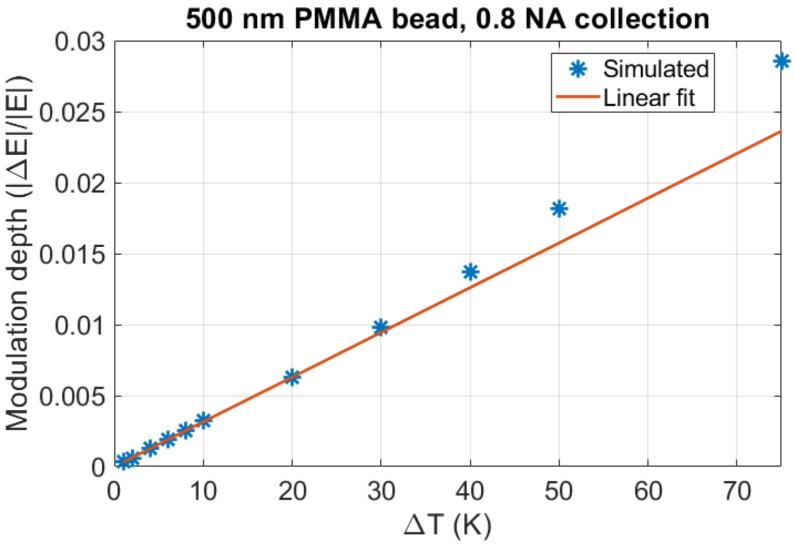

Figure 5·3: Simulated temperature dependence of photothermal signal for 500 nm PMMA bead. Simulation parameteres are the same in Figure 5·2

for $|\Delta E| \ll |E|$ can be written in a linear form,

$$\frac{\Delta E}{E} = \Delta T \frac{dE_{scat}(T)}{dT} = \Delta T \left[\frac{\partial E_{scat}(r,n)}{\partial r}\frac{dr}{dT} + \frac{\partial E_{scat}(r,n)}{\partial n}\frac{dn}{dT} \right] \tag{5.6}$$

Together, our assumption in equation 5.6 holds for small temperature changes owing to the sample's linear temperature response and very small thermal coefficients in the -4 orders of magnitude at the room temperature [Mark et al., 2007]. The simulated photothermal response curve as a function of ΔT is shown in Figure 5·3. We point out that this linearity breaks at the large temperature changes of $\Delta T >$30 K. This stems from the fact that the photothermal effect induces a strong change in the scattered field which scales with the third power of the particle's size. That is to say, the modulation depth should be within the range of 0.01 for the assumption of the scattered field's linear temperature dependence. Otherwise, the modulation depth dependent temperature change calculations can be performed by polynomial curve fitting to the theoretical findings.

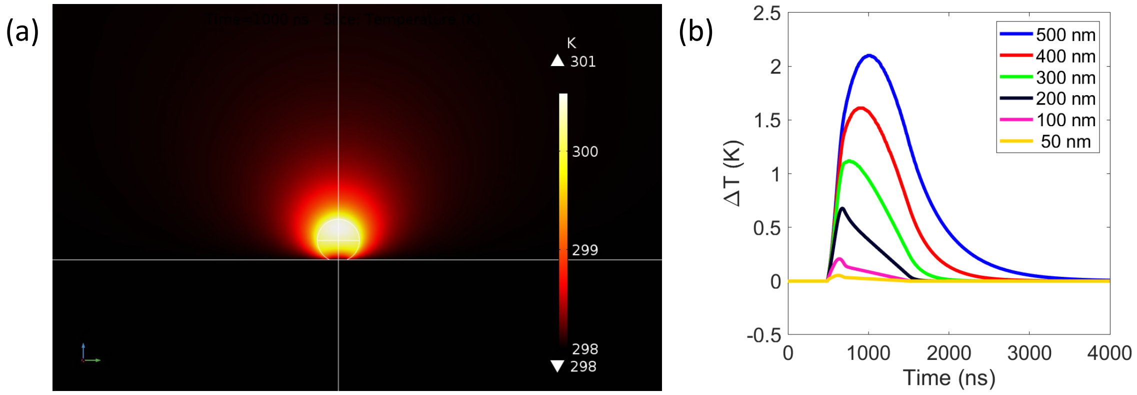

Figure 5·4: (a) Temperature distribution when a 500 nm PMMA bead is heated by the IR pulse. The time is at 500 ns after the rising edge of the IR pulse. (b) Temperature rising for different sizes of PMMA beads.

5.2.4 Photothermal effect COMSOL simulations

The analytical model introduced discussed can be used to calculate the photothermal image formation of a specific sample with known size and refractive index. To investigate the photothermal process, the size and refractive index of both "hot" and "cold" states need to be known. With the known thermo-optic ($\frac{dn}{dT}$) and thermal-expansion ($\frac{dr}{dT}$) coefficients, the temperature of "hot" and "cold" states need to be solved. The transient temperature profile for a particle placed on a silicon substrate is simulated in COMSOL Multiphysics. We performed the simulations in two steps. First, we numerically evaluate the absorbed mid-infrared power P_{abs} by a 500 nm PMMA particle. The total absorbed power is related to the mid-infrared beam intensity I and the absorption cross-section σ_{abs}, $P_{abs} = \sigma_{abs} \cdot I$. Using the particle's optical parameters including the size and dielectric constant, the absorption cross-section is calculated in the electromagnetic wave, frequency domain module. The mid-infrared beam intensity at the center of the IR focus is input from the experimentally measured power and beam size. The experimental details are explained in the results section.

In the second step, we calculate the transient temperature rise using the COMSOL's heat transfer in the solids module which takes the pre-calculated absorbed power as an input from the initial step. To do so, we define the geometry in which the bead sits on top of the substrate. The bead is treated as a uniform heat source, which is reasonable as a result of the roughly uniform absorbed power distribution from the simulation result in the first step. The thermal diffusion process is calculated as the following equations:

$$\rho C_p \frac{\partial T}{\partial t} + \nabla \cdot \mathbf{q} = Q \tag{5.7}$$

$$\mathbf{q} = -k \nabla T \tag{5.8}$$

where ρ is the density of the material, C_p is the heat capacity at constant pressure, T is temperature, t is time, k is the thermal conductivity. The COMSOL's heat transfer in the solids module can numerically solve these equations and obtain the temperature distribution in the time and space domain of the full system.

The transient temperature response of the PMMA bead in the time domain can be obtained. The temperature is calculated from the temperature distribution by integrating the temperature of the whole volume of the PMMA bead and dividing by the volume. Figure 5·4b shows the transient temperature response from different size parameters ranging from 50 to 500 nm. These plots are calculated for the experimentally obtained pulse parameters used in Figure 5·4a. It is clearly seen that ΔT decreases with the size since the heat dissipation constant is much faster for smaller particles. Therefore, the small nanoparticles require a much shorter IR pulse width.

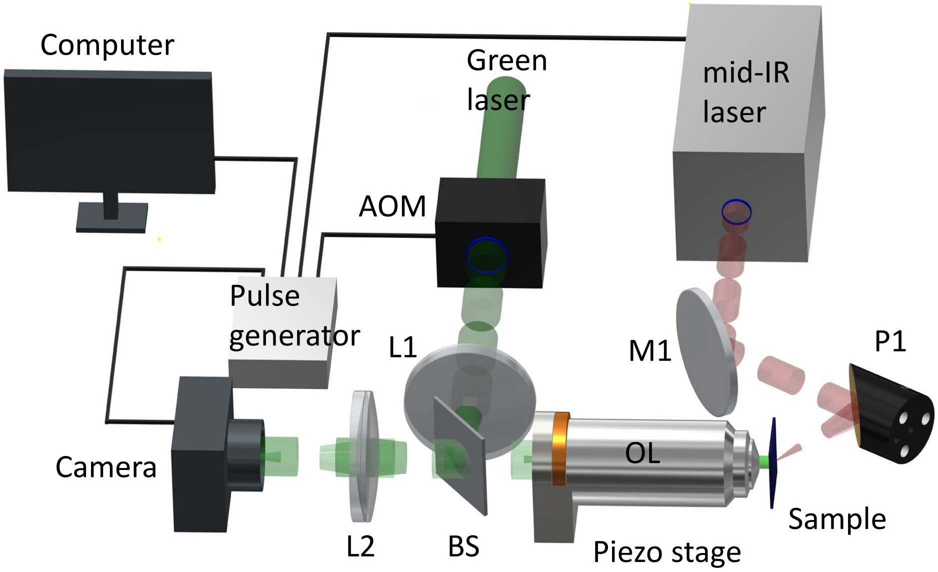

Figure 5·5: Schematic of wide-field interferometric mid-infrared photothermal microscopy. L1-L2: achromatic doublets; BS: beam-splitter; M1: gold mirror; P1: parabolic gold mirror; AOM: acousto-optic modulator; OL: objective lens.

5.3 Experimental considerations

5.3.1 Experimental setup

The schematic of our bond-selective interferometric scattering microscopy is illustrated in Figure 5·5. The green pump beam is frequency-doubled from a femtosecond (fs) laser (Chameleon, Coherent) operating at 80 MHz with 1040 nm wavelength and 100 fs pulse width by second-harmonic generation (SHG) process using a non-linear crystal. The resulted laser beam has a 520 nm central wavelength with a 9 nm bandwidth, reducing speckles in the images owing to its low temporal coherence length. Before the SHG, the fs beam is chopped by an acousto-optical modulator (AOM, R23110-0.5, Gooch and Housego) at 200 kHz with a 50% duty-cycle square waveform. To provide wide-field sample illumination, the green laser is focused on a microscope objective's (CFI TU Plan Fluor EPI 50×, NA 0.8, Nikon) back-pupil plane in Köhler illumination configuration using a field lens (L1) with a 75 mm focal length. This illuminates the sample of interest with a plane wave at an incident angle defined by its location at the objective back-pupil. The objective lens is mounted on an objective piezo scanner (MIPOS 100 SG RMS, Piezosystem Jena) to adjust the objective nominal focus and acquire defocus image scans. To hold the substrate stable in the vertical direction, the substrate is held by a custom-built vacuum chuck mounted on a tip/tilt kinematic mount. The sample is translated by a manual XYZ stage with differential adjusters (PT3A/M, Thorlabs). To achieve normal incidence on the sample, we ensure that the green laser is focused at the center of the back-pupil by adjusting the two tip/tilt mirrors before the field lens. The normal incidence realizes a radially symmetric point spread function (PSF) [Yurdakul et al., 2020]. We utilize this fact to fine-tune the mirrors by imaging spherical beads. The epi-illuminated sample is then imaged onto a 5.0 MP monochromatic area-scan CMOS camera (GS3-U3-51S5M-C, FLIR) through a tube lens (L2).

5.3.2 Backside IR illumination

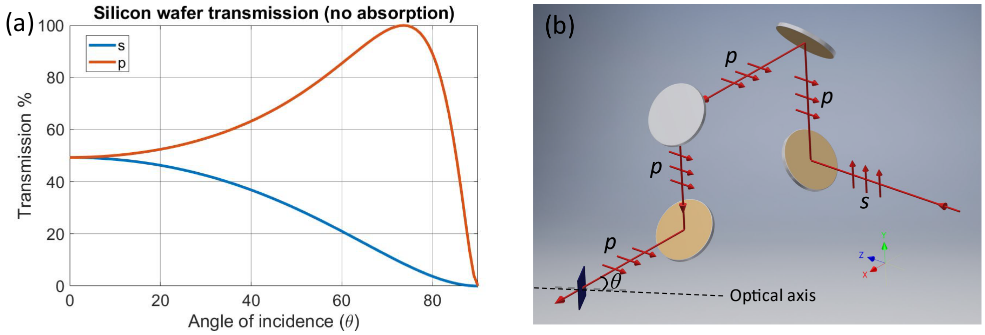

Figure 5·6: Back-side IR illumination optimization. (a) Calculated transmission of silicon substrate for polarized IR beam at various angle of incidence. Simulation parameters: $\tilde{\nu}_{illumination} = 1650\ cm^{-1}$, $n_{silicon} = 3.4$, $n_{medium} = 1$. The imaginary part of silicon refractive index is omitted in the transmission calculations. (b) Topological polarization rotation of IR light from s to p polarization state.

A pulsed mid-IR tunable quantum-cascaded laser (QCL, MIRcat, Daylight solutions) illuminates the substrate from the backside at an oblique angle of ∼61° which goes beyond the objective's acceptance angle of 53°. The collimated IR beam is focused on the substrate's front surface using a parabolic gold mirror (P1). There are two main reasons for using the oblique IR illumination: (1) it avoids the IR absorption by the objective lens which creates random signal fluctuations and (2) it can improve the IR transmission that enhances the photothermal signal. To increase the IR transmission in the silicon substrate, we utilized Brewster's angle in which *p*-polarized light reflection reduces to nearly zero. To do so, we topologically rotate the polarization state of the factory default IR from *s*-polarized to *p*-polarized as shown in Figure 5·6. We use two 45° gold mirrors in a periscope configuration but pointing each other at a 90° axial rotation such that the incident beam along the x-axis propagates at the y axis. The first mirror reflects the light upwards and upon this reflection the polarization state changes from *s* to *p*. The second mirror preserves its polarization state with respect to the optical axis of the substrate. The arrangement of the mirrors was placed accordingly to this design right after the IR laser output. The IR beam is incident at the angle of 61°. As shown in the transmission simulations, this oblique illumination provides 84% transmission for *p* polarization compared with 20% transmission in the initial *s* polarization state. The simulations are numerically calculated using Fresnel's reflection coefficients. The calculations omit the nitride layer since it has negligible absorption. Overall, the IR transmission is enhanced about four-fold compared to that of the initial *s*-polarized beam, providing higher IR power on the sample.

5.3.3 Camera-based photothermal signal detection mechanism

To measure the photothermal signal in the wide-field system, we employed the virtual lock-in camera detection reported in [Bai et al., 2019]. As shown in Figure 5·7a, while a pulse train of visible beam continuously illuminates the sample, the IR beam simultaneously illuminates the sample at every other camera frame. In other words, the IR beam is turned on and off at the subsequent frames. We refer the IR-on and IR-off frames to *"hot"* and *"cold"*, respectively. The photothermal image is then obtained by taking the difference image, subtracting the cold frames from the hot frames. The time delay t_d denotes the delay between individual IR and visible pulses. The camera, visible, and IR beams are synchronized by a pulse generator master clock which externally triggers each instrument. The pulse generator (9254-TZ50-US, Quantum composers) outputs three pulse waves with different duty cycles, pulse widths, and time delays. This allows for individually controlling the AOM, camera exposure, and mid-IR QCL. The AOM is triggered at 200 kHz with a 200 ns pulse width to obtain the 200 ns visible pulse train. The camera is triggered at 200 Hz using the duty cycle mode at 1 on and 999 off. To obtain the hot and cold frames, the mid-IR QCL laser is externally triggered at 200 kHz using duty cycle mode at 1000 on and 1000 off. The IR-pulse width is set to 1 µs using QCL's internal settings. The time delay t_d was set to $\sim$500 ns to maximize the photothermal signal. t_d is empirically determined by measuring the transient photothermal response via time-gated pump-probe approach [Zhang et al., 2019]. For the particle of interest, the photothermal signal peaks around the same delay. Therefore, we keep the delay constant unless otherwise noted.

The image acquisition and hardware, that is the piezo scanner and pulse generator, control is implemented on a custom-built Python. For acquisition, we use an open-source Python module named "PySpin" provided by the camera company. The camera captures the frames sequentially at each trigger pulse and transfers them to the computer via the universal serial port. Each image is self-normalized by the average intensity at a predetermined region of interest out of the IR spot. This min-

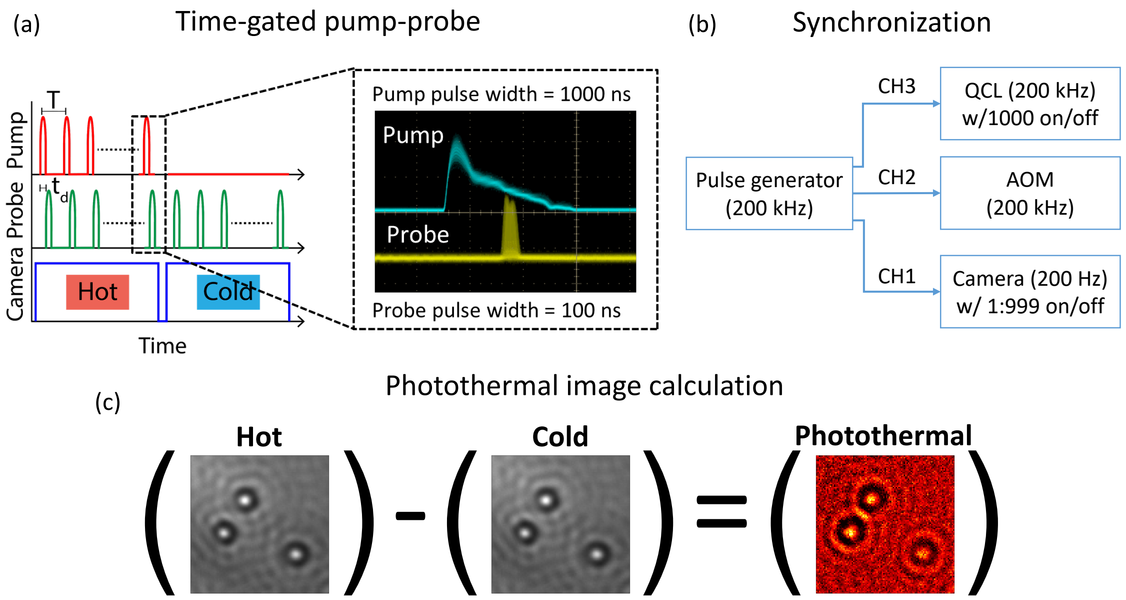
(a)
Time-gated pump-probe
T
Pump
t_d
Probe
Camera
Hot
Cold
Time
Pump pulse width = 1000 ns
Pump
Probe
Probe pulse width = 100 ns
(b)
Synchronization
Pulse generator (200 kHz)
CH3
QCL (200 kHz) w/1000 on/off
CH2
AOM (200 kHz)
CH1
Camera (200 Hz) w/ 1:999 on/off
(c)
Photothermal image calculation
Hot
Cold
Photothermal

Figure 5·7: (a) Virtual camera lock-in detection. The synchronization and timing are controlled by the pulse generator which externally triggers the pump, probe, and camera. T period of the IR and pump pulse which is set to 200 kHz. The camera frame rate is set to 200 Hz. The pump beam is modulated at 100 Hz such that odd frames are IR-on (Hot) and even frames are IR-off (Cold). Time delay t_d between the pump and probe beams are controlled for transient thermal response measurements and maximized photothermal signal. Zoom-in shows the pump and probe pulses monitored by an oscilloscope. (b) Block diagram of electronic connections for system control and signal detection. The pulse generator generates the master clock at 200 kHz and triggers the components at the aforementioned frequencies. (c) Experimental photothermal image calculation by subtracting the cold frame from the hot frame. The sample is 500 nm PMMA beads on the nitride substrate. The IR wavelength is tuned to the 1729 cm^{-1} vibrational peak of the C=H bond.

imizes the effect of the possible visible laser intensity fluctuations across the multiple frames. Even/odd-numbered frames are then temporally stored in the memory and directly averaged into a single 2D array at their corresponding data arrays as *"hot"* and *"cold"*, respectively. A large number of frame averaging is required to obtain high SNR that can distinguish the photothermal signal from the background noise. We typically acquire 10000 frames in total, that is, 5000 hot and 5000 cold. The frames are averaged in real-time. This computationally efficient image acquisition approach significantly reduces the memory and space requirement for a large number of frames ($O(N) \rightarrow O(1)$). In other words, only two averaged hot and cold images (a few MBs) are saved on the disk at the end of each photothermal image acquisition, instead of saving gigs of image data to average at the post-process. We note that all images can also be saved for the SNR characterization experiments.

5.4 System validation and characterization

5.4.1 IR spot visualization

To evaluate our system's performance, we first demonstrated the mid-IR absorption by a thin film of PMMA spin-coated on a silicon substrate. As shown in Figure 5·8, the IR focus on the substrate was elongated along the horizontal axis due to the oblique incident angle. This provided nearly 30 µm × 60 µm of FOV for the photothermal detection. The IR focus can be adjusted to a more circular spot by changing the parabolic mirror's position with respect to the substrate, but the defocused IR focus could reduce the IR intensity and thus the photothermal signal. For the sake of the proof-of-concept experiments with high-SNR, we kept the IR focus smaller. Note that, we cropped the rectangular image FOVs into squares to obtain symmetric data visualization throughout the manuscript.

5.4.2 Noise analysis

Our photothermal microscopy in practice can achieve shot-noise-limited sensitivity. The noise-floor in the interferometric signal is dominated by the photon shot noise [Taylor and Sandoghdar, 2019]. However, the wide-field laser illumination creates heterogeneous background across the FOV. The interferometric contrast from

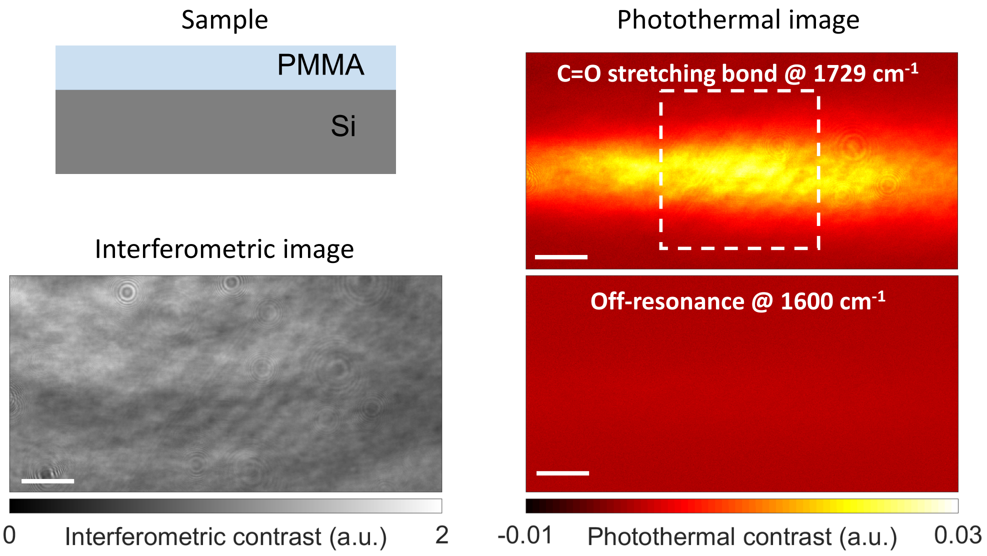
Sample
PMMA
Si
Photothermal image
C=O stretching bond @ 1729 cm-1
Interferometric image
Off-resonance @ 1600 cm-1
0
Interferometric contrast (a.u.)
2
-0.01
Photothermal contrast (a.u.)
0.03

Figure 5·8: Bond-selective interferometric imaging of PMMA thin-film on top of a silicon substrate. Interferometric MIP images at C=O stretching absorption peak of 1729 cm^{-1} and off-resonance wavenumber of 1600 cm^{-1} . The dashed square indicates the region of interest in the analyzed photothermal images. Photothermal image acquisition time: 10 s (1000 frames). IR power: 6.05 mW @ 1729 cm^{-1} and 5.73 mW @ 1600 cm^{-1}. Scale bar: 20 µm

nanoscale samples can be buried under such heterogeneity. Luckily, the photothermal detection is immune to those variations, providing nearly background-free images [Boyer et al., 2002]. The differential images only have the shot-noise contribution from the background signal. Although there exist contrast variations across the pixels, the shot-noise level variations become quite negligible owing to relatively small differences.

We experimentally evaluated the noise in our imaging system. We measured the noise in differential frames of the same FOV captured at a various number of collected photons (P). This minimized the background fluctuations due to the nonuniform laser illumination. Figure 5·9 shows our noise calculations in the logarithmic scale. The fitted curve as a function of P was $\alpha P^{0.498}$ with a constant scaling factor of α. The ex-

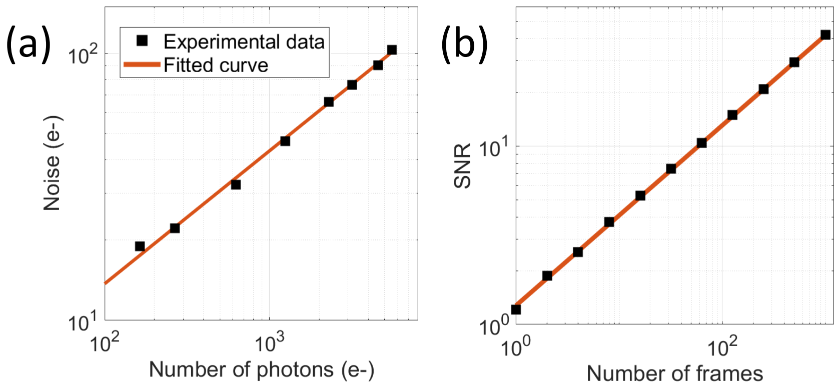

Figure 5·9: SNR analyis. (a) Calculated noise in a single photothermal image for different collected photons (P). The fitted curve ($\alpha P^{0.498}$) has a slope of 0.498 in logarithmic scale, indicating shot-noise-limited detection. The total number of electrons in a single pixel is nearly 10 ke-. (b) Photothermal SNR calculated for different number of frames (N) averaging. The fitted curve ($\alpha N^{0.505}$) has a slope of 0.505 in logarithmic scale, indicating random noise-source with minimal mechanical instability and fixed pattern artifacts.

ponent of the curve was very close to the theoretical value of 0.5. This indicated that our camera grants the shot-noise-limited detection for sufficiently saturated frames. The aforementioned modulation fraction was in the orders of the camera's shot-noise limited contrast which is defined by $1/\sqrt{\mathrm{P}}$. Frame averaging of shot-noise-limited images can reduce the noise floor by a factor of the square root of the number of frames N. Therefore, multiple difference images were averaged in practice to obtain the photothermal signal with good data fidelity. The PMMA film was a great example of SNR improvement upon frame averaging since a single photothermal frame had an SNR of 1.2. The SNR was calculated by dividing the maximum signal by the background standard deviation outside the IR spot. As shown in Figure 5·9, the experimental image SNR was consistent with the theoretical curve which scales with $\alpha N^{0.505}$. This indicated that the photothermal SNR can be greatly improved by frame averaging with minimal mechanical noise during the acquisition. Furthermore, SNR can be improved by using a large pixel-well-depth camera recently used in interferometry measurements [Schnell et al., 2020].

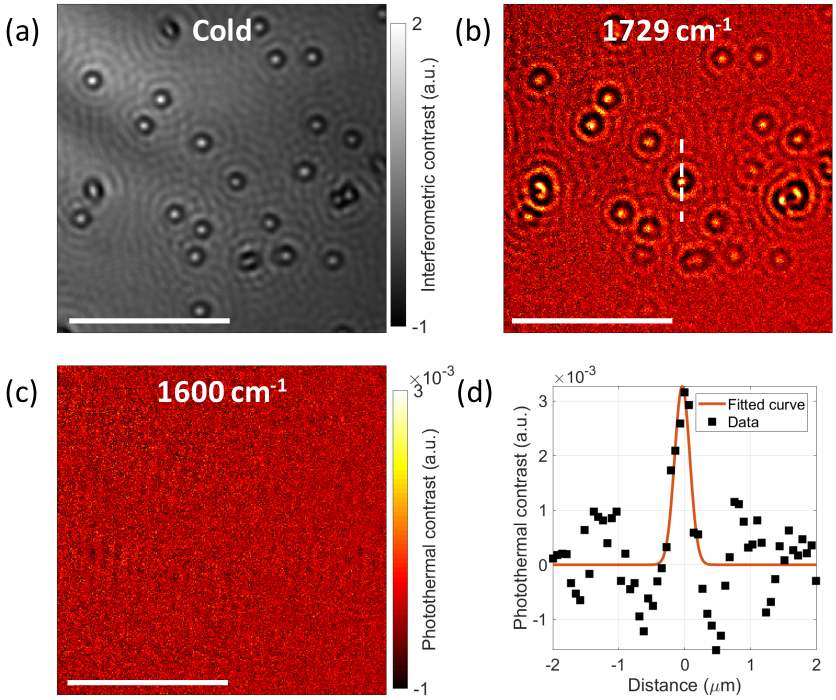

Figure 5·10: Bond-selective interferometric imaging of 500 nm PMMA beads. (a) Interferometric cold image. (b-c) Interferometric MIP images at C=O stretching absorption peak (1729 cm^{-1}) and off-resonance (1600 cm^{-1}), respectively. (d) Cross-section profile indicated by the white dashed line along the single bead in (b). The FWHM of the Gaussian fit is nearly 300 nm. The minimum and maximum points coincide at 500 nm separation ($\Delta_{feature} = 500$ nm). The beads in the interfaces appears to be Gaussian-shaped objects with ($\Delta_{bead} = 350$ nm), resulting in the deconvolved PSF with 357 nm FWHM ($\Delta_{PSF} = \sqrt{\Delta^2_{feature} - \Delta^2_{bead}} = 357$ nm). Photothermal image acquisition time: 50 s. IR power: 2 mW @ 1729 cm^{-1} and 3.8 mW @ 1600 cm^{-1}. Scale bars: 10 µm

5.4.3 Resolution analysis

Next, we perform proof-of-principle experiments on 500 nm PMMA nanospheres to demonstrate photothermal imaging of individual particles. The PMMA beads have a refractive index similar to biological nanoparticles, having similar particle polarizability for a given size (see equation 2.9). Therefore, the interferometric contrast from PMMA beads is very close to those from the same size viruses or bacteria. A 100 mm double side polished 100 nm low-pressure chemical vapor deposition (LPCVD) Nitride (Si_3N_4) on silicon (Si) wafer with 500 µm thickness (University Wafer) was first etched down to ∼70 nm. A photolithography process was then used for patterning the reference regions for easy focus finding, followed by dicing to 10 mm × 20 mm rectangular chips. Half of the substrate interfaces with the vacuum chuck, the remaining part is used for samples. A stock solution of 500 nm PMMA nanospheres (MMA500, Phosphorex) was diluted with deionized water by 1:10, followed by a spin coating on the nitride substrate. Figure 5·10a shows the interferometric image from a cropped FOV, showing nearly a contrast level of 2. To obtain chemical imaging of these beads, we target the carboxyl group around the C=O stretching absorption peak at 1729 cm^{-1}. This resonance photothermal image has an SNR of 9. When the IR wavelength is tuned to off-resonance at 1600 cm^{-1}, we observe no photothermal contrast. As we expected, the background heterogeneity due to the laser illumination is greatly reduced in the photothermal images. This shows consistency with the differential images obtained under interferometric scattering microscopy [Ortega Arroyo et al., 2014]. Furthermore, our photothermal measurements can achieve diffraction-limited lateral resolution in the visible spectrum (see Figure 5·10d). According to Rayleigh's resolution definition, the first minimum of the cross-section profile across the 500 nm beads coincides with the peak value around 500 nm. Under Gaussian object [Yilmaz et al., 2015] approximation, the deconvolved PSF is 357 nm which is close to $\lambda/2NA$.

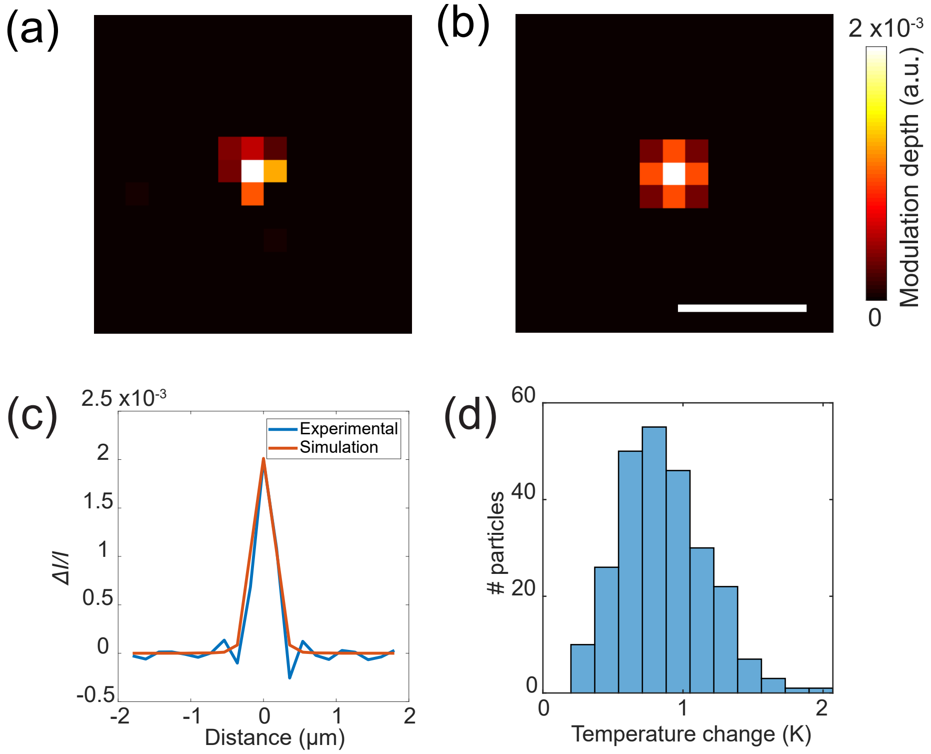

Figure 5·11: Experimental validation of photothermal image formation modeling. (a) Experimental and (b) simulated photothermal image of a 500 nm PMMA bead at 1729 cm^{-1}. (c) Modulation depth ($\Delta I/I$) cross-section profiles in (a-b). (d) Temperature change (ΔT) histogram of the detected 500 nm PMMA beads. The temperature change is calculated at each bead's peak contrast using the linear relationship with the modulation depth. Scale bar: 1 µm.

5.4.4 Validation of theoretical calculations

This experimental validation data is obtained in a dark-field version of our setup since it can achieve better SNR for a given particle size. The probe part of this setup is conceptually the same as in the previously discussed 4f setup in [Avci et al., 2017a]. This setup blocks 99.9% of the reflected light at the conjugate plane of the objective back focal plane. The image formulation framework detailed above was verified in two steps using the experimental photothermal image of a 500 nm PMMA bead. We first calculate the modulation depth from the BEM simulation

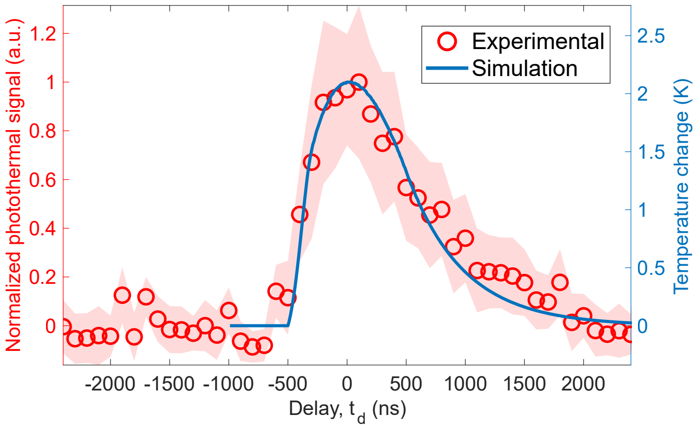

Figure 5·12: Transient temperature response analysis. Experimental and simulated transient temperature response for 56 particles. The temperature decay time constant is 915 ns.

using the PMMA's optical and thermal coefficients at $\Delta T = 1\ K$. Since the modulation depth can be linearly related to the small temperature changes ΔT (see Figure 5·3), ΔT of the PMMA beads can be obtained backward from the experimental results. The experimental photothermal modulation depth image of a 500 nm PMMA bead on the silicon substrate is shown in Figure 5·11. The modulation depth was calculated as the ratio between photothermal image and peak contrast value at the cold state. Figure 5·11b is a simulation photothermal modulation depth image which is scaled to the same maximum value in Figure 5·11a. The cross-section profiles in Figure 5·11c show consistency between the experimental and simulated results. We then calculated the ΔT histogram for PMMA beads as shown in Figure 5·11d. The maximum temperature rising across the FOV was calculated as nearly 2 K which is consistent with the COMSOL simulations.

The simulated temperature rising and the experimental photothermal signal versus delay scan of 56 individual PMMA beads with a 500 nm diameter is shown in Figure 5·12. For each specific delay value, the photothermal signal is proportional to the integrated temperature change within the time window of the probe pulse, which

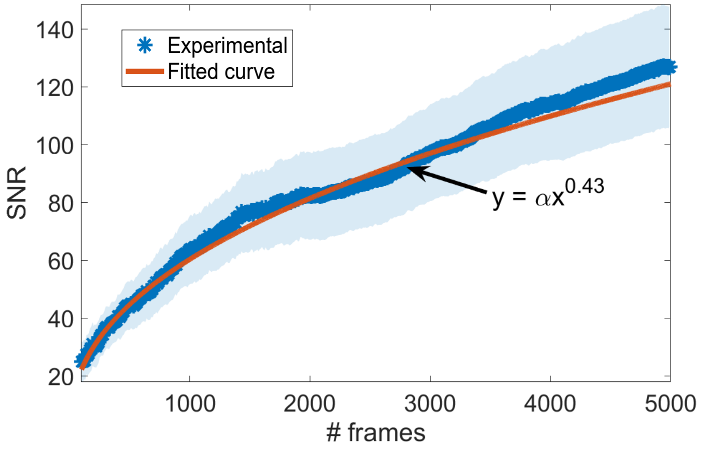

Figure 5·13: Photohermal signal stability in frame averaging. The phothothermal SNR of 500 nm PMMA beads calculated at different number of frames averaging. The experimental data is fit to an exponential function $y = \alpha x^n$ with n = 0.43. IR power: 6 mW @ 1729 cm^{-1}.

has a 200 ns pulse width as introduced in the previous section. In other words, the curve shape of the experimental delay scan is a convolution of the simulated temperature curve with the 200 ns probe pulse. Figure 5·12 shows that the experimental delay scan curve is not distorted too much compared to the simulation, which means the 200 ns pulse width is short enough to probe the highest temperature change. We point out that the transient response curves depend on sample size and IR pulse shape. Considering the pulse shape and particle size in this study, the time delay is carefully determined to obtain the maximum photothermal signal during the experiments. The photothermal images are then acquired using the optimized delay scan value that corresponds to the highest photothermal signal.

5.4.5 Mechanical stability in acquisitions

Figure 5·13 further shows the noise analysis of 56 PMMA beads over a different number of frames averaging N. The noise is calculated as the standard deviation of the photothermal image background nearby the particles. The exponential fit to the

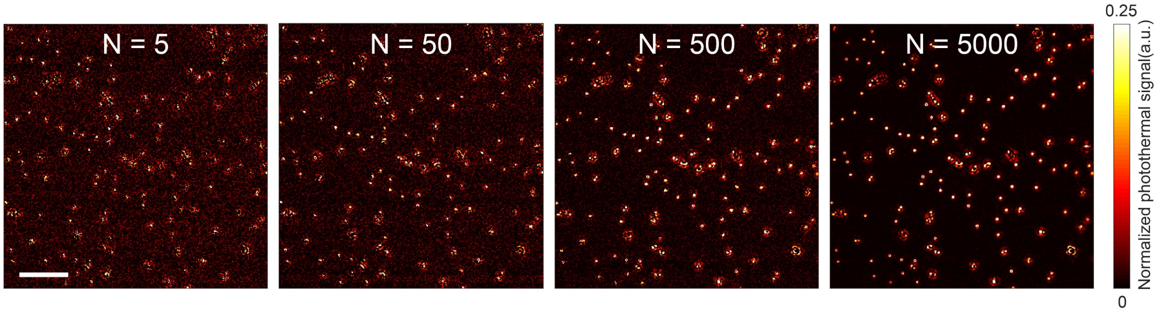

Figure 5·14: Photothermal signal of 500 nm PMMA beads at different number (N) of averaged frames. $P_{pump} =$, $\tilde{\nu}_{pump} = 1729\ cm^{-1}$ vibrational peak of the C=H bond, camera FPS: 400 Hz, scale bar: 10 μm.

experimental SNR values was found to be $SNR \propto N^{0.43}$. The slight variation from the theoretical value of 0.5 could be attributed to the mechanical noise in the imaging system. The photothermal image results at different frame averaging have been also shown in Figure 5·14.

5.5 Biological experiments

5.5.1 Bacteria and Fungi sample preparation

We used two strains of bacteria *S. aureus* ATCC 6538 and *E. coli* BW 25113 in this study. These strains were obtained from the American Type Culture Collection (ATCC) and the Biodefense and Emerging Infections Research Resources Repository (BEI Resources), respectively. To prepare bacteria samples for chemical imaging, bacterial strains were first cultured in cation-adjusted Mueller-Hinton Broth (Thermo Fisher Scientific) media and grown to the logarithmic phase. 1 mL of bacteria sample was centrifuged, washed twice with purified water, and then fixed by a 10% (w/v) formalin solution (Thermo Fisher Scientific). To load the bacteria sample, 2 µL of either *S. aureus* or *E. coli* bacteria solution was incubated on the substrate at room temperature until the surface dried.

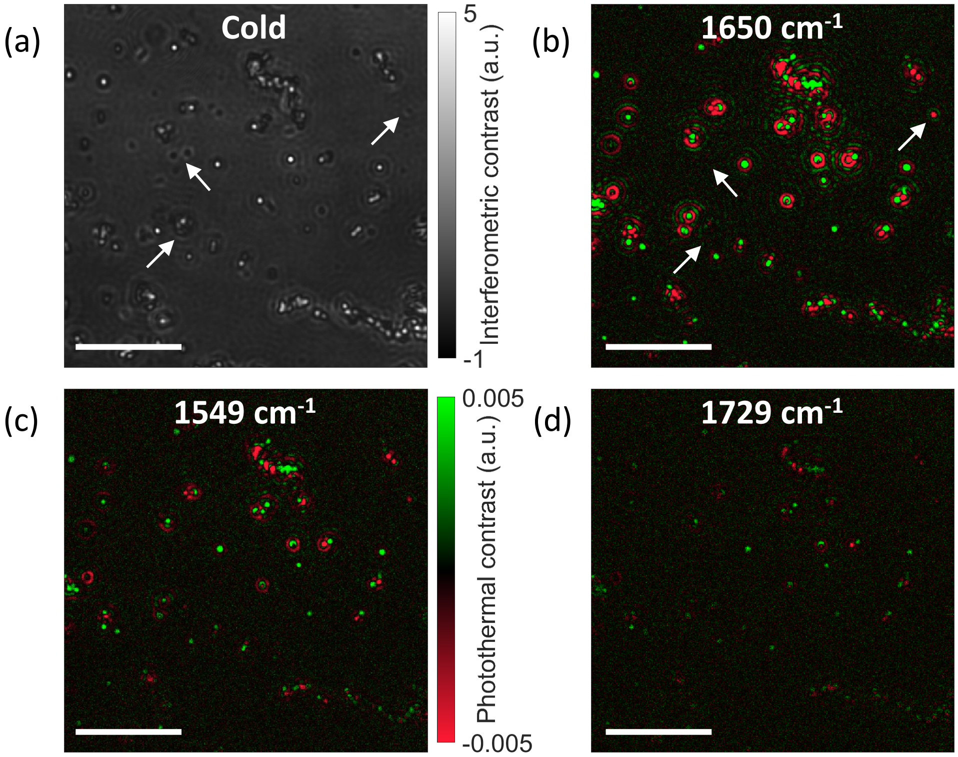

Figure 5·15: Bond-selective interferometric imaging of *S. aureus* bacteria. (a) Interferometric cold image. (b-d) Multi-spectral MIP images at discrete wavenumbers; (b-c) Amide I (1650 cm^{-1}) and II (1549 cm^{-1}) bands, and (d) C=O bond (1729 cm^{-1}). The left two arrows in DC image (a) indicates sample like features which disappear in MIP images. The upper right arrow indicates that the negative interferometric contrast from *S. aureus* due to its size appears to be negative in the MIP images. IR powers: 12.4 mW @ 1650 cm^{-1}, 9 mW @ 1549 cm^{-1}, and 6.05 mW @ 1729 cm^{-1}. Photothermal image acquisition time: 50 s (5000 frames). Scale bars: 10 µm

5.5.2 Bond-selective bacteria imaging

To demonstrate bond-selective interferometric imaging of single biological nanoparticles, we study bacteria and fungi as testing models. Figure 5·15 shows hyperspectral imaging of spherical *S. aureus* bacteria directly immobilized on the substrate. The interferometric image clearly shows their size variation across the FOV, since the contrast is related to the particle's size. To target major protein absorption peak in

Amide I band, the IR wavelength is tuned to 1650 cm^{-1}. The obtained photothermal image has a strong photothermal contrast with an SNR of about 60, indicating the rich protein content in *S. aureus* cells. Furthermore, Amide II band at 1549 cm^{-1} and off-resonance C=O stretching bond at 1729 cm^{-1} show the distinctive spectroscopic imaging at the same FOV. The weak-contrast at off-resonance wavelength comes from the residual IR absorption in the vibrational fingerprint region [Li et al., 2019]. Owing to the chemical specificity, photothermal detection is immune to the scattered signal from the unspecific immobilized particles. The interferometric particle signal indicated by the left arrow in Figure 5·15 disappears in the photothermal images, showing no contrast. The dark contrast particles (see e.g., the middle arrow), seems to be associated with unwanted signals based on the one-to-one comparison. However, the dark contrast particle indicated by the right arrow has photothermal contrast. This result further emphasizes the chemical specificity of our technique which was inaccessible in the conventional interferometric microscopy. We also point out that the photothermal contrast could be a positive or negative sign. This stems from the fact that thermo-optic and thermal expansion counteract each other. Their overall effect on the photothermal signal strongly depends on the particle's size [Li et al., 2017]. Either one could be dominant or cancel each other. Thus, some materials of a certain size could be invisible in this technique.

Next, we image rod-shape *E. coli* bacteria in the fingerprint region as shown in Figure 5·16. Similar to the *S. aureus* cells, the hyperspectral images are acquired at Amide I (1650 cm^{-1}) and II (1549 cm^{-1}) bands and C=O stretching bond (1729 cm^{-1}). The Amide I band shows the strongest photothermal signal with an SNR of about 22, which is three-fold less than the *S. aureus* cells. Nevertheless, *E. coli* photothermal images also exhibit distinctive signal levels at the Amide II band and C=O bond. The C=O bond has a much weaker photothermal contrast. We also observe that one

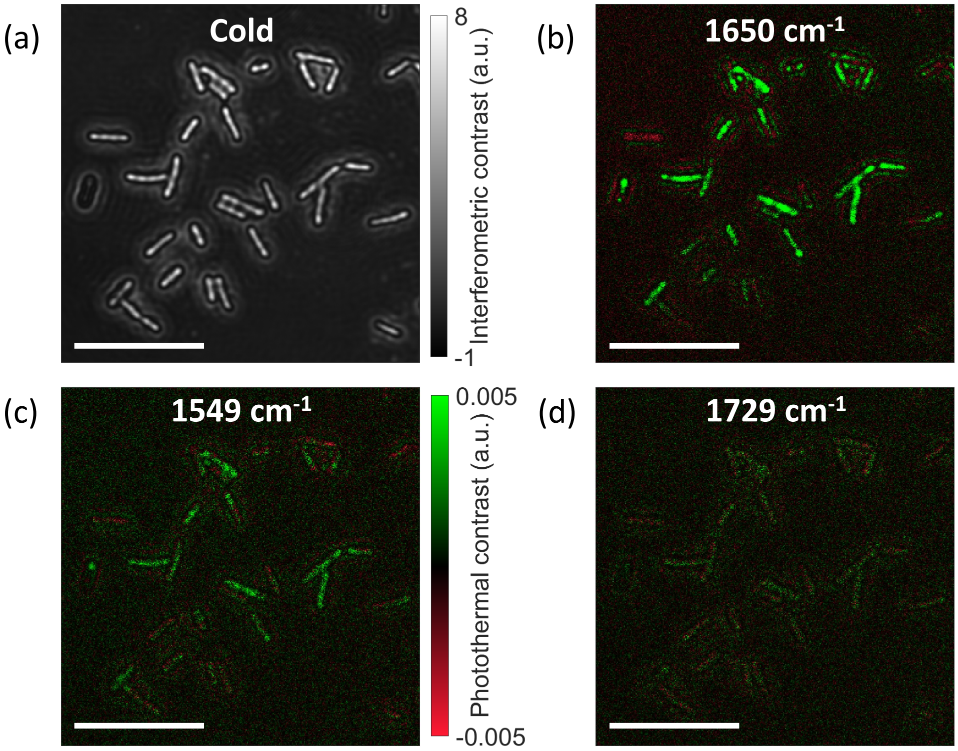

Figure 5·16: Bond-selective interferometric imaging of *E. coli* bacteria. (a) Interferometric cold image. (b-d) Multi-spectral MIP images at discrete wavenumbers; (b-c) Amide I (1650 cm^{-1}) and II (1549 cm^{-1}) bands, and (d) C=O bond (1729 cm^{-1}). IR powers: 12.4 mW @ 1650 cm^{-1}, 9 mW @ 1549 cm^{-1}, and 6.05 mW @ 1729 cm^{-1}. Photothermal image acquisition time: 50 s (5000 frames). Scale bars: 10 µm

of the *E. coli* cells have negative photothermal contrast although its interferometric image contrast is positive. Interestingly, another *E. coli* with negative interferometric contrast has positive photothermal contrast. These results indicate that photothermal signal signs of the same type of particles could vary even for similar interferometric contrast levels due to the difference in their size and shape. Together, these two distinctive bacteria results show the promise of this bond-selective interferometric scattering microscopy for high-throughput and multiplex differentiation of diverse bacteria populations.

5.5.3 Bond-selective fungi imaging

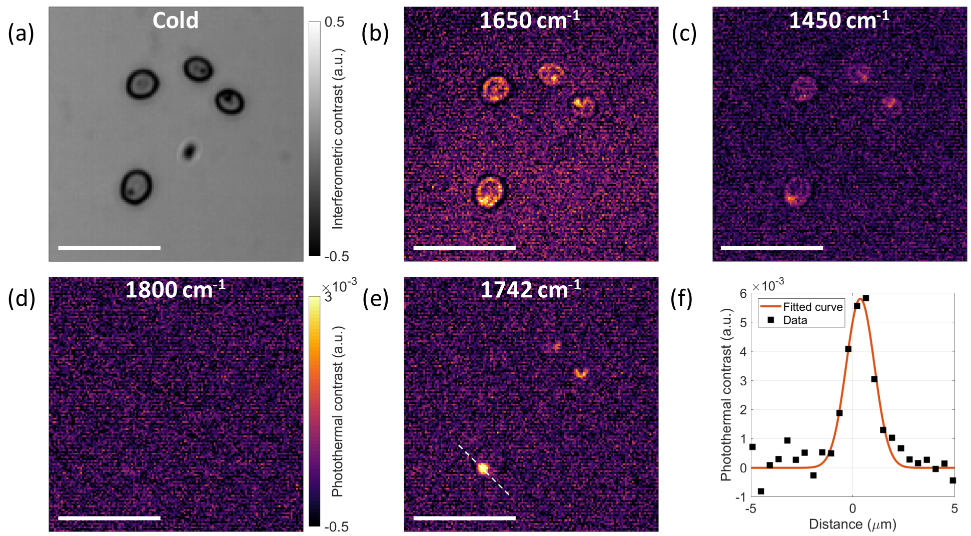
(a)
Cold
0.5
Interferometric contrast (a.u.)
-0.5
(b)
1650 cm-1
(c)
1450 cm-1
(d)
1800 cm-1
×10-3
3
Photothermal contrast (a.u.)
-0.5
(e)
1742 cm-1
(f)
×10-3
Fitted curve
Data
Photothermal contrast (a.u.)
6
5
4
3
2
1
0
-1
-5
0
5
Distance (μm)

Figure 5·17: Bond-selective interferometric imaging of *C. albicans.* (a) Interferometric cold image of *C. albicans.* (b-d) Multi-spectral MIP images at discrete wavenumbers; (b) protein Amide I band (1650 cm^{-1}), (c) CH$_2$ bending (1450 cm^{-1}) in lipid and protein bonds, (d) off-resonance (1800 cm^{-1}), and (e) C=O stretching (1742 cm^{-1}) in phospholipid esters. (f) Cross-section profile indicated by the white dashed line along the lipid droplet in (e). The FWHM of the Gaussian fit is 1.64 µm. IR powers: 11.35 mW @ 1650 cm^{-1}, 11 mW @ 1450 cm^{-1}, 8.7 mW @ 1800 cm^{-1}, 12.9 mW @ 1742 cm^{-1}. Photothermal image acquisition time: 20 s (1000 frames). Scale bar: 20 µm

We further investigate the capability of our technique on micron-scale single cells. We image *C. albicans* fungi which have oval morphology. Since these cells are several microns in diameter larger than diffraction-limited resolution, the temporal coherence of the laser source hinders visualizing inside the cells due to the speckle noise. To address this limitation, we replace the green laser illumination with a partially coherent blue light-emitting diode (LED). This greatly reduces the speckle noise as shown in Figure 5·17. The LED illumination is achieved in Köhler configuration which provides source-free and highly uniform sample illumination. We note that the frame rate in this experiments is set to 1250 frame/s using a fast CMOS camera (IL5, Fastec Imaging). To measure the protein distribution inside the cells, we tune the IR wavelength to 1650 cm^{-1} at Amide I band and 1450 cm^{-1} at the Amide III band. The strong signal from protein bonds is obtained whereas the off-resonance image at 1800 cm^{-1} shows no contrast. To avoid the lipid absorption peak, the off-resonance wavelength is set to 1800 cm^{-1} in contrast to bacteria samples. Furthermore, we target the phospholipid ester band at 1742 cm^{-1} to visualize the lipid droplet inside the fungi cells. The photothermal image reveals a micron-scale lipid droplet in one of the cells. The Gaussian fit to the lipid droplet indicated by the dashed line has an FWMH of 1.64 µm. Our findings show great promise for the understanding of such subcellular organelles with high chemical specificity.

5.6 Conclusion

In summary, we introduced the bond-selective interferometric scattering microscopy that enables fingerprinting individual nanoparticles captured on the layered substrate. We utilize 70 nm Si_3N_4/Si substrate to increase interferometric contrast by reducing the reference background. The analytical framework of the interferometric photothermal signal mechanism is formulated and a direct relation between the interferometric contrast and the photothermal signal has been presented. We demonstrate proof-of-principle biological experiments on *S. aureus*, *E. coli* and *C. albicans.* Our technique provides high-throughput molecular information beyond affinity-specific molecular specificity without any labeling. Moreover, this direct chemical imaging method could open up exciting possibilities for functional bio-nanoparticle analysis. Overall, our refined bond-selective interferometric microscopy has a great promise for high-resolution and high-throughput spectroscopic imaging of a broad size range of biological nanoparticles without any labeling.

Chapter 6

Conclusions

6.1 Summary

In this thesis, we introduce new theoretical and experimental concepts in single-particle interferometric reflectance (SPIR) microscopy. We discuss the analytical model of the common-path interferometric signal that underlines our physical understanding of the contrast mechanism in the presented approaches. The experimental realizations include careful discussions on the trade-off considerations in implementation and instrumentation. We show remarkable advancements in the imaging system's sensitivity, resolution, and chemical specificity. We establish the vectorial-optics-based linear forward model in common-path interferometric detection, relating the sample's polarizability with intensity images. We develop computational imaging methods using this forward model to expand the capability of conventional SPIR microscopy to previously unreached levels that can achieve an exceptional lateral resolution of 150 nm and sensitivity down to a single 25 nm low-index dielectric nanoparticle. Lastly, we introduce bond-selective SPIR microscopy that enables spectroscopic imaging in the vibrational fingerprint region by utilizing the mid-infrared induced photothermal effect. As a versatile microscopy platform, SPIR has a great promise for high-resolution and multiplexed accurate visualization and chemical characterization of a broad size range of individual biological nanoparticles with its high sensitivity. The simplicity of our technique would allow other researchers to implement SPIR with relatively minor modifications to their existing light microscopy, thus, enabling broad impact. We expect that SPIR microscopy has the potential of providing a simple, easy-to-use, and low-cost alternative for single nanoparticle detection and characterization beyond the classical limits of ordinary light microscopy.

6.2 Future Research Directions

6.2.1 Label-free nanoscopy in common-path interferometric microscopy

We demonstrated 150 nm lateral resolution in the computational asymmetric illumination SPIR microscopy project. In the future direction of this project, we speculate that a path forward exists for improving the resolution down to 100 nm. The source function could be optimized for higher SPIR contrast, and high-NA objectives with a shorter wavelength light source could be utilized. Moreover, since the PSF model is vectorial, *i.e.*, it includes the polarization of fields, we speculate that a further enhancement for both contrast and resolution can be achieved by using polarization diversity. Similarly, polarization could also allow for better localization of rod-shaped metallic nanoparticles such as gold and silver. Especially, elongated nanoparticles show strong signal dependency with respect to the angle between the polarization axis and the particle's long axis.

The most practical add-on would perhaps be through automation of the imaging/acquisition system. In the current project, the images were acquired by manually rotating the illumination mask introducing a considerable delay between consecutive images hence limiting the temporal resolution. Therefore, fully-automated control of illumination configuration, for example using a spatial light modulator or galvo scanner in the illumination path, would enable dynamic measurements with a significant increase in spatiotemporal resolution. Such devices would also allow for the implementation of complex source functions including scanning individual or multiplexed low-NA illuminations across the back-pupil.

Lastly, the linear forward model can incorporate coupled dipole method that considers multiple scattering [Chaumet et al., 2004]. This could potentially improve the accuracy of light scattering description. Reconstructions can be extended to quantify 3D complex permittivity functions. Particularly, prior sample information such as dielectric coefficients could be utilized in iterative reconstruction algorithms to retrieve complex dielectric structures at a nanoscale resolution far beyond the diffraction limit [Zhang et al., 2016b]. In addition, complex iterative reconstruction algorithms and physics-based learning approaches could be incorporated to enhance the reconstruction quality and resolution.

6.2.2 Mid-infrared photohermal nano-imaging/sensing

The bond selective interferometric microscopy's scope was currently limited to wavelength scale (~ 500 nm) nanoparticles due to the availability of the laser sources and camera. Photothermal imaging of sub-100 nm particles requires a much shorter pump and probe pulses less than 100 ns as a consequence of the direct relationship between heat dissipation and particle size. By employing such light sources, interferometric mid-IR photothermal microscopy can achieve chemical sensitivity levels within the reach of the existing interferometric techniques. This will require special design and instrumentation care due to the temporal and spatial coherence of the laser source. To overcome this problem, the adaptive mirrors, rotating diffusers, and AOM could be coupled into the system. Furthermore, the weak photothermal signal can be significantly improved by pupil-engineering in both illumination and collection paths. Lastly, a linear forward model of the system can be formulated from the analytical theory established in this dissertation. This would significantly improve the sensitivity and resolution beyond the reach of any other previously reported MIP techniques in the literature. Together, chemical optical nanoscopy in the vibrational fingerprint region could be realized on individual biological nanoparticles including viruses.

References

Arroyo, J. O., Cole, D., and Kukura, P. (2016). Interferometric scattering microscopy and its combination with single-molecule fluorescence imaging. *Nature protocols*, 11(4):617–633.

Avci, O., Adato, R., Ozkumur, A. Y., and Ünlü, M. S. (2016). Physical modeling of interference enhanced imaging and characterization of single nanoparticles. *Optics Express*, 24(6):6094–6114.

Avci, O., Campana, M. I., Yurdakul, C., and Ünlü, M. S. (2017a). Pupil function engineering for enhanced nanoparticle visibility in wide-field interferometric microscopy. *Optica*, 4(2):247–254.

Avci, O., Ünlü, N. L., Özkumur, A. Y., and Ünlü, M. S. (2015). Interferometric reflectance imaging sensor (iris)—a platform technology for multiplexed diagnostics and digital detection. *Sensors*, 15(7):17649–17665.

Avci, O., Yurdakul, C., and Ünlü, M. S. (2017b). Nanoparticle classification in wide-field interferometric microscopy by supervised learning from model. *Applied Optics*, 56(15):4238–4242.

Aygun, U., Urey, H., and Yalcin Ozkumur, A. (2019). Label-free detection of nanoparticles using depth scanning correlation interferometric microscopy. *Scientific Reports*, 9(1):9012.

Bai, Y., Zhang, D., Lan, L., Huang, Y., Maize, K., Shakouri, A., and Cheng, J.-X. (2019). Ultrafast chemical imaging by widefield photothermal sensing of infrared absorption. *Science Advances*, 5(7).

Baker, M. J., Trevisan, J., Bassan, P., Bhargava, R., Butler, H. J., Dorling, K. M., Fielden, P. R., Fogarty, S. W., Fullwood, N. J., Heys, K. A., et al. (2014). Using fourier transform IR spectroscopy to analyze biological materials. *Nature protocols*, 9(8):1771.

Beniac, D. R., Melito, P. L., deVarennes, S. L., Hiebert, S. L., Rabb, M. J., Lamboo, L. L., Jones, S. M., and Booth, T. F. (2012). The organisation of ebola virus reveals a capacity for extensive, modular polyploidy. *PLOS ONE*, 7(1):1–12.

Berciaud, S., Lasne, D., Blab, G. A., Cognet, L., and Lounis, B. (2006). Photothermal heterodyne imaging of individual metallic nanoparticles: Theory versus experiment. *Physical Review B*, 73:045424.

Bharat, T. A. M., Noda, T., Riches, J. D., Kraehling, V., Kolesnikova, L., Becker, S., Kawaoka, Y., and Briggs, J. A. G. (2012). Structural dissection of ebola virus and its assembly determinants using cryo-electron tomography. *Proceedings of the National Academy of Sciences*, 109(11):4275–4280.

Boyer, D., Tamarat, P., Maali, A., Lounis, B., and Orrit, M. (2002). Photothermal imaging of nanometer-sized metal particles among scatterers. *Science*, 297(5584):1160–1163.

Brandenburg, B. and Zhuang, X. (2007). Virus trafficking–learning from single-virus tracking. *Nature Reviews Microbiology*, 5(3):197–208.

Bruckman, M. A., Randolph, L. N., VanMeter, A., Hern, S., Shoffstall, A. J., Taurog, R. E., and Steinmetz, N. F. (2014). Biodistribution, pharmacokinetics, and blood compatibility of native and pegylated tobacco mosaic virus nano-rods and -spheres in mice. *Virology*, 449:163 – 173.

Campbell, P. J., Kyriakis, C. S., Marshall, N., Suppiah, S., Seladi-Schulman, J., Danzy, S., Lowen, A. C., and Steel, J. (2014). Residue 41 of the eurasian avian-like swine influenza a virus matrix protein modulates virion filament length and efficiency of contact transmission. *Journal of Virology*, 88(13):7569–7577.

Carter, E. P., Seymour, E. Ç., Scherr, S. M., Daaboul, G. G., Freedman, D. S., Selim Ünlü, M., and Connor, J. H. (2017). *Visualizing Ebolavirus Particles Using Single-Particle Interferometric Reflectance Imaging Sensor (SP-IRIS)*, pages 259–270. Springer, New York, NY.

Champion, J. A., Katare, Y. K., and Mitragotri, S. (2007). Making polymeric micro- and nanoparticles of complex shapes. *Proceedings of the National Academy of Sciences*, 104(29):11901–11904.

Chatterjee, R., Pavlovetc, I. M., Aleshire, K., Hartland, G. V., and Kuno, M. (2018). Subdiffraction infrared imaging of mixed cation perovskites: Probing local cation heterogeneities. *ACS Energy Letters*, 3(2):469–475.

Chaumet, P. C., Sentenac, A., and Rahmani, A. (2004). Coupled dipole method for scatterers with large permittivity. *Physical Review E*, 70(3):036606.

Chen, C. and Okayama, H. (1987). High-efficiency transformation of mammalian cells by plasmid dna. *Molecular and Cellular Biology*, 7(8):2745–2752.

Cheng, C.-Y. and Hsieh, C.-L. (2017). Background estimation and correction for high-precision localization microscopy. *ACS Photonics*, 4(7):1730–1739.

Cheng, C.-Y., Liao, Y.-H., and Hsieh, C.-L. (2019). High-speed imaging and tracking of very small single nanoparticles by contrast enhanced microscopy. *Nanoscale*, 11:568–577.

Cheng, J.-X. and Xie, X. S. (2015). Vibrational spectroscopic imaging of living systems: An emerging platform for biology and medicine. *Science*, 350(6264).

Chereddy, K. K., Vandermeulen, G., and Préat, V. (2016). Plga based drug delivery systems: Promising carriers for wound healing activity. *Wound Repair and Regeneration*, 24(2):223–236.

Cole, D., Young, G., Weigel, A., Sebesta, A., and Kukura, P. (2017). Label-free single-molecule imaging with numerical-aperture-shaped interferometric scattering microscopy. *ACS Photonics*, 4(2):211–216. PMID: 28255572.

Cooley, M., Sarode, A., Hoore, M., Fedosov, D. A., Mitragotri, S., and Gupta, A. S. (2018). Influence of particle size and shape on their margination and wall-adhesion: Implications in drug delivery vehicle design across nano-to-micro scale. *Nanoscale*, 10(32):15350–15364.

Cotte, Y., Toy, F., Jourdain, P., Pavillon, N., Boss, D., Magistretti, P., Marquet, P., and Depeursinge, C. (2013). Marker-free phase nanoscopy. *Nature Photonics*, 7(2):113–117.

Daaboul, G. G., Gagni, P., Benussi, L., Bettotti, P., Ciani, M., Cretich, M., Freedman, D. S., Ghidoni, R., Ozkumur, A. Y., Piotto, C., Prosperi, D., Santini, B., Ünlü, M. S., and Chiari, M. (2016). Digital detection of exosomes by interferometric imaging. *Scientific Reports*, 6(1):37246.

Daaboul, G. G., Lopez, C. A., Chinnala, J., Goldberg, B. B., Connor, J. H., and Unlu, M. S. (2014). Digital sensing and sizing of vesicular stomatitis virus pseudotypes in complex media: A model for ebola and marburg detection. *ACS Nano*, 8(6):6047–6055.

Daaboul, G. G., Yurt, A., Zhang, X., Hwang, G. M., Goldberg, B. B., and Ünlü, M. S. (2010). High-throughput detection and sizing of individual low-index nanoparticles and viruses for pathogen identification. *Nano Letters*, 10(11):4727–4731.

Dazzi, A., Prater, C. B., Hu, Q., Chase, D. B., Rabolt, J. F., and Marcott, C. (2012). AFM–IR: Combining atomic force microscopy and infrared spectroscopy for nanoscale chemical characterization. *Applied Spectroscopy*, 66(12):1365–1384. PMID: 23231899.

Dinarvand, R., Sepehri, N., Manoochehri, S., Rouhani, H., and Atyabi, F. (2011). Polylactide-co-glycolide nanoparticles for controlled delivery of anticancer agents. *International Journal of Nanomedicine*, 6:877.

Ekiz-Kanik, F., Sevenler, D. D., Ünlü, N. L., Chiari, M., and Ünlü, M. S. (01 Jul. 2017). Surface chemistry and morphology in single particle optical imaging. *Nanophotonics*, 6(4):713 – 730.

Enoki, S., Iino, R., Morone, N., Kaihatsu, K., Sakakihara, S., Kato, N., and Noji, H. (2012). Label-free single-particle imaging of the influenza virus by objective-type total internal reflection dark-field microscopy. *PLOS ONE*, 7(11):1–7.

Flint, S. J., Racaniello, V. R., Rall, G. F., Hatziioannou, T., and Skalka, A. M. (2020). *Principles of virology, Volume 2: pathogenesis and control*. John Wiley & Sons.

Freudiger, C. W., Min, W., Saar, B. G., Lu, S., Holtom, G. R., He, C., Tsai, J. C., Kang, J. X., and Xie, X. S. (2008). Label-free biomedical imaging with high sensitivity by stimulated raman scattering microscopy. *Science*, 322(5909):1857–1861.

Gaiduk, A., Yorulmaz, M., Ruijgrok, P., and Orrit, M. (2010). Room-temperature detection of a single molecule's absorption by photothermal contrast. *Science*, 330(6002):353–356.

Garbutt, M., Liebscher, R., Wahl-Jensen, V., Jones, S., Möller, P., Wagner, R., Volchkov, V., Klenk, H.-D., Feldmann, H., and Ströher, U. (2004). Properties of replication-competent vesicular stomatitis virus vectors expressing glycoproteins of filoviruses and arenaviruses. *Journal of Virology*, 78(10):5458–5465.

García de Abajo, F. J. and Howie, A. (2002). Retarded field calculation of electron energy loss in inhomogeneous dielectrics. *Physical Review B*, 65:115418.

Ge, P., Tsao, J., Schein, S., Green, T. J., Luo, M., and Zhou, Z. H. (2010). Cryo-em model of the bullet-shaped vesicular stomatitis virus. *Science*, 327(5966):689–693.

Geng, Y., Dalhaimer, P., Cai, S., Tsai, R., Tewari, M., Minko, T., and Discher, D. E. (2007). Shape effects of filaments *versus* spherical particles in flow and drug delivery. *Nature Nanotechnology*, 2(4):249–255.

Golightly, R. S., Doering, W. E., and Natan, M. J. (2009). Surface-enhanced raman spectroscopy and homeland security: A perfect match? *ACS Nano*, 3(10):2859–2869. PMID: 19856975.

Haeberlé, O., Belkebir, K., Giovaninni, H., and Sentenac, A. (2010). Tomographic diffractive microscopy: basics, techniques and perspectives. *Journal of Modern Optics*, 57(9):686–699.

Henao-Restrepo, A. M., Camacho, A., Longini, I. M., Watson, C. H., Edmunds, W. J., Egger, M., Carroll, M. W., Dean, N. E., Diatta, I., Doumbia, M., Draguez, B., Duraffour, S., Enwere, G., Grais, R., Gunther, S., Gsell, P.-S., Hossmann, S., Watle, S. V., Kondé, M. K., Kéïta, S., Kone, S., Kuisma, E., Levine, M. M., Mandal, S., Mauget, T., Norheim, G., Riveros, X., Soumah, A., Trelle, S., Vicari, A. S., Røttingen, J.-A., and Kieny, M.-P. (2017). Efficacy and effectiveness of an rvsv-vectored vaccine expressing ebola surface glycoprotein: Interim results from the guinea ring vaccination cluster-randomised trial. *The Lancet*, 389(10068):505–518.

Horio, T. and Hotani, H. (1986). Visualization of the dynamic instability of individual microtubules by dark-field microscopy. *Nature*, 321(6070):605–607.

Huang, Q., Li, N., Zhang, H., Che, C., Sun, F., Xiong, Y., Canady, T. D., and Cunningham, B. T. (2020). Critical review: digital resolution biomolecular sensing for diagnostics and life science research. *Lab on a Chip*, 20(16):2816–2840.

Huang, Y.-C., Chen, T.-H., Juo, J.-Y., Chu, S.-W., and Hsieh, C.-L. (2021). Quantitative imaging of single light-absorbing nanoparticles by widefield interferometric photothermal microscopy. *ACS Photonics*, 8(2):592–602.

Huang, Y.-F., Zhuo, G.-Y., Chou, C.-Y., Lin, C.-H., Chang, W., and Hsieh, C.-L. (2017). Coherent brightfield microscopy provides the spatiotemporal resolution to study early stage viral infection in live cells. *ACS Nano*, 11(3):2575–2585. PMID: 28067508.

Hulst, H. C. and van de Hulst, H. C. (1981). *Light scattering by small particles*. Courier Corporation.

Huth, F., Govyadinov, A., Amarie, S., Nuansing, W., Keilmann, F., and Hillenbrand, R. (2012). Nano-FTIR absorption spectroscopy of molecular fingerprints at 20 nm spatial resolution. *Nano Letters*, 12(8):3973–3978. PMID: 22703339.

Işil, Ç., Yorulmaz, M., Solmaz, B., Turhan, A. B., Yurdakul, C., Ünlü, S., Ozbay, E., and Koç, A. (2018). Resolution enhancement of wide-field interferometric microscopy by coupled deep autoencoders. *Applied Optics*, 57(10):2545–2552.

Jing, W., Wang, Y., Yang, Y., Wang, Y., Ma, G., Wang, S., and Tao, N. (2019). Time-resolved digital immunoassay for rapid and sensitive quantitation of procalcitonin with plasmonic imaging. *ACS Nano*, 13(8):8609–8617. PMID: 31276361.

Kairdolf, B. A., Qian, X., and Nie, S. (2017). Bioconjugated nanoparticles for biosensing, in vivo imaging, and medical diagnostics. *Analytical Chemistry*, 89(2):1015–1031. PMID: 28043119.

Kamaly, N., Xiao, Z., Valencia, P. M., Radovic-Moreno, A. F., and Farokhzad, O. C. (2012). Targeted polymeric therapeutic nanoparticles: design, development and clinical translation. *Chemical Society Reviews*, 41(7):2971–3010.

Kasarova, S. N., Sultanova, N. G., and Nikolov, I. D. (2010). Temperature dependence of refractive characteristics of optical plastics. *Journal of Physics: Conference Series*, 253:012028.

Klementieva, O., Sandt, C., Martinsson, I., Kansiz, M., Gouras, G. K., and Borondics, F. (2020). Super-resolution infrared imaging of polymorphic amyloid aggregates directly in neurons. *Advanced Science*, 7(6):1903004.

Levin, I. W. and Bhargava, R. (2005). Fourier transform infrared vibrational spectroscopic imaging: Integrating microscopy and molecular recognition. *Annual Review of Physical Chemistry*, 56(1):429–474. PMID: 15796707.

Li, X., Zhang, D., Bai, Y., Wang, W., Liang, J., and Cheng, J.-X. (2019). Fingerprinting a living cell by raman integrated mid-infrared photothermal microscopy. *Analytical Chemistry*, 91(16):10750–10756. PMID: 31313580.

Li, Z., Aleshire, K., Kuno, M., and Hartland, G. V. (2017). Super-resolution far-field infrared imaging by photothermal heterodyne imaging. *The Journal of Physical Chemistry B*, 121(37):8838–8846. PMID: 28741348.

Luan, X., Sansanaphongpricha, K., Myers, I., Chen, H., Yuan, H., and Sun, D. (2017). Engineering exosomes as refined biological nanoplatforms for drug delivery. *Acta Pharmacologica Sinica*, 38(6):754–763.

Mahamdeh, M., Simmert, S., Luchniak, A., Schaeffer, E., and Howard, J. (2018). Label-free high-speed wide-field imaging of single microtubules using interference reflection microscopy. *Journal of Microscopy*, 272(1):60–66.

Mark, J. E. et al. (2007). *Physical properties of polymers handbook*, volume 1076. Springer.

McLeod, E. and Ozcan, A. (2016). Unconventional methods of imaging: Computational microscopy and compact implementations. *Reports on Progress in Physics*, 79(7):076001.

Mir, M., Ahmed, N., and ur Rehman, A. (2017). Recent applications of plga based nanostructures in drug delivery. *Colloids and Surfaces B: Biointerfaces*, 159:217–231.

Nehls, J., Businger, R., Hoffmann, M., Brinkmann, C., Fehrenbacher, B., Schaller, M., Maurer, B., Schönfeld, C., Kramer, D., Hailfinger, S., Pöhlmann, S., and Schindler, M. (2019). Release of immunomodulatory ebola virus glycoprotein-containing microvesicles is suppressed by tetherin in a species-specific manner. *Cell Reports*, 26(7):1841 – 1853.e6.

Newell, D. G., Koopmans, M., Verhoef, L., Duizer, E., Aidara-Kane, A., Sprong, H., Opsteegh, M., Langelaar, M., Threfall, J., Scheutz, F., et al. (2010). Food-borne diseases—the challenges of 20 years ago still persist while new ones continue to emerge. *International journal of food microbiology*, 139:S3–S15.

Novotny, L. and Hecht, B. (2006). *Principles of Nano-Optics*. Cambridge University Press, Cambridge.

Ortega Arroyo, J., Andrecka, J., Spillane, K. M., Billington, N., Takagi, Y., Sellers, J. R., and Kukura, P. (2014). Label-free, all-optical detection, imaging, and tracking of a single protein. *Nano Letters*, 14(4):2065–2070.

Pagels, R. F. and Prud'homme, R. K. (2015). Polymeric nanoparticles and microparticles for the delivery of peptides, biologics, and soluble therapeutics. *Journal of Controlled Release*, 219:519–535.

Pavlovetc, I. M., Podshivaylov, E. A., Chatterjee, R., Hartland, G. V., Frantsuzov, P. A., and Kuno, M. (2020). Infrared photothermal heterodyne imaging: Contrast mechanism and detection limits. *Journal of Applied Physics*, 127(16):165101.

Pegtel, D. M. and Gould, S. J. (2019). Exosomes. *Annual Review of Biochemistry*, 88:487–514.

Piliarik, M. and Sandoghdar, V. (2014). Direct optical sensing of single unlabelled proteins and super-resolution imaging of their binding sites. *Nature Communications*, 5(1):4495.

Prausnitz, M. R., Mitragotri, S., and Langer, R. (2004). Current status and future potential of transdermal drug delivery. *Nature reviews Drug discovery*, 3(2):115–124.

Ralston, T. S., Marks, D. L., Carney, P. S., and Boppart, S. A. (2006). Inverse scattering for optical coherence tomography. *JOSA A*, 23(5):1027–1037.

Ralston, T. S., Marks, D. L., Carney, P. S., and Boppart, S. A. (2007). Interferometric synthetic aperture microscopy. *Nature Physics*, 3(2):129–134.

Rassaei, L., Marken, F., Sillanpää, M., Amiri, M., Cirtiu, C. M., and Sillanpää, M. (2011). Nanoparticles in electrochemical sensors for environmental monitoring. *TrAC Trends in Analytical Chemistry*, 30(11):1704–1715.

Rejman, J., Oberle, V., Zuhorn, I. S., and Hoekstra, D. (2004). Size-dependent internalization of particles *via* the pathways of clathrin- and caveolae-mediated endocytosis. *Biochemical Journal*, 377(Pt 1):159–169.

Samolis, P. D., Langley, D., O'Reilly, B. M., Oo, Z., Hilzenrat, G., Erramilli, S., Sgro, A. E., McArthur, S., and Sander, M. Y. (2021). Label-free imaging of fibroblast membrane interfaces and protein signatures with vibrational infrared photothermal and phase signals. *Biomedical Optics Express*, 12(1):303–319.

Samolis, P. D. and Sander, M. Y. (2019). Phase-sensitive lock-in detection for high-contrast mid-infrared photothermal imaging with sub-diffraction limited resolution. *Optics Express*, 27(3):2643–2655.

Schermelleh, L., Ferrand, A., Huser, T., Eggeling, C., Sauer, M., Biehlmaier, O., and Drummen, G. P. (2019). Super-resolution microscopy demystified. *Nature Cell Biology*, 21(1):72–84.

Scherr, S. M., Daaboul, G. G., Trueb, J., Sevenler, D., Fawcett, H., Goldberg, B., Connor, J. H., and Ünlü, M. S. (2016). Real-time capture and visualization of individual viruses in complex media. *ACS Nano*, 10(2):2827–2833.

Schnell, M., Mittal, S., Falahkheirkhah, K., Mittal, A., Yeh, K., Kenkel, S., Kajdacsy-Balla, A., Carney, P. S., and Bhargava, R. (2020). All-digital histopathology by infrared-optical hybrid microscopy. *Proceedings of the National Academy of Sciences*, 117(7):3388–3396.

Selmke, M., Braun, M., and Cichos, F. (2012). Gaussian beam photothermal single particle microscopy. *JOSA A*, 29(10):2237–2241.

Sennaroglu, A. (2010). *Photonics and Laser Engineering: Principles, Devices, and Applications*. McGraw-Hill.

Sevenler, D., Avci, O., and Ünlü, M. S. (2017). Quantitative interferometric reflectance imaging for the detection and measurement of biological nanoparticles. *Biomedical Optics Express*, 8(6):2976–2989.

Sevenler, D., Daaboul, G. G., Ekiz Kanik, F., Ünlü, N. L., and Ünlü, M. S. (2018). Digital microarrays: Single-molecule readout with interferometric detection of plasmonic nanorod labels. *ACS Nano*, 12(6):5880–5887.

Soto, J. M., Rodrigo, J. A., and Alieva, T. (2018). Optical diffraction tomography with fully and partially coherent illumination in high numerical aperture label-free microscopy. *Applied Optics*, 57(1):A205–A214.

Stanley, S. (2014). Biological nanoparticles and their influence on organisms. *Current Opinion in Biotechnology*, 28:69–74.

Tamamitsu, M., Toda, K., Horisaki, R., and Ideguchi, T. (2019). Quantitative phase imaging with molecular vibrational sensitivity. *Optics Letters*, 44(15):3729–3732.

Tamamitsu, M., Toda, K., Shimada, H., Honda, T., Takarada, M., Okabe, K., Nagashima, Y., Horisaki, R., and Ideguchi, T. (2020). Label-free biochemical quantitative phase imaging with mid-infrared photothermal effect. *Optica*, 7(4):359–366.

Taylor, R. W., Mahmoodabadi, R. G., Rauschenberger, V., Giessl, A., Schambony, A., and Sandoghdar, V. (2019). Interferometric scattering microscopy reveals microsecond nanoscopic protein motion on a live cell membrane. *Nature Photonics*, 13(7):480–487.

Taylor, R. W. and Sandoghdar, V. (2019). Interferometric scattering microscopy: Seeing single nanoparticles and molecules via rayleigh scattering. *Nano Letters*, 19(8):4827–4835.

Tian, L., Li, X., Ramchandran, K., and Waller, L. (2014). Multiplexed coded illumination for fourier ptychography with an led array microscope. *Biomedical Optics Express*, 5(7):2376–2389.

Tian, L. and Waller, L. (2015). Quantitative differential phase contrast imaging in an led array microscope. *Optics Express*, 23(9):11394–11403.

Toda, K., Tamamitsu, M., Nagashima, Y., Horisaki, R., and Ideguchi, T. (2019). Molecular contrast on phase-contrast microscope. *Scientific Reports*, 9(1):1–7.

Trueb, J. T., Avci, O., Sevenler, D., Connor, J. H., and Ünlü, M. S. (2017). Robust visualization and discrimination of nanoparticles by interferometric imaging. *IEEE Journal of Selected Topics in Quantum Electronics*, 23(2):394–403.

Tsuda, S., Yamaguchi, S., Kanamori, Y., and Yugami, H. (2018). Spectral and angular shaping of infrared radiation in a polymer resonator with molecular vibrational modes. *Optics Express*, 26(6):6899–6915.

Turrell, G. and Corset, J. (1996). *Raman microscopy: developments and applications.* Academic Press.

Vahey, M. D. and Fletcher, D. A. (2019). Low-fidelity assembly of influenza a virus promotes escape from host cells. *Cell*, 176(1):281 – 294.e19.

Waxenegger, J., Trügler, A., and Hohenester, U. (2015). Plasmonics simulations with the mnpbem toolbox: Consideration of substrates and layer structures. *Computer Physics Communications*, 193:138 – 150.

Welsch, S., Kolesnikova, L., Krähling, V., Riches, J. D., Becker, S., and Briggs, J. A. G. (2010). Electron tomography reveals the steps in filovirus budding. *PLoS Pathogens*, 6(4):1–9.

Wu, Y., Deng, W., and Klinke II, D. J. (2015). Exosomes: Improved methods to characterize their morphology, rna content, and surface protein biomarkers. *Analyst*, 140(19):6631–6642.

Yilmaz, H., van Putten, E. G., Bertolotti, J., Lagendijk, A., Vos, W. L., and Mosk, A. P. (2015). Speckle correlation resolution enhancement of wide-field fluorescence imaging. *Optica*, 2(5):424–429.

Young, G., Hundt, N., Cole, D., Fineberg, A., Andrecka, J., Tyler, A., Olerinyova, A., Ansari, A., Marklund, E. G., Collier, M. P., Chandler, S. A., Tkachenko, O., Allen, J., Crispin, M., Billington, N., Takagi, Y., Sellers, J. R., Eichmann, C., Selenko, P., Frey, L., Riek, R., Galpin, M. R., Struwe, W. B., Benesch, J. L. P., and Kukura, P. (2018). Quantitative mass imaging of single biological macromolecules. *Science*, 360(6387):423–427.

Yurdakul, C., Avci, O., Matlock, A., Devaux, A. J., Quintero, M. V., Ozbay, E., Davey, R. A., Connor, J. H., Karl, W. C., Tian, L., and Ünlü, M. S. (2020). High-throughput, high-resolution interferometric light microscopy of biological nanoparticles. *ACS Nano*, 14(2):2002–2013.

Yurdakul, C. and Ünlü, M. S. (2020). Computational nanosensing from defocus in single particle interferometric reflectance microscopy. *Optics Letters*, 45(23):6546–6549.

Yurt, A., Daaboul, G. G., Connor, J. H., Goldberg, B. B., and Selim Ünlü, M. (2012). Single nanoparticle detectors for biological applications. *Nanoscale*, 4:715–726.

Zanchetta, G., Lanfranco, R., Giavazzi, F., Bellini, T., and Buscaglia, M. (2017). Emerging applications of label-free optical biosensors. *Nanophotonics*, 6(4):627–645.

Zhang, D., Lan, L., Bai, Y., Majeed, H., Kandel, M. E., Popescu, G., and Cheng, J.-X. (2019). Bond-selective transient phase imaging via sensing of the infrared photothermal effect. *Light: Science & Applications*, 8(1):1–12.

Zhang, D., Li, C., Zhang, C., Slipchenko, M. N., Eakins, G., and Cheng, J.-X. (2016a). Depth-resolved mid-infrared photothermal imaging of living cells and organisms with submicrometer spatial resolution. *Science Advances*, 2(9).

Zhang, T., Godavarthi, C., Chaumet, P. C., Maire, G., Giovannini, H., Talneau, A., Allain, M., Belkebir, K., and Sentenac, A. (2016b). Far-field diffraction microscopy at $\lambda/10$ resolution. *Optica*, 3(6):609–612.

Zhang, Y., Yurdakul, C., Devaux, A. J., Wang, L., Xu, X. G., Connor, J. H., Ünlü, M. S., and Cheng, J.-X. (2021). Vibrational spectroscopic detection of a single virus by mid-infrared photothermal microscopy. *Analytical Chemistry*, 93(8):4100–4107. PMID: 33596049.

Zheng, G., Horstmeyer, R., and Yang, C. (2013). Wide-field, high-resolution fourier ptychographic microscopy. *Nature Photonics*, 7(9):739–745.

Zhou, K. C., Qian, R., Degan, S., Farsiu, S., and Izatt, J. A. (2019). Optical coherence refraction tomography. *Nature Photonics*, 13(11):794–802.

Zong, H., Yurdakul, C., Bai, Y., Zhang, M., Unlu, M. S., and Cheng, J.-X. (2021). Background-suppressed high-throughput mid-infrared photothermal microscopy via pupil engineering. *arXiv preprint arXiv:2104.06247*.

CURRICULUM VITAE

[redacted]

[redacted]

[redacted]

[redacted]